Relativistic Magnetohydrodynamic Simulations of Extragalactic Jets

Tobias Leismann

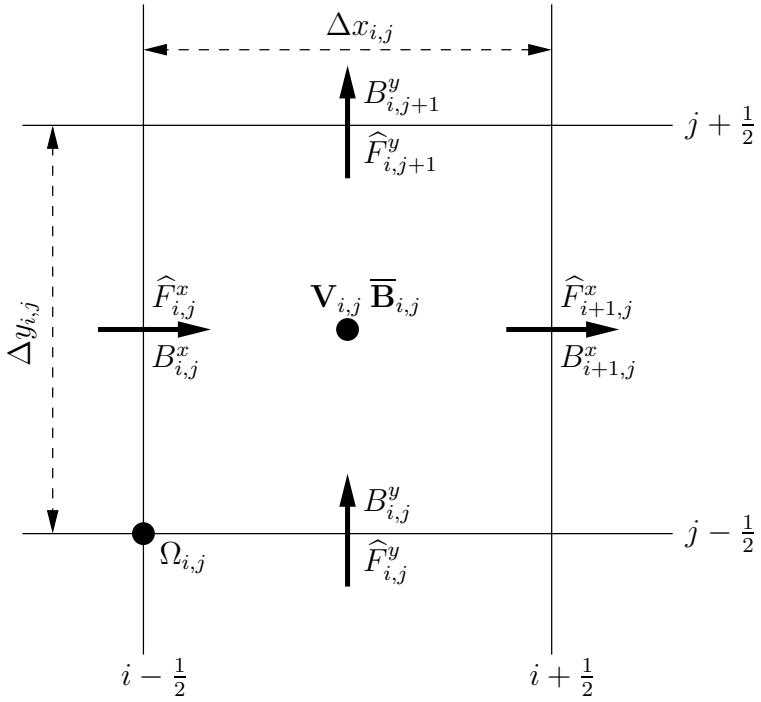

Max-Planck-Institut für Astrophysik

Relativistic Magnetohydrodynamic Simulations of Extragalactic Jets

Tobias Leismann

Vollständiger Abdruck der von der Fakultät für Physik der Technischen Universität München zur Erlangung des akademischen Grades eines

Doktors der Naturwissenschaften

genehmigten Dissertation.

Vorsitzender: Univ.-Prof. Dr. Lothar Oberauer

Prüfer der Dissertation:

1. Priv.-Doz. Dr. Ewald Müller
2. Univ.-Prof. Dr. Andrzej J. Buras

Die Dissertation wurde am 29. Januar 2004 bei der Technischen Universität München eingereicht und durch die Fakultät für Physik am 12. März 2004 angenommen.

Contents

1 Extragalactic Jets **7**
- 1.1 Introduction . . . 7
- 1.2 Observation . . . 8
- 1.3 Modelling . . . 14
- 1.4 Numerical simulations . . . 16

2 Numerical RMHD **21**
- 2.1 Equations of ideal relativistic MHD . . . 21
  - 2.1.1 Units . . . 21
  - 2.1.2 The RMHD equations as a system of conservation laws . . . 22
  - 2.1.3 The equations in primitive variables . . . 24
  - 2.1.4 The equations in cylindrical coordinates . . . 25
  - 2.1.5 Spectral decomposition . . . 26
- 2.2 Numerical techniques . . . 29
  - 2.2.1 Discrete space-time . . . 29
  - 2.2.2 Conservative method . . . 29
  - 2.2.3 The Riemann problem . . . 30
  - 2.2.4 Directional splitting . . . 31
  - 2.2.5 An approximate Riemann solver — HLLE . . . 31
  - 2.2.6 Spatial interpolation . . . 36
  - 2.2.7 Time integration . . . 37
  - 2.2.8 Recovery of primitive variables . . . 37
  - 2.2.9 Conservation of $\nabla \cdot \mathbf{B} = 0$ . . . 38
  - 2.2.10 Boundary conditions . . . 40
  - 2.2.11 Code structure . . . 41
- 2.3 Code validation . . . 42
  - 2.3.1 1D test problems . . . 42
  - 2.3.2 2D test problems . . . 45
  - 2.3.3 Convergence Tests . . . 53

3 Parameter Study **55**
- 3.1 Introduction to jet simulations . . . 55
- 3.2 Model parameters . . . 58
- 3.3 C2 series . . . 59
- 3.4 B1 series . . . 69
- 3.5 C1 series . . . 79
- 3.6 Discussion . . . 87

4 Long Term Evolution **91**
4.1 Simulation setup . . . 91
4.2 Results . . . 92
4.2.1 Morphology . . . 92
4.2.2 Temporal evolution . . . 99
4.3 Discussion . . . 100
4.3.1 Comparison with previous simulations . . . 103
4.3.2 Influence of the magnetic field on the long term evolution . . . 104
4.3.3 Comparison with observations . . . 105
4.3.4 Limitations . . . 107

5 Summary and Conclusions **111**

List of Figures **117**

Bibliography **121**

1 Extragalactic Jets

1.1 Introduction

An extragalactic jet has first been described by Curtis (1918) as "A curious straight ray ... connected with the nucleus" in an optical image of the galaxy M87. In the 1950s the term *jet* was first used for describing this phenomenon. It was associated with the ejection of material from the inner region of the galaxy (Baade & Minkowski, 1954). By then radio observations of twin lobes in extended radio galaxies – of which Cygnus A is one of the best known (Jennison & Das Gupta, 1953) – provided more and more evidence for highly collimated jets. After many of these radio sources had been identified with extragalactic objects at cosmological distances, it became clear that they were of gigantic dimensions (up to megaparsec scales) and had huge powers. Shklovskii (1953) suggested that the radio emission might be electron synchrotron radiation, an idea which was indirectly supported by the results of measuring the optical polarisation of the M87 jet (Baade, 1956). Attempts to explain these observations with ballistic ejection of plasma from the central object all failed because of the huge energies involved and because of the short synchrotron lifetimes of electrons ($< 10^6$ years) which would require the presence of reacceleration mechanisms.

By the 1960s the term *jet* was in common use although still without the recognition that a continuous flow of matter was involved. In an attempt to explain the M87 jet and the double lobed radio sources, Shklovskii (1963) used a number of ideas which are still important for today's theories: the accretion of plasma into the gravitational potential of the *active galactic nucleus* (AGN) which is then heated, breaks out along a preferred axis and flows into the intergalactic medium. In 1974 Blandford & Rees (1974) and Scheuer (1974) developed the idea that the energy transport is in form of *beams* where most of the plasma's internal energy is transformed into kinetic energy by a collimation process and recovered where the beam interacts with the external medium. Thus supersonic fluid flow can deliver the required energy continuously from the nucleus to the radio lobes and even allows for particle reacceleration. With increase in angular resolution of radio telescopes, bridges of non-thermal radiation were discovered between the cores and the radio lobes establishing a surprisingly collimated physical link between nuclei and lobes.

During the last three decades this theory has gained substantial support from observational evidence. In particular the advent of the *Very Large Array* (VLA) in the beginning of the 1980s led to the discovery of many jets in powerful extragalactic sources in accordance with the beam theory. *Very–Long–Baseline–Interferometry*

(VLBI) has made it possible to observe small-scale nuclear jets on the milliarcsecond scale. Optical identification of many sources became possible with the *Hubble Space Telescope* (HST) in the 1990s. Recently, the *Chandra X-Ray Observatory*, launched in 1999, has made it possible to observe kiloparsec-scale jets in AGNs with high angular resolution and sensitivity in the X-ray band. These observations not only led to the detection of many X-ray jets in sources of low radio power but also show relativistic bulk motion on very large scales (see e.g. Worrall et al., 2001; Sambruna et al., 2002; Gambill et al., 2003, and references therein).

1.2 Observation

Terminology

Radio galaxies are observed in a large number of forms. Therefore, several classification schemes were introduced by different observers. We will describe some of these schemes here and also the properties of the galaxies falling into those categories. Some elements of radio source structure which are most commonly used by astronomers will be described here:

Cores are the stationary components associated with the power source in the nucleus of the radio galaxy. Their spectrum is flat (see below) and they are often only resolved by VLBI observation (i.e., at angular resolutions <0.1 arcseconds). The core is identified with the optical image of the galaxy in large scale observations (see central panel of Fig. 1.1).

Lobe is the general term to describe the extended region of radio emission, generally assumed to consist of plasma transported from the galaxy cores by the beams. They often have a plume like appearance as illustrated in Fig. 1.1.

Jets are linear features linking the cores with the outer extended lobe structures. Following Hughes & Miller (1991) a structure must meet the following criteria to be called a jet: (i) its length must be at least four times its width, (ii) the separation from the extended structure should be possible by high resolution observations, and (iii) it should be aligned to the core where closest to it. Jets may be visible along either part of, or the whole inferred path and on one or both sides of the core (*one-sided* or *two-sided* jets), smooth or knotty, centre–brightened or edge–brightened. In high resolution observations the jet breaks down into distinct bright features, usually attributed to standing shocks in the jet's flow, thus giving the jet a knotty structure (see Fig. 1.1).

Components are local brightness peaks with sufficient statistical significance, normally associated with moving features. Single components can be followed for example by VLBI observations to measure their proper motion. Their spectral index is typically around 0.6.

Hotspots are the bright regions at the outer extremities of the lobes. They have linear sizes of less than 1 kpc and are naturally interpreted to be the *working surface* where the beam meets the ambient medium, thus creating a shock which converts kinetic energy into internal energy of relativistic particles leading to further radiation. Their

spectrum is somewhat flatter than that of the jets.

Basic facts

Very little is known about the central nucleus of radio sources, because the resolution of today's instruments is limited to regions larger than 100 mpc. Consequently, our knowledge of jets starts at the time when they are well collimated at a distance of 0.1 to 1 pc.

On the parsec scale (100 mpc to 100 pc) jets emit from radio through X-ray frequencies due to synchrotron and inverse Compton processes. They are observed using VLBI or the *Very Large Baseline Array* (VLBA). They display a high degree of collimation and their morphologies are characterised by components which separate from the core at sometimes super-luminous speeds. Many parsec-scale jets are one–sided and show intra-day variability of the radio emission. If the variability is intrinsic, this constrains the actual sizes of the emitting regions to less than a light day.

On the kiloparsec scale (1 kpc to 1 Mpc) radio and X-ray jets are very common and extended radio lobes with or without bright hotspots can be found. Their overall morphologies depend on their interaction with surrounding gas and may be influenced strongly by high peculiar velocities in rich galaxy clusters. Evidence for relativistic speeds on kpc-scales in the beams of jets have been found both in radio (e.g. Bridle et al., 1994) and X-ray observations (Sambruna et al., 2002).

Classification

Common to all extragalactic radio sources is that they are manifestations of the spectacular phenomenon of Active Galactic Nuclei (AGNs). They produce enormous energies ($10^{41} - 10^{49}$ erg s^{-1}) of up to four times the luminosity of a typical galaxy in very small volumes of probably $\ll 1\mathrm{pc}^3$ (Krolik, 1999). Their emission can be observed from infrared to gamma ray frequencies.

Generally large scale radio sources can be divided into two groups: (a) *extended, steep spectrum* objects with a roughly collinear double lobe structure extending out to either side of the host galaxy, and (b) *compact, flat spectrum* sources where no or very little extended structure is observed. The terms *flat spectrum* and *steep spectrum* refer to the spectral index α of the flux density S in its conventional form $S \propto \nu^{-\alpha}$ where ν is the frequency. Conventionally, flat is defined as $\alpha \leq 0.5$ and steep as $\alpha \geq 0.5$. Steeper spectra are associated with radiatively aged material, i.e., synchrotron radiation loss combined with expansion as material flows away from sites of active acceleration (Leahy, 1991). As observational methods advanced, it became apparent that compact objects contain some of the extended steep spectrum emission elements present in extended objects and vice-versa. The classification was then modified to *lobe-dominated* and *core-dominated*, respectively (Muxlow & Garrington, 1991). Core-dominated objects are those where the bulk emission region is not resolved by the VLA and therefore must be smaller than $20(D_A H_0/c)(h/0.75)^{-1}$ kpc,

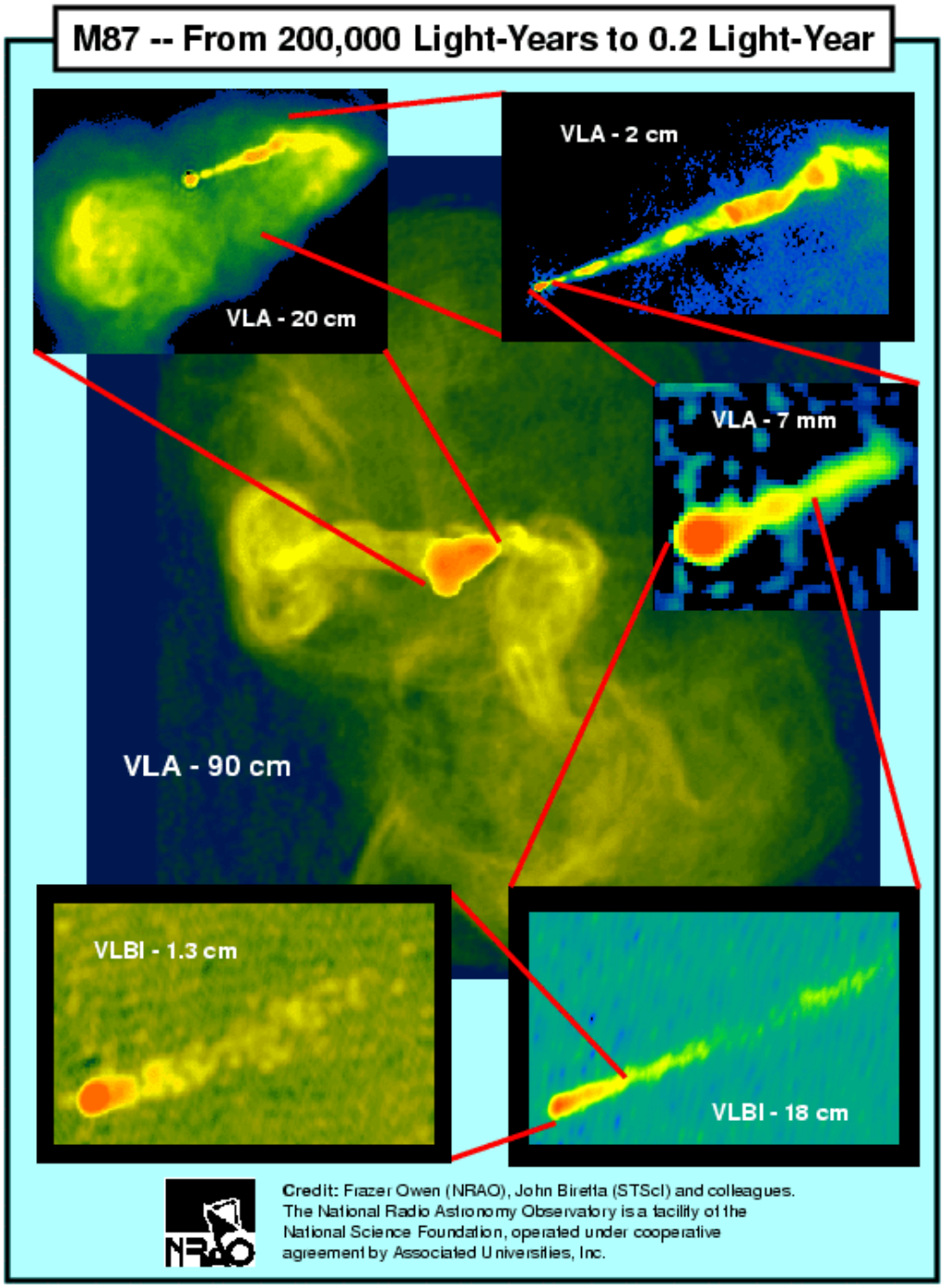

Figure 1.1: Montage of different images of the radio galaxy M87. The largest image demonstrates the huge size of the outer lobes, while the next smaller image shows that the inner lobes are of plume like form. Evidence for a complex internal structure is seen in the smaller images of the jet, which exhibits a very jet. The montage also illuminates the fact that many observations with different telescopes are required to resolve a radio galaxy on all scales.

where D_A is the angular diameter distance[1], $H_0 = 100h$ km s^{-1} is the Hubble constant and h is the scale factor of H_0. Both of these types are divided into several sub–classes. Lobe-dominated sources, found in luminous spiral and elliptical galaxies, fall into three distinct sub–types, associated to different types of AGNs: radio Seyfert galaxies, lobe–dominated radio galaxies and lobe–dominated radio–loud quasars.

Many Seyfert galaxies show S-shaped kpc scale radio structures (possibly due to disruption of the jet) and they are often less powerful emitters than elliptical galaxies. This is commonly attributed to the lower power output of the AGN and to the dense interstellar medium of the galaxies discs (making plasma ejection through it more difficult). Some Seyfert galaxies do not contain any evidence of jets. Their radio luminosities at 1 GHz are typically $P \sim 10^{21} - 10^{25}$ W Hz^{-1} (at 1 GHz).

The properties and morphology of lobe–dominated radio galaxies undergo an abrupt change at a luminosity of around $P = 5 \times 10^{25}$ MW Hz^{-1} (at 178 MHz). A simple classification scheme was first introduced by Fanaroff & Riley (1974): galaxies below the critical luminosity are called *Fanaroff–Riley type I (FR I)* objects, those above are known as *FR II* type objects.

FR I sources tend to have smooth, continuous two–sided jets running into large scale lobe structures also called *plumes*. They are *edge–darkened* meaning that the ratio of the separation between the peaks of radio emission and the total size of the source is small, e.g. less than 0.5 in the case of FR I galaxies (see e.g. Muxlow & Garrington, 1991; Krolik, 1999). The jets contribute more than 10% of the total radio power of the source. Their steepest radio spectra, and therefore the radiatively oldest material lie furthest from the host galaxy in the extended lobes. FR II sources tend to be *edge–brightened*, i.e. they show bright hotspots at the outer edges of the extended emission regions. Their jets are usually one–sided (with a jet to counter jet intensity ratio of $> 4/1$). Furthermore, these jets are not smooth as in FR I sources but consist of several bright *knots*. The core and the jets together often only contribute $< 10\%$ to the total radio power, and in many sources the core is not detected at all. The steepest spectra are measured in the bridges, the inner regions of the lobes. A special class of objects, the *fat doubles*, marks the transition between FR Is and FR IIs. Fat doubles are weak FR II sources with large double lobes and almost no evidence for core, jets and hotspots.

Figure 1.2 shows a radio-optical superposed image of the FR II object 3C219. The bright dot in the centre is the host galaxy, i.e., the core. The inflated radio lobes with their hotspots, and on one side of the core, a part of the jet, are clearly visible. The image also illustrates the immense size of the jets and lobes when compared to the core, which is coincident with the optical image of the galaxy. Another archetype FR II object is Cygnus A (3C 405). The FR I object M87 is shown in Fig. 1.1. Another typical FR I source is 3C 449.

There are a couple of sub-classes of FR I and FR II objects. *Narrow-Angle-Tail* (NAT) sources, e.g. NGC 1265, are of FR I type with bent two–sided jets running into extended tails. This is believed to be due to the proper motion of the host

[1] D_A is the distance between an observer and objects at which two object on the sky with angular separation ϵ have the mutual distance ϵD_A.

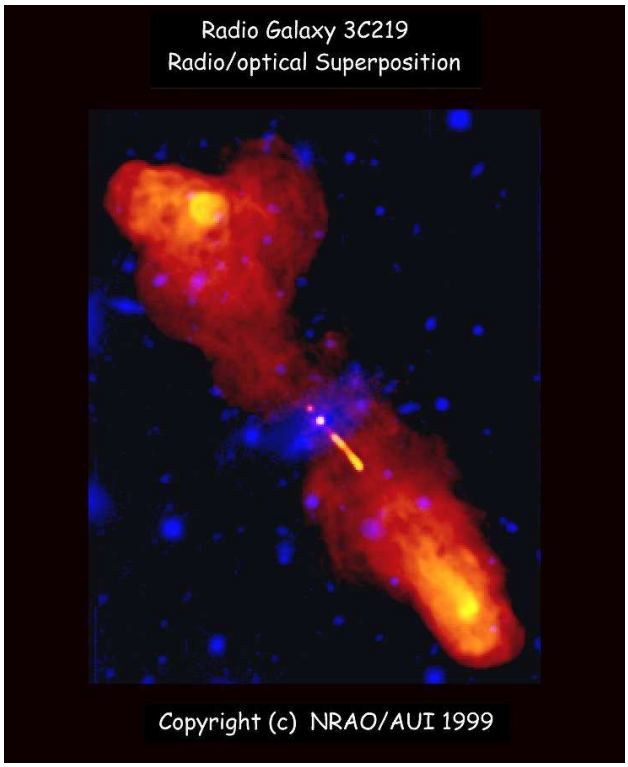

Figure 1.2: Fanaroff–Riley class II radio galaxy superposed onto an optical image. Note the difference in size between the core and the lobes. A jet is only visible on one side of the core, but hotspots are visible in both outer lobes. The image was taken from the home page of Alan Bridle (Bridle, 2003).

galaxy with respect to the cluster it resides in. The radio structure is then bent by the ram pressure of the hot cluster gas (Begelman et al., 1979). *Wide-Angle-Tail* sources (WAT, Owen & Rudnick (1976), for example 3C 465) are C–shaped objects with disrupted FR I type tails and inner hotspots linked to the central component by FR II type jets. Although not many of these sources are observed, they are often associated with optically dominated galaxies in rich clusters.

With a morphology similar to that of FR IIs, lobe–dominated radio–loud quasars display bright, knotty, one–sided jets and bright cores with higher luminosities than those of radio galaxies. They are mainly found at high redshift and consist of powerful extended radio emission regions (with a luminosity of $P > 5 \times 10^{25}$ MW Hz^{-1} at 178 MHz observing frequency) surrounding some quasars. An example of this class of objects is 3C 179 (Shone et al., 1985).

The defining property of core–dominated sources is a luminous core in the centre often combined with a bright, one–sided jet. These sources have a high surface brightness and are thus particularly suited for observation by VLBI. Knots in VLBI jets are often observed to move with *apparent superluminal* speeds. For example, in 3C 120 superluminal motion was detected from the parsec scale (Seielstad et al., 1979; Walker et al., 1987) to tens of pc (e.g. Benson et al., 1988; Walker, 1997, etc.). In Gómez et al. (1998) and Gómez et al. (1999) up to ten components with apparent

speeds between 2.3 and 5.4 $h^{-1}c$ are shown in 3C 120. A significant bending of the jet is very common in core–dominated sources. The jet of 3C 273 bends by $\approx 20°$ within the first 10 milliarcseconds from the core and extends continuously to 22 arcseconds from the core (Whitney et al., 1971; Cohen et al., 1971). In addition to the bright components, VLA images show a low surface brightness extended component, often on the opposite side of the jet.

Magnetic fields

The orientation of magnetic fields projected on the plane of the sky can be detected by polarisation measurements, i.e. the fact that many sources display a high degree of polarisation implies ordering of the magnetic field perpendicular to the line of sight. A general trend for large scale magnetic fields of radio jets is that low power radio sources (e.g. FR I radio galaxies) are dominated by transversal fields ($B_\perp$) while sources with larger total and core powers (like FR IIs) show parallel magnetic fields ($B_\parallel$) aligned with the jet axis (see e.g. Bridle, 1984; Bridle & Perley, 1984 for kpc scale observations and Wardle, 1998 for VLBI observations). However, this trend is not absolute, as the observed polarisation patterns of radio sources are as diverse as the sources themselves. Since the magnetic fields and thus also the polarisation of the radiation are tracers of the underlying hydrodynamics, oblique shocks, shear flows and bending of jets may lead to changes in the magnetic field configuration. For example bright knots in FR IIs, attributed to shocked gas, often display a $B_\perp$ configuration while the fainter emission of the surrounding jet might still have $B_\parallel$. More recent studies by Laing & Bridle (2002) and Laing et al. (2003) infer that the FR I jets in 3C 31 primarily display toroidal and to a lesser degree longitudinal components and only a very small radial component; only where the magnetic field becomes isotropic at the edge of the jet, the radial component becomes comparable.

Directly measuring the strength of the magnetic fields in AGNs and extragalactic radio sources is not possible. Therefore inferring the magnetic field always depends on the physical model fitted to the observation. Using equipartition arguments (i.e. equating thermal and magnetic pressure) and fitting observed spectra to standard synchrotron models lead to values of $B = 10^{-6} - 10^{-3}$ G for radio galaxies. For the jet of M87 Heinz & Begelman (1997) get a magnetic field strength of 0.1 to 0.7 times the equipartition value. Combining X-ray and radio observations in a single synchrotron self-Compton emission model allows to constrain the magnetic field strength further. A number of authors have applied this method to the hotspots of several radio galaxies and have inferred values between a factor of 25 below equipartition and slightly above equipartition. (e.g. Harris et al., 1994; Hardcastle et al., 1998, 2002; Wilson et al., 2000; Donahue et al., 2003).

Theoretically understanding the magnetic fields in the jets is not simple since observations do not yield enough data. However it is believed that the spine of the jet is threaded with a mainly toroidal field configuration surrounded by a longitudinal field. Radial fields do not play a large role (Begelmann et al., 1984; Laing, 1993). An average magnitude of the equipartition field would be $B_{eq} \sim 10^{-3}$ G in the hotspots to $B_{eq} \sim 10^{-5}$ G in the lobes, compared to $B_{eq} < 10^{-6} - 10^{-5}$ G in the external medium (Ferrari, 1998).

1.3 Modelling

The standard model

Although there is no complete theory to describe the observations of AGNs and extragalactic jets, the hydrodynamic explanation of Blandford & Rees (1974) is considered the standard model for explaining extended radio galaxies by most of the scientific community (see Begelmann, Blandford & Rees, 1984; Ferrari, 1998, for detailed reviews). In summary the facts are the following: Twin opposite jets are produced and collimated in the cores of AGNs. They are most likely powered by accretion of material onto a very massive black hole which continuously thrusts out magnetised plasma along its rotational axis. The plasma is channelled into jets with a highly relativistic bulk flow speed. The jets plough their way through the intergalactic gas thus transporting energy and momentum away from the core. A working surface which produces a bow shock is generated where the head of the jet pushes against the external gas and is associated with the hotspot; and a cocoon is formed around the entire source which is filled with a mixture of shocked ambient material and turbulent back flow of jet material.

On parsec scales the jet material moves with bulk Lorentz factors of $W \approx 10$ (Ghisellini et al., 1993) or even $W \approx 30 - 100$ (Begelman et al., 1994). Single moving components are explained by the shock–in–jet model as travelling shock waves inside the jet which heats the material and thus accelerates electrons. The main reasons for that model are the spectral evolution of the components and their variability time scales (Marscher & Gear, 1985). It is also supported by VLBI observations of the polarisation of the components (Wardle, 1998).

The morphologies of FR Is on kiloparsec scales are the result of the jets' deceleration from relativistic to sub-relativistic speeds (Bicknell, 1996; Laing, 1996*a*). They are assumed to be moving at transonic speeds (Begelmann et al., 1984) and thus appear two–sided as Doppler boosting (see next section) has no effect. Deceleration happens by entrainment of external material, a process which is only efficient when the speeds are transonic. If the jet is able to re-collimate a FR I source occurs, when the power is too large, it cannot re-collimate and the result might be a WAT. However, if the jet does not decelerate it continues with relativistic speed and will remain supersonic until it impacts with the external medium thereby forming a hotspot, and A FR II source results. Then the jet emission is enhanced by relativistic beaming (see below) while the counter jet suffers the opposite effect, therefore the source appears one–sided. The beam has two components: a fast spine and slower, hot shear layer which divides it from the cocoon (Sol et al., 1989; Swain et al., 1998; Aloy et al., 2000; Stawarz & Ostrowski, 2002).

In a unified model (see e.g. Urry & Padovani, 1995; Laing, 1996*b*) the observed differences between the many classes of extragalactic radio sources and quasars are explained by their different orientation towards the observer (e.g. a quasar might then simply be a radio galaxy seen head on) or influences of the external medium.

Figure 1.3: Illustration of superluminal motion. The radiation originating from points 1 and 2 reaches the distant observer nearly simultaneously, which leads to apparent transverse speeds greater than the speed of light.

Superluminal motion and relativistic beaming

There are two main arguments supporting the relativistic nature of extragalactic jets: (i) the observations of apparent *superluminal motion*; and (ii) the one-sidedness observed in most FR II jets.

When radio jets are observed in several epochs, most of them display components that are apparently moving away from the core at superluminal speeds (25 of 25 sources in Hough et al., 2002; more than 40 sources in Ghisellini et al., 1993). This effect is explained by assuming that the jets propagate with relativistic velocity, i.e., $v \approx c$, at a small inclination of the jet axis to the line of sight to the observer. The situation is illustrated in Fig. 1.3. Then the apparent time duration between two radiating events (labelled by 1 and 2 in Fig. 1.3) seen by a distant observer appears compressed, because the source moves at a similar speed and in the same direction as its radiation. Therefore the apparent transverse velocity as measured by a distant observer on the plane of the sky can exceed the speed of light. A distant observer measures an apparent transverse velocity $v_{\rm app}$ for any component with a flow velocity v at an angle θ to the line of sight towards the observer, which is given by (Blandford & Königl, 1979):

$$v_{\rm app} = \frac{v/c \sin\theta}{1 - v/c \cos\theta}. \tag{1.1}$$

This implies that the apparent speed has a maximum for $\cos\theta = v/c$ with $v_{\rm app}^{max} = Wc$, where $W = (1 - v^2/c^2)^{-1/2}$ is the Lorentz factor. For example, for $W = 10$ and $\theta = 6$ degrees the apparent speed would be almost $10c$.

The one-sidedness of jets observed in FR II sources can be explained by relativistic motion at a small angle to the line of sight, too. The so-called *Doppler beaming* is a combined effect of relativistic aberration and of the ordinary Doppler effect which makes the emission of the approaching jet become blue shifted in the frame of the observer. The resulting asymmetry in the luminosity of the twin jets is given by the Doppler factor (Blandford & Königl, 1979)

$$D = W^{-1}(1 - v/c \cos\theta)^{-1} \ . \tag{1.2}$$

Thus, although the extended diffuse lobe emission is more or less symmetric (as the emitting plasma in the lobes is moving with small velocities and, therefore, its isotropic emission is not Doppler boosted), the jet only appears one–sided. Figure 1.2 illustrates how the Doppler beaming boosts the emission of the jet propagating

towards the observer: on one side of the core there is a bright linear feature which can clearly be identified with a jet, whereas on the other side no jet is visible.

Jet production

The large powers produced by AGNs concentrated in such small volumes lead to the consideration of models for jet formation and collimation based on processes around supermassive black holes ($> 10^6$ solar masses, Rees, 1984). Two mechanisms suggest themselves for extracting energy from the black hole to power the launching of the jet, (a) accretion of matter onto the black hole, thereby liberating gravitational energy that is transferred to matter flung along the rotational axis; (b) electrodynamic processes, tapping black hole rotational energy and feeding it into Poynting flux. In both cases the procedure leads to twin opposite jets as suggested by Blandford & Rees (1974). Both possibilities are general enough to allow for many different models for the formation and collimation of jets. This and the fact that we have no observations of the central region of the AGNs have led to the publication of a myriad of different models, from the early ones for electrodynamic or magnetohydrodynamic jet formation (Blandford & Znajek, 1977; Blandford & Payne, 1982) to very recent ones (Vlahakis & Tsinganos, 1999; Krasnopolsky et al., 2003; Meier et al., 2001; Tominmatsu & Takahashi, 2003; Okamoto, 2003, to name a few). Most likely a combination of electrodynamic energy extraction with magnetohydrodynamic collimation is needed to explain the jet formation and collimation phase. The former has recently been supported by direct observational evidence (Wilms et al., 2001), while the latter seems now to be the generally accepted idea (Blandford, 2002): the magnetic field that is attached to the accretion disk can be twisted to form a sort of helical magnetic sleeve around an emerging jet, consisting of an almost purely toroidal field. The highly relativistic jet is then collimated by the hoop stress magnetic pressure (i.e. by the Lorentz force created by the toroidal field around the flow), while material is further accelerated by magnetocentrifugal forces (Meier et al., 2001).

1.4 Numerical simulations

Time-dependent numerical simulations of jets have proven to be a very successful tool for the theoretical understanding of extragalactic radio sources. For this, the intergalactic medium (IGM) and the jets are approximated as fluid-like continuous media where the equations of hydrodynamics (HD) or magnetohydrodynamics (MHD) hold. This is justified because the collisional mean free path of the jet plasma is limited by collisional coupling through micro-Gauss magnetic fields. Then the Lamor radii and Debye lengths of electrons and protons in extragalactic jets are several orders of magnitude smaller than the jets' radii.

The first milestone in the field were the 2D Newtonian simulations performed by Norman et al. (1982). Their results verified the jet model of Blandford & Rees (1974), and many detailed features of VLA observations could be reproduced: for example the hotspots can be associated with the working surface (the terminal shock) of the

beam, the knots in the jet with internal conical shocks, and the lobe structure with the hot turbulent material of the inflated cocoon behind the bow shock of the jet. Figure 1.4 shows a sketch of the jet morphology as produced in a two-dimensional, axisymmetric hydrodynamic simulation (Müller, 1998). The following expressions are commonly used when describing the features of a jet simulation:

- the *cavity* is the region inside the leading bow shock, it is divided into
- the *beam*, which terminates in a shock (the Mach disk) near the head of the jet,
- the *cocoon*, formed by a mixture of back flowing beam material deflected by the Mach disk shock and ambient medium and
- the *shell*, the remaining outside part of the cavity consisting of high density, shocked ambient gas;
- *cross shocks* or internal shocks in the beam;
- the *hot spot*, the high pressure region of shocked gas downstream of the terminal Mach disk.

The cocoon is usually turbulent, vortices being ejected from the terminal shock (a process usually called *vortex shedding*), and flowing backwards in the opposite direction of the beam.

Following the initial success, numerical work in the 1980s and early 1990s focused on Newtonian HD and ideal MHD simulations in order to explain the observations by the VLA (see Burns et al., 1991, for a review). Both 2D and 3D simulation were used to gain insight on NAT (Balsara & Norman, 1992) and WAT (Norman et al., 1988; Loken et al., 1995) sources. MHD simulations demonstrated the importance of the toroidal magnetic field for jet confinement (Clarke et al., 1986, 1989; Lind et al., 1989; Kössl et al., 1990; Appl & Camenzind, 1992). Given the fact that extragalactic jets remain collimated flows for such length scales up to Mpc, many authors have performed simulations addressing the question of jet stability. Mixing properties of high Mach number HD jets have, for example, been studied in 3D by Bodo et al. (1998), while the stability of MHD jets has, for example, been examined by Hardee & Norman (1988), Norman & Hardee (1988) or Hardee et al. (1992) in 2D slab geometry, and by Hardee et al. (1995) or Rosen et al. (1999) in 3D.

Since the middle of the 1990s the advance in numerical algorithms and computer technology has made it possible to simulate relativistic (RHD) flows in 2D (e.g., Duncan & Hughes, 1994; Martí et al., 1994, 1995, 1997). One absolute necessity for developing a time dependent RHD code is to write the equations as a system of conservation laws and exploit their hyperbolic character (see e.g. Martí et al., 1991; Martí & Müller, 1996). Mathematically, this is required to guarantee that the RHD equations (as any other hyperbolic system of partial differential equations) converges to the right physical solution. One main conclusion of relativistic jet simulations is that both the internal energy and the Lorentz factor increase the effective inertial mass of the beam, i.e. it can become both thermally and kinematically relativistic.

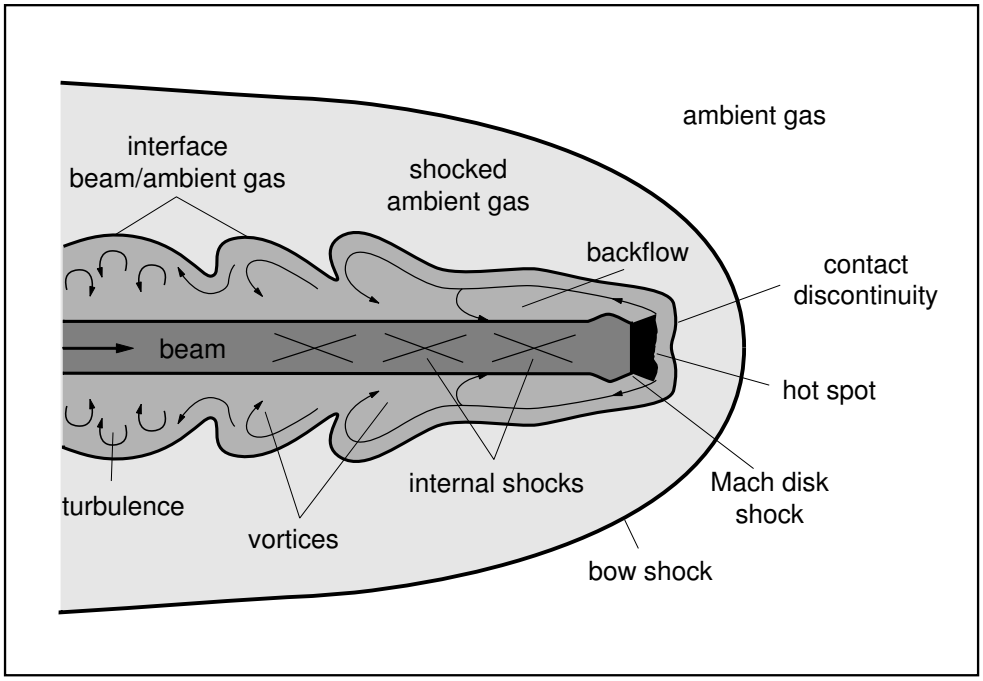

Figure 1.4: Sketch of the morphology of an axisymmetric supersonic light jet in a homogeneous ambient medium (image taken from Müller, 1998). The different components found in the simulations can be associated with corresponding observations, e.g., the hotspot is found between the interface dividing beam and ambient gas and the terminal shock at the head of the beam (called Mach disk shock). The knots observed in many jets (e.g., Fig. 1.1) can be identified with internal shocks.

This enhances the stability of the beam compared to equivalent classical flows. An early review by Norman (1996) describes the relativistic effects and the differences between 2D and 3D non-relativistic simulations. Long term evolution studies of 2D axisymmetric, powerful jets have been performed by Martí et al. (1998) and Komissarov & Falle (1997, 1998) for fixed plasma compositions and by Scheck et al. (2002) with different plasma compositions. Highly relativistic jets from collapsars were simulated as a likely explanation for long gamma-ray bursts (Aloy et al., 2000, 2002). More recently even in full 3D RHD simulations have become possible (Aloy et al., 1999*b*,*a*, 2000; Aloy & Martí, 2002; Aloy et al., 2003). While cross shocks on the beam are similar to 2D simulations, the turbulence in the cocoon is entirely different. Also, the propagation of the jets is more efficient due to wobbling of its head (drill effect).

Relativistic MHD (RMHD) simulations of jets are still difficult because the RMHD equations do not form a strictly hyperbolic system of conservation laws and, therefore, pose severe difficulties to the application of standard numerical techniques to solve systems of hyperbolic PDEs (see Sec. 2.1.5). Consequently, only a few codes exists for that purpose. The first 2D simulations performed by van Putten (1993, 1996) used pseudo-spectral techniques and were very limited in their range of parameters. Simulations performed by the group around Koide in 2D (Koide et al., 1996; Koide, 1997) and 3D (Nishikawa et al., 1997, 1998) suffered from similar draw-

backs: low resolution (only 2 zones per beam radius), low Lorentz factor (only up to 4.56) and short evolution times of the jets. In addition, this group has never published a full suite of test results that would validate their numerical method. Komissarov (1999*a*) applied his non-conservative, second-order RMHD code to 2D jets with toroidal fields (Komissarov, 1999*b*, , see also Sec. 2.3.2) and to the recently discovered jet-torus structure in the crab nebula (Komissarov & Lyubarsky, 2003).

Finally, in the past few years, jet formation has been studied using general relativistic MHD (GRMHD) simulations. Koide et al. (1998, 1999, 2000, 2002) and Koide (2003) performed 2D simulations of jet formation from accretion disks of rotating Schwarzschild and Kerr Black holes and from a rapidly rotating black hole magnetosphere. While their results support the current view of jet formation theory, they should be treated with caution: due to the considerable numerical challenge involved, their code can only evolve the system for very few rotational periods and the outflow only reaches a Lorentz factor of about 2. And in these simulations there is no specific control on the evolution of $\nabla \cdot \mathbf{B} = 0$ (Sec. 2.2.9). Additionally, magnetic twisting might change the picture completely when looking at the problem in 3D (Blandford, 2002).

2 Numerical RMHD

RMHD deals with the behaviour of relativistic, conducting fluids and electromagnetic fields. It is based on the assumption that the mean free path of the electrons is much smaller than the characteristic length scale of the problem, leading to a high collisional frequency of the electrons, such that Ohm's law is valid in its simple form, $\mathbf{J} = \sigma_{\rm con}\mathbf{E}$. In an *ideal RMHD* plasma the electromagnetic fields act on both the electrons and the ionised atoms to produce bulk motion of the medium itself with no charge separation, which in turn will produce modifications of the electromagnetic fields. In the limit of infinite conductivity, this is fulfilled, and the electric field vanishes in the fluid's rest frame. The mechanical motion of the matter can be described in terms of a single conducting fluid by combining the Euler equations with the Maxwell equations (Jackson, 1975). Ideal (R)MHD applies to many astrophysical plasmas, and in particular to the physics of extragalactic jets (Begelmann et al., 1984).

This Chapter is split into three parts. First, we will describe the equations of ideal RMHD and the equation of state used in our numerical implementation. We use the equations in the same form as Anile (1989), where a full derivation can be found. In the second Section we will explain the numerical methods used to solve these equations in time dependent simulations. And finally, in the third part, we will demonstrate how well our code solves various numerical test problems, and how it compares to other RMHD simulation codes.

2.1 Equations of ideal relativistic MHD

2.1.1 Units

The equations and the simulation code described in this section are written in natural units where the speed of light $c = 1$. The code itself is written in scale free form and the system of units is fixed by selecting a length scale and a scale for the rest mass density given in cgs units:

$$\rho[\mathrm{g/cm^3}] \; . \tag{2.1}$$

The thermodynamic pressure, p, is measured in units of

$$\rho c^2[\mathrm{dyn/cm^2}] \; , \tag{2.2}$$

and the specific internal energy, ε, in units of

$$c^2[\mathrm{erg/g}] \ . \tag{2.3}$$

All velocities are given in units of $[c]$. The units of magnetic fields in the laboratory frame are given by

$$\sqrt{\rho c^2}[\sqrt{4\pi}\mathrm{G(auss)}] \tag{2.4}$$

to avoid cluttering of the equations by factors of π.

2.1.2 The RMHD equations as a system of conservation laws

Throughout the following the metric will be $g^{\alpha\beta} = \mathrm{diag}(-1, 1, 1, 1)$ unless stated otherwise. The usual conventions for indices and summation will be used. Roman indices run from 1 to 3 (or x, y, z in Cartesian geometry), Greek indices run from 0 to 4. Three-vectors like the velocity, $\mathbf{v}$, or the laboratory frame magnetic field, $\mathbf{B}$, are set in boldface.

The velocity four vector is

$$u^\alpha = W(1, v^x, v^y, v^z) \ , \tag{2.5}$$

where $W = 1/\sqrt{1-\mathbf{v}^2}$ is the Lorentz factor. The covariant magnetic field vector, b^α (lower case opposed to the upper case letter for the laboratory frame field) is given by

$$b^0 = W(\mathbf{v}\cdot\mathbf{B}) \ , \tag{2.6}$$

$$b^i = \frac{B^i}{W} + v^i b^0 \ . \tag{2.7}$$

Note that $|\mathbf{b}|^2 = b_\alpha b^\alpha = \frac{\mathbf{B}^2}{W^2} - (\mathbf{v}\cdot\mathbf{B})^2$. The covariant magnetic field vector is defined such that, in the infinite conductivity approximation, Ohm's law can be written as

$$b^\alpha u_\alpha = 0 \ , \tag{2.8}$$

which translates into a vanishing electric field in the fluid's rest frame.

The equations that describe the evolution of a relativistic magneto-fluid can be written in the form of conservation laws, the conservation of mass,

$$\partial_\alpha(\rho u^\alpha) = 0 \ , \tag{2.9}$$

and the conservation of total energy-momentum,

$$\partial_\alpha T^{\alpha\beta} = 0 \ , \tag{2.10}$$

where the energy-momentum tensor of a magnetic fluid is given by

$$T^{\alpha\beta} = \rho h^* u^\alpha u^\beta + p^* g^{\alpha\beta} - b^\alpha b^\beta \ . \tag{2.11}$$

Here h^* and p^* are the hydromagnetic specific enthalpy and the hydromagnetic total pressure, respectively, given by

$$h^* = h + \frac{|\mathbf{b}|^2}{\rho} = 1 + \varepsilon + \frac{p}{\rho} + \frac{|\mathbf{b}|^2}{\rho} \quad \text{and} \quad p^* = p + p_{mag} \,, \tag{2.12}$$

where ε denotes the specific internal energy, $h = 1 + \varepsilon + p/\rho$ is the specific enthalpy, and

$$p_{mag} = \frac{|\mathbf{b}|^2}{2} \tag{2.13}$$

is the magnetic pressure. The evolution of the magnetic field components is described by the relativistic induction equation

$$\partial_\alpha (u^\alpha b^\beta - u^\beta b^\alpha) = 0 \,, \tag{2.14}$$

the spatial part of which, in terms of the laboratory frame magnetic field, reads:

$$\frac{\partial \mathbf{B}}{\partial t} - \nabla \times (\mathbf{v} \times \mathbf{B}) = 0 \,. \tag{2.15}$$

Ideal RMHD assumes infinite conductivity of the plasma, thus $\frac{\partial \mathbf{E}}{\partial t} = 0$ and $\mathbf{E} = -\mathbf{v} \times \mathbf{B}$. The time component of Eq. (2.14) becomes the usual MHD constraint

$$\nabla \cdot \mathbf{B} = 0 \,, \tag{2.16}$$

which has to be fulfilled at all times. Equations (2.9), (2.10) and (2.14) provide the complete set of RMHD equations.

It is useful to introduce the *magnetisation parameter*, β, which is the ratio of magnetic to thermal gas pressure:

$$\beta = \frac{p_{mag}}{p} \,. \tag{2.17}$$

A value of $\beta = 1$ means that the magnetic field energy density equals (or is in *equipartition* with) the thermal energy density of the plasma. Following Appl & Camenzind (1988), we introduce another parameter that will prove useful in parameterising RMHD flows: the ratio of magnetic field energy density to that of the rest mass given by

$$\sigma = \frac{|\mathbf{b}|^2}{\rho} \,. \tag{2.18}$$

Then $h^* = h + \sigma$ and for $\sigma \gg h$, the magnetic field dominates h^*. This means that the Poynting flux in the first term of the energy-momentum tensor (2.11) will be much larger than the material energy flux. We have defined σ to be the inverse of the definition used by Appl & Camenzind (1988) or Komissarov (1999*b*). In this way both β and σ become large for large magnetic fields and zero for non-magnetised plasma.

The system of RMHD equations given by (2.9), (2.10), and (2.15) is closed by an equation of state (EOS):

$$p = p(\varepsilon, \rho) \ . \tag{2.19}$$

In the following we will use an ideal EOS with a constant adiabatic index, γ:

$$p = (\gamma - 1)\rho\varepsilon \ . \tag{2.20}$$

The speed of sound waves, c_s, can then be calculated from (e.g. Landau & Lifschitz, 1966)

$$hc_s^2 = \left.\frac{\partial p}{\partial \rho}\right|_\varepsilon + \frac{p}{\rho^2}\left.\frac{\partial p}{\partial \varepsilon}\right|_\rho \ , \tag{2.21}$$

thus

$$c_s = \sqrt{\frac{\gamma p}{\rho h}} \ . \tag{2.22}$$

In magnetic fluids, in addition to sound waves, another type of wave motion is possible, called *Alfvén waves* (e.g. Jackson, 1975). In RMHD, the Alfvén speed, c_a, is defined through (Anile, 1989)

$$c_a^2 = \frac{|\mathbf{b}|^2}{\rho h^*} = \frac{\sigma}{h + \sigma} \ . \tag{2.23}$$

There are three ways for a magnetised plasma to become relativistic: (1) when the flow velocity is close to c and therefore the Lorentz factor of the flow becomes much larger than one; (2) when the plasma is hot, i.e. $p \gg \rho$ such that the sound speed (2.22) becomes relativistic; and (3) when $|\mathbf{b}|^2 \gg \rho$, i.e. $\sigma \gg h$, such that the Alfvén speed (2.23) is close to c.

2.1.3 The equations in primitive variables

The RMHD system of partial differential equations can be cast in conservation form as follows

$$\partial_t \mathbf{U} + \partial_x \mathbf{F}^x + \partial_y \mathbf{F}^y + \partial_z \mathbf{F}^z = \mathbf{Q} \ , \tag{2.24}$$

where $\mathbf{U}$ is the vector of *conserved quantities*, the $\mathbf{F}^i$ are the vectors of *fluxes*, and $\mathbf{Q}$ is the vector of source terms (see Sec 2.1.4). Written in terms of *primitive variables*,

$$\mathbf{V} = (\rho, v^x, v^y, v^z, p, B^x, B^y, B^z)^T \ , \tag{2.25}$$

and using the symbols $D, \mathbf{S}$ and τ for the conserved rest mass density, momentum density vector and energy density measured in the laboratory frame, respectively,

the conserved quantities, $\mathbf{U}$, read

$$\mathbf{U} = \begin{pmatrix} D \\ S^x \\ S^y \\ S^z \\ \tau \\ B^x \\ B^y \\ B^z \end{pmatrix} \equiv \begin{pmatrix} \rho W \\ \rho h^* W^2 v^x - b^0 b^x \\ \rho h^* W^2 v^y - b^0 b^y \\ \rho h^* W^2 v^z - b^0 b^z \\ \rho h^* W^2 - p^* - b^0 b^0 - \rho W \\ B^x \\ B^y \\ B^z \end{pmatrix} . \tag{2.26}$$

The fluxes, $\mathbf{F}^i$, are then

$$\mathbf{F}^i = \begin{pmatrix} \rho W v^i \\ \rho h^* W^2 v^i v^x + p^* \delta^i_x - b^i b^x \\ \rho h^* W^2 v^i v^y + p^* \delta^i_y - b^i b^y \\ \rho h^* W^2 v^i v^z + p^* \delta^i_z - b^i b^z \\ \rho h^* W^2 v^i - b^0 b^i - \rho W v^i \\ v^i B^x - B^i v^x \\ v^i B^y - B^i v^y \\ v^i B^z - B^i v^z \end{pmatrix} . \tag{2.27}$$

Note that while system (2.24) consists of eight conservation equations, only seven components of the fluxes, F^i, are non-trivial. Owing to the antisymmetric character of the induction equation (2.15) the flux of B^i in i-direction is always zero. For example in the x direction the evolution equation for B^x reads

$$\partial_t B_x = \partial_x (v^x B^x - B^x v^x) = 0 . \tag{2.28}$$

2.1.4 The equations in cylindrical coordinates

For jet applications where axisymmetry is assumed (Chapters 3 and 4), Eq. (2.24) has to be written in cylindrical coordinates. This will yield the vector of geometrical source terms, $\mathbf{Q}$, and the appropriate geometrical factors for numerical implementation.

Using cylindrical coordinates (r, ϕ, z) the metric becomes

$$g_{\alpha\beta} = \mathrm{diag}(-1, 1, r^2, 1) . \tag{2.29}$$

Then the mass conservation equation (2.9) reads

$$\partial_0 D + \frac{1}{r}\partial_r \left(r D v^r\right) + \frac{1}{r}\partial_\phi (D v^\phi) + \partial_z (D v^z) = 0 , \tag{2.30}$$

and the momentum and energy conservation equations (2.10) become

$$\partial_0 S^r + \frac{1}{r}\partial_r\left[r\left(\rho h^* W^2 v^r v^r + p^* - b^r b^r\right)\right] + \frac{1}{r}\partial_\phi\left(\rho h^* W^2 v^r v^\phi - b^r b^\phi\right) + \partial_z\left(\rho h^* W^2 v^r v^z - b^r b^z\right) = \frac{\rho h^* W^2 v^\phi v^\phi + p^* - b^\phi b^\phi}{r}\,, \tag{2.31}$$

$$\partial_0 S^z + \frac{1}{r}\partial_r\left[r\left(\rho h^* W^2 v^z v^r - b^r b^z\right)\right] + \frac{1}{r}\partial_\phi\left(\rho h^* W^2 v^z v^\phi - b^z b^\phi\right) + \partial_z\left(\rho h^* W^2 v^z v^z + p^* - b^z b^z\right) = 0\,, \tag{2.32}$$

$$\partial_0 S^\phi + \frac{1}{r}\partial_r\left[r\left(\rho h^* W^2 v^\phi v^r - b^\phi b^r\right)\right] + \frac{1}{r}\partial_\phi\left(\rho h^* W^2 v^\phi v^\phi + p^* - b^\phi b^\phi\right) + \partial_z\left(\rho h^* W^2 v^\phi v^z - b^\phi b^z\right) = -\frac{\rho h^* W^2 v^r v^\phi - b^r b^\phi}{r}\,, \tag{2.33}$$

$$\partial_0 \tau + \frac{1}{r}\partial_r\left[r\left(\rho h^* W^2 v^r - b^r b^0 - D v^r\right)\right] + \frac{1}{r}\partial_\phi\left(\rho h^* W^2 v^\phi - b^\phi b^0 - D v^\phi\right) + \partial_z\left(\rho h^* W^2 v^z - b^z b^0 - D v^z\right) = 0\,. \tag{2.34}$$

Accordingly, written component-wise, the induction equation (2.15) in cylindrical coordinates reads

$$\partial_0 B^r + \partial_z(v^z B^r - v^r B^z) + \frac{1}{r}\partial_\phi(v^\phi B^r - v^r B^\phi) = 0\,, \tag{2.35}$$

$$\partial_0 B^z + \frac{1}{r}\partial_r\left[r(v^r B^z - v^z B^r)\right] + \frac{1}{r}\partial_\phi(v^\phi B^z - v^z B^\phi) = 0\,, \tag{2.36}$$

$$\partial_0 B^\phi + \frac{1}{r}\partial_r\left[r(v^r B^\phi - v^\phi B^r)\right] + \partial_z(v^z B^\phi - v^\phi B^z) = \frac{B^\phi v^r - B^r v^\phi}{r}\,. \tag{2.37}$$

Equations (2.30)-(2.37) cast the RMHD system into cylindrical coordinates, where geometrical source terms occur in the equations for the r- and ϕ-momentum, and for the ϕ magnetic field. Thus the vector of source terms is

$$\mathbf{Q} = \left(0, \frac{\rho h^* W^2 v^\phi v^\phi + p^* - b^\phi b^\phi}{r}, 0, -\frac{\rho h^* W^2 v^r v^\phi - b^r b^\phi}{r}, 0, 0, 0, \frac{B^\phi v^r - B^r v^\phi}{r}\right)^T. \tag{2.38}$$

2.1.5 Spectral decomposition

Wave speeds

In order to compute the eigenvalues, λ, of the one dimensional RMHD system

$$\partial_t \mathbf{U} + \partial_x \mathbf{F}^x = 0\,, \tag{2.39}$$

where $\mathbf{U}$ and $\mathbf{F}^x$ are given by (2.26) and (2.27), respectively, one has to solve the characteristic polynomial

$$|\mathcal{A}^1 - \lambda \mathcal{A}^0| = 0\,, \tag{2.40}$$

where $\mathcal{A}^1$ and $\mathcal{A}^0$ are Jacobian matrices of system defined as

$$\mathcal{A}^1_{ij} = \frac{\partial \mathbf{F}^x_i}{\partial \mathbf{V}_j} \quad \text{and} \quad \mathcal{A}^0_{ij} = \frac{\partial \mathbf{U}_i}{\partial \mathbf{V}_j} \, . \tag{2.41}$$

Here $i, j = 1 \ldots 7$ are the components in the vectors (2.25), (2.26) and (2.27). (2.40) yields a polynomial of degree seven, the solution of which is non-trivial.

In order to simplify the problem Anile (1989) has used a covariant system of the RMHD equations to derive eigenvalues and eigenvectors. By augmenting three non-physical quantities the system becomes fully covariant, a fact which is skillfully exploited by Anile in finding a solution. After solving the system the waves corresponding to the augmented variables can be discarded as unphysical. The remaining seven waves are physical. Anile derives the following expressions for the eigenvalues: the matter/entropy wave,

$$\lambda_0 = v_x \, , \tag{2.42}$$

the two Alfvén (a) waves,

$$\lambda^{\pm}_a = \frac{b^1 \pm u^1 \sqrt{\rho h^*}}{b^0 \pm u^0 \sqrt{\rho h^*}} \, , \tag{2.43}$$

and the four magnetosonic (ms) waves (two slow and two fast ones), which are the roots of a quartic polynomial in λ_{ms},

$$C_4 \lambda^4_{ms} + C_3 \lambda^3_{ms} + C_2 \lambda^2_{ms} + C_1 \lambda_{ms} + C_0 = 0 \, , \tag{2.44}$$

where

$$C_4 = 1 - \omega^2 \mathbf{v}^2 - \frac{(b^0)^2 c_s^2}{\rho h^* W^4} \, , \tag{2.45}$$

$$C_3 = -4 v_x (1 - \omega^2) - \frac{2 v_x \omega^2}{W^2} + \frac{2 b^0 b^1 c_s^2}{\rho h^* W^4} \, , \tag{2.46}$$

$$C_2 = 6 v_x^2 (1 - \omega^2) - \frac{(1 - v_x^2)\omega^2}{W^2} + \frac{((b^0)^2 - (b^1)^2) c_s^2}{\rho h^* W^4} \, , \tag{2.47}$$

$$C_1 = -4 v_x^3 (1 - \omega^2) + \frac{2 v_x \omega^2}{W^2} - \frac{2 b^0 b^1 c_s^2}{\rho h^* W^4} \quad \text{, and} \tag{2.48}$$

$$C_0 = v_x^4 (1 - \omega^2) - \frac{v_x^2 \omega^2}{W^2} + \frac{(b^1)^2 c_s^2}{\rho h^* W^4} \, . \tag{2.49}$$

ω is a combination of sound and Alfvén speeds defined as $\omega^2 = c_s^2 + c_a^2 - c_s^2 c_a^2$.

Unfortunately, equation (2.44) does not allow for simple analytic expressions for the fast and slow magnetosonic wave speeds, and therefore has to be solved numerically (see Sec. 2.2.5). However, the eigenvalues can always be ordered

$$\lambda^-_{fms} \leq \lambda^-_a \leq \lambda^-_{sms} \leq \lambda_0 \leq \lambda^+_{sms} \leq \lambda^+_a \leq \lambda^+_{fms} \, , \tag{2.50}$$

where fms and sms mean fast and slow magnetosonic, respectively.

Eigenvectors

Once the eigenvalues of the system are known one can compute the right eigenvectors by solving the set of equations

$$(\mathcal{B} - \lambda\mathcal{I}) \cdot \mathbf{r} = 0 \,, \tag{2.51}$$

where $\mathcal{B}$ is the Jacobian matrix $\mathcal{B} = \frac{\partial \mathbf{F}^x}{\partial \mathbf{U}} = \mathcal{A}^1 \cdot (\mathcal{A}^0)^{-1}$ and $\mathcal{I}$ is the unitary matrix. Since it is difficult to derive $\mathcal{B}$ in analytical form, it is easier to solve the corresponding system

$$(\mathcal{A}^1 - \lambda\mathcal{A}^0) \cdot \mathbf{r}^{'} = 0 \tag{2.52}$$

and afterwards multiply the resulting vectors by $(\mathcal{A}^0)^{-1}$.

The eigenvectors provided by Anile (1989) in the ten by ten augmented system can easily be transformed to a seven by seven primitive variable system, see e.g. Balsara (2001). The eigenvectors corresponding to the four magnetosonic waves can only be given as generic expressions which depend on the eigenvalues themselves. It serves no purpose to list these expressions here, so we refer the reader to the above mentioned publications.

Degeneracies

A system is called strictly hyperbolic if all eigenvalues of its characteristic problem are real and distinct. In RMHD there exist degeneracies where system (2.39) is not strictly hyperbolic: (i) in the case where $B^x = 0$, the slow magnetosonic and the Alfvén waves have the same speed as the entropy wave; (ii) in the case where $B^y = B^z = 0$ in the fluid's rest frame (but not in the laboratory frame due to relativistic aberration, see Komissarov, 1999a) the Alfvén waves have the same speeds as the slow and/or fast magnetosonic waves depending on the relation between c_a and c_s. For the system to remain hyperbolic all degenerate eigenvalues have to be paired with linearly independent eigenvectors.

For the first degenerate case, $B^x = 0$ in Eq. (2.39), we can find an analytic solution to the eigenvalue problem, Eq. (2.40). In that case both the Alfvén waves and the slow magnetosonic waves degenerate to the material wave. Equation (2.44) then becomes a quadratic equation in λ the solutions of which are the two fast magnetosonic waves. The complete set of eigenvalues then is given by

$$\lambda_0 = v_x \quad \text{(five times degenerate)} \tag{2.53}$$

and

$$\lambda^{\pm}_{fms} = \frac{v_x(1-\omega^2) \pm \sqrt{\big((\mathbf{v}^2-1)\omega^2 + R\big)\big((\mathbf{v}^2 - v_x^2)\omega^2 + v_x^2 - 1 + R\big)}}{1 - \mathbf{v}^2\omega^2 - R} \tag{2.54}$$

with $R = \frac{c_s^2(\mathbf{v}\cdot\mathbf{B})^2}{\rho h^* W^2}$ and $\omega = c_s^2 + c_a^2 - c_s^2 c_a^2$. The solution of Eq. (2.52) is also analytic for $B^x = 0$, although one has to be careful to chose five linearly independent eigenvectors

for the five-fold degenerate eigenvalue λ_0. However, we do not include the expressions for the eigenvectors here, because we will not use them in our scheme (see Sec. 2.2.5).

In the second degenerate case the characteristic polynomial (2.40) does not have such simple solutions.

2.2 Numerical techniques

In the following we will restrict all equations to two spatial dimensions for two reasons: (a) readability, and (b) all of our applications discussed later in this work will be 2D. Generalisation to 3D is straightforward, and in principle, all the methods described here work in 3D, too.

2.2.1 Discrete space-time

The equations of RMHD (2.24) are solved numerically in a discrete sample of events in space-time. Space is discretised into a grid of zones or cells, the positions of their centres denoted by lower integer indices i and j. Time is divided into steps which are denoted by an upper index n, such that t^n stands for the time after the nth time step. For example on a 2D Cartesian grid indices (i, j) correspond to coordinates (x, y), while on a 2D cylindrical grid used for the simulations described in Chapters 3 and 4 indices (i, j) denote the r and z coordinates, respectively. The vector $\mathbf{U}(r_i, z_j, t^n)$ in grid zone (i, j) at time t^n is written as $U^n_{i,j}$. Cell interfaces are denoted by half integer indices, e.g., the flux across the interface between zone (i, j) and $(i + 1, j)$ at time t^n is denoted by $\mathbf{F}^n_{i+1/2,j}$. For clarity, the superscript n will be dropped whenever all variables are given at the same time step.

2.2.2 Conservative method

The magnetohydrodynamic equations are solved in their conservation form which is obtained by integrating (2.24) over a finite volume, V, with surface $S(V)$ (hence conservative methods are also called *finite volume* methods). For a component, $U_{(k)}$ of the state vector $\mathbf{U}$ the integral reads

$$\frac{\partial}{\partial t}\int_V U_{(k)}dV + \oint_{S(V)} \mathbf{F}_{(k)} \cdot \mathbf{dS} = \int_V Q_k dV \text{ , where } \quad \mathbf{F}_{(k)} = \begin{pmatrix} (F_{(k)})^x \\ (F_{(k)})^y \end{pmatrix}. \quad (2.55)$$

Then the densities of mass, momentum, energy, and magnetic field in that volume can only change in time by the corresponding fluxes across the volume's boundary. In this way conservation of the state vector $\mathbf{U}$ is implemented naturally and exactly.

The discretisation of Eqs. (2.24) can be written down, following the method of lines (e.g., LeVeque, 1991), such that the time variation of the state vector $\mathbf{U}$ within a numerical cell reads

$$\frac{\mathbf{dU}_{i,j}}{dt} = -\frac{1}{\Delta x}(\widehat{\mathbf{F}}^x_{i+(1/2),j} - \widehat{\mathbf{F}}^x_{i-(1/2),j}) - \frac{1}{\Delta y}(\widehat{\mathbf{F}}^y_{i,j+(1/2)} - \widehat{\mathbf{F}}^y_{i,j-(1/2)}) + \mathbf{Q}_{i,j} \equiv \mathcal{D}(\mathbf{U}) \text{ ,}$$

(2.56)

where $\mathcal{D}(\mathbf{U})$ is the spatial operator of the method. Thus the mean value of the state vector $\mathbf{U}_{i,j}$ in the corresponding cell is calculated be considering the numerical fluxes (denoted by a hat symbol) across the cell interfaces, $\widehat{\mathbf{F}}^{x}_{i+(1/2),j}$ and $\widehat{\mathbf{F}}^{y}_{i,j+(1/2)}$, and the mean vector of sources in that cell, $\mathbf{Q}_{i,j}$.

For the computation of the numerical fluxes a Godunov method can be used (e.g., LeVeque, 1998), which exploits the Riemann problem discussed in section 2.2.3. In the case of the original Godunov method the spatial distributions of the states are approximated by piecewise constant functions, i.e., the states are assumed to be constant inside a grid zone. Thus discontinuities at the cell interfaces are created, the breakup of which can be addressed by solving Riemann problems and will be explained below in detail. The numerical fluxes are then obtained by solving these Riemann problems at each cell interface approximately (see section 2.2.5). In this way discontinuities in the fluid are captured naturally, and are resolved within a few grid zones. Hence, methods of this type are also called *high–resolution shock–capturing* schemes (Martí & Müller, 1999).

In order to avoid numerical instabilities and unphysical solutions, the Courant-Friedrichs-Lewy (CFL) condition for the size of the time step has to be taken into account (LeVeque, 1991): information must not travel further than one grid zone within one time step, i.e., the flux across a cell boundary may only change the states in the adjacent cells. If $v_{max}(t^n)$ is the maximum physical speed in the computational domain and Δx the minimal size of a zone, then the following relation must be fulfilled:

$$\Delta t = t^{n+1} - t^n < \min\left(\Delta x / v_{max}(t^n)\right) \equiv \Delta t_{\rm cfl} \ . \tag{2.57}$$

In actual applications the time step must be further decreased to compensate errors introduced by the spatial interpolation scheme (Sec. 2.2.6). One introduces a scale factor, the so-called CFL number, $f_{\rm cfl} < 1$, such that

$$\Delta t = f_{\rm cfl} \Delta t_{\rm cfl} \ . \tag{2.58}$$

$f_{\rm cfl}$ is usually chosen between 0.5 and 0.8.

2.2.3 The Riemann problem

The hydrodynamic Riemann problem consists of computing the breakup of a discontinuity, which initially separates two arbitrary constant states $\mathbf{V}_L$ (left) and $\mathbf{V}_R$ (right) in a gas, where $\mathbf{V} = \{p, \rho, \mathbf{v}\}$. Imagine an infinitely thin membrane separating the two states at point $x_0 = x_D$ (See Fig. 2.1, top panel. $L \equiv 1$ and $R \equiv 5$). At time t_0 the membrane is suddenly removed and the discontinuity breaks up. The solution of this problem is self-similar: it only depends on the two constant states defining the discontinuity, and on the ratio $(x - x_0)/(t - t_0)$. The discontinuity decays into two elementary non-linear waves (shocks or rarefaction waves). Between these waves two new constant states $\mathbf{V}_{L*}$ and $\mathbf{V}_{L*}$ ($L* \equiv 3$ and $R* \equiv 4$ in Fig. 2.1) appear, separated by a contact discontinuity which moves with the fluid. While

the density shows a jump across this contact discontinuity, pressure and velocity are continuous. The self-similar character of the flow through the rarefaction waves together with the Rankine–Hugoniot jump conditions across shocks (Landau & Lifschitz, 1966) provide the equations to relate the intermediate states (the $*$-states) with their corresponding initial states. In that way the fluid flow velocity in the intermediate states can be expressed in terms of the pressure. This can be used to derive an exact solution for the relativistic Riemann problem (Martí & Müller, 1994).

However, in RMHD, the initial states contain two more variables, B^y and B^z, i.e. $\mathbf{V} = \{p, \rho, \mathbf{v}, B^y, B^z\}$. Therefore the discontinuity breaks up into seven states instead of five, so far no general analytical solution has been found (see Sec. 2.1.5).

2.2.4 Directional splitting

In multi–dimensional numerical hydrodynamics it is common to treat each spatial dimension separately. In the case of a Godunov method this means that the computation of the fluxes is split up into *sweeps*. On a 2D cylindrical grid two sweeps are required, in the first sweep all fluxes in the radial direction are computed, and in a second sweep all fluxes in axial direction. This method is called *directional splitting*. Hence, a routine which solves the Riemann problems at the cell interfaces only has to handle one dimensional "sub-grids" and is therefore very efficient computationally. In addition the approximate Riemann solver discussed below only needs to be implemented for a reduced one dimensional system. For example, in the x-direction it is of the form

$$\frac{\partial \mathbf{U}}{\partial t} + \frac{\partial \mathbf{F}(\mathbf{U})}{\partial x} = 0 \,. \tag{2.59}$$

The hydrodynamic conserved quantities are also updated sweep-by-sweep, i.e. the contribution of fluxes from the different directions are added one after the other. The magnetic fields, however, can not be updated in a split fashion because the antisymmetric form of the induction equation (2.15) leads to a coupling of the directions perpendicular to the sweep. Ignoring this coupling generates (numerical) magnetic monopoles. Instead magnetic fluxes are saved into arrays, and are used at the end of a time step to update the fields using an unsplit formula, which explicitly keeps $\nabla \cdot \mathbf{B} = 0$ (see Sec. 2.2.9).

Another important advantage of directional splitting is that the spatial interpolation algorithms discussed in section 2.2.6 are much easier to implement in 1D than in 2D.

2.2.5 An approximate Riemann solver — HLLE

Approximate Riemann solvers are based on the linearisation of (2.59),

$$\frac{\partial \mathbf{U}}{\partial t} + A\frac{\partial \mathbf{U}}{\partial x} = 0 \,, \tag{2.60}$$

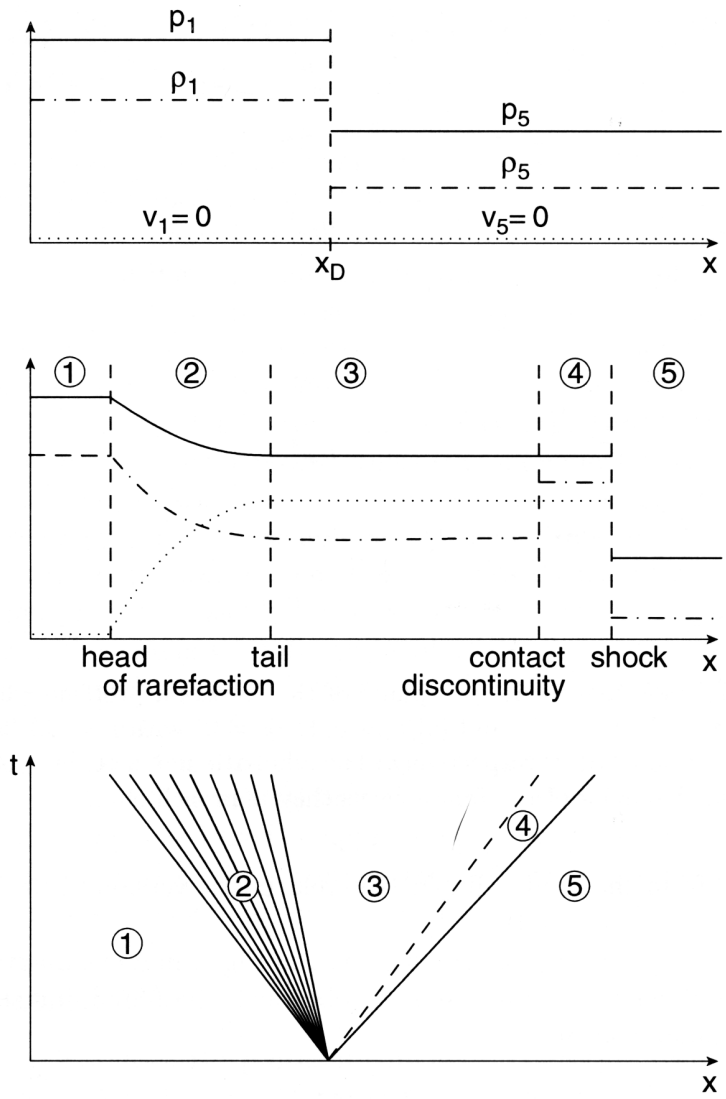

Figure 2.1: Schematic explanation of a hydrodynamic Riemann problem. The top figure shows the initial state ($t < t_0$) which consists of two constant states 1 and 5: $p_1 > p_5$, $\rho_1 > \rho_5$ and $v_1 = v_5 = 0$ separated by a diaphragm at $x_0 = x_D$. The middle diagram shows the flow pattern after the breakup of the discontinuity. The self-similar evolution of the flow pattern is displayed in the space-time diagram (bottom figure) with a shock (solid line) and the contact discontinuity (dashed line) moving to the right and rarefaction waves propagating to the left (from Martí & Müller, 1999).

where $A = const$ is an approximation of the Jacobian matrix $\frac{\partial \mathbf{F}(\mathbf{U})}{\partial \mathbf{U}}$.

If the system of seven equations (2.59) is hyperbolic, A is diagonalisable and has only real eigenvalues, λ_p, $p = 1 \ldots 7$, with a complete set of left and right eigenvectors, $\mathbf{l}^p$ and $\mathbf{r}^p$, respectively (LeVeque, 1998). Multiplying system (2.59) by $L = (\mathbf{l}^1, \ldots, \mathbf{l}^7)$ from the left yields the decoupled system of advection equations

$$\frac{\partial \mathbf{W}}{\partial t} + \Lambda \frac{\partial \mathbf{W}}{\partial x} = 0 \ , \tag{2.61}$$

where $\mathbf{W} = L\mathbf{U}$ is the new vector of characteristic states and $\Lambda = LAL^{-1} = \mathrm{diag}(\lambda_1, \ldots, \lambda_7)$. The solution for every component, w_p, of $\mathbf{W}$ is simply $w_p(x,t) = w_p(x - \lambda_p t, 0)$, because in the linear approximation, information propagates along straight lines, $x = \lambda_p t$, called *characteristics*. Transforming back to $\mathbf{U} = L^{-1}\mathbf{W}$ yields

$$\mathbf{U}(x,t) = \sum_{p=1}^{7} w_p(x - \lambda_p t, 0)\mathbf{r}^p \quad \text{and} \tag{2.62}$$

$$\mathbf{F}(x,t) = \sum_{p=1}^{7} \lambda_p w_p(x - \lambda_p t, 0)\mathbf{r}^p \ . \tag{2.63}$$

In a Godunov method the initial states $\mathbf{U_L}$ and $\mathbf{U_R}$ on the left and right side of a cell interface are given. For the computation of the resulting numerical fluxes ($\widehat{\mathbf{F}}$ in equation (2.56)) across the cell interface we use the HLLE flux formula (Harten et al., 1983; Einfeldt, 1988). It is based on the calculation of the two fastest signal velocities perturbing the initial states on both sides of the interface:

$$\widehat{\mathbf{F}}(\mathbf{U_L}, \mathbf{U_R}) = \psi_+ \mathbf{F}(\mathbf{U_L}) - \psi_- \mathbf{F}(\mathbf{U_R}) + \frac{\psi_+ - \psi_-}{\psi_+ \psi_-}(\mathbf{U_R} - \mathbf{U_L}) \ , \tag{2.64}$$

where, in our case,

$$\psi_+ = \max(\lambda_{p,L}, \lambda_{p,R}) \quad \text{and} \quad \psi_- = \min(\lambda_{p,L}, \lambda_{p,R}), \quad p = 1, \ldots, 7 \tag{2.65}$$

are the minimum and maximum of the characteristic wave speeds, λ_p, of the local Riemann problem.

As described in Sec. 2.1.5 these speeds can be computed by solving the quartic equation (2.44). We have found that the best procedure to obtain the four solutions is the following: (1) first we compute the two fast magnetosonic wave speeds employing a Newton-Raphson iteration scheme; (2) then we reduce the quartic to a quadratic equation by polynomial division; (3) finally we get the two slow magnetosonic wave speeds by another set of Newton-Raphson iterations in combination with a bisection scheme (Press et al., 1992). However, these methods lead to severe numerical problems and will make the solver unstable for high Lorentz factors. This is illustrated in Fig. 2.2 where we have plotted the quartic in the relevant range for a flow velocity of $v^x = 0.999$ (i.e. Lorentz factor $W \approx 20$). In this case, the combination of two facts make it difficult to find the four zeroes by numerical iteration schemes: all of them lie within 0.1% of each other, i.e. the quartic is less than 10^{-14} from zero for a relatively broad interval such that it reaches the machine precision of $\mathcal{P} = \mathcal{O}(10^{-16})$ and

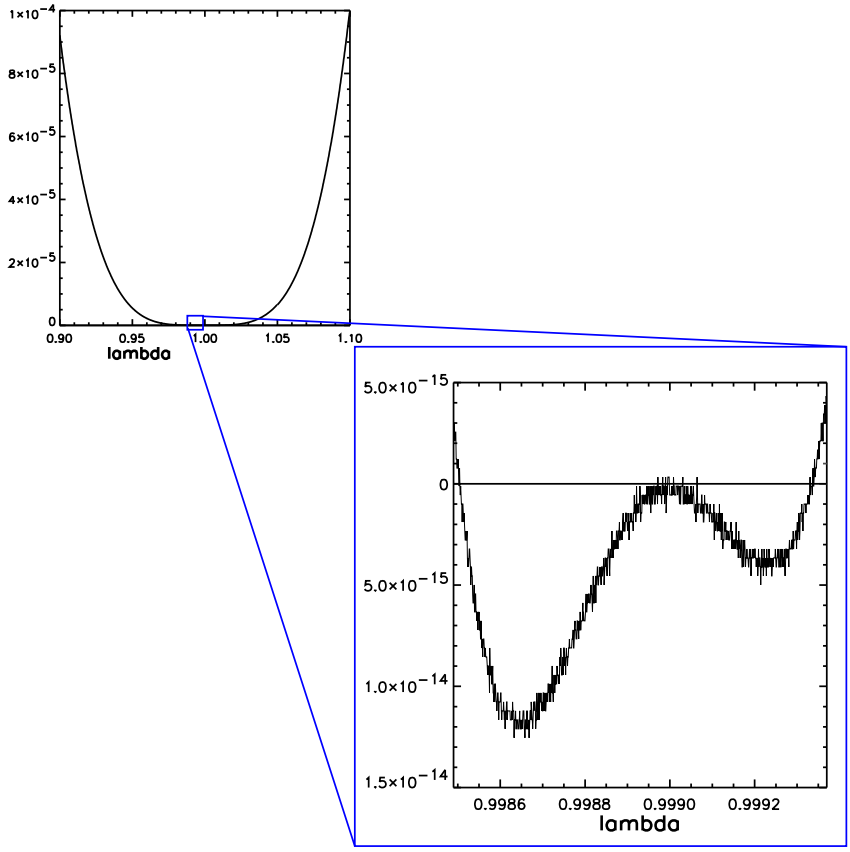

Figure 2.2: Plot of the quartic equation (2.44) for a Lorentz factor of 20. Due to limitations by machine precision of $\mathcal{P} = \mathcal{O}(10^{-16})$ the equation has more than four solutions. The line is not smooth but juggles around the true, smooth curve by the amount $\mathcal{P}$.

numerically has more than four zeros. Using quadruple precision ($\mathcal{P} = \mathcal{O}(10^{-32})$) does not merit the considerable increase in computation time, since it only shifts the problem to slightly higher Lorentz factors. Del Zanna et al. (2003) claim that an analytical solution of the full quartic yields better results than a numerical one, but we have found that this is not the case. Since the former involves square roots of cubic roots it suffers even more from the problem of machine precision, returning signal velocities that are larger than one in many test cases with high Lorentz factors in addition to being slower than the numerical solution.

Therefore, instead of dealing with all these difficulties, and in order to get a robust solver, we use the analytical solution of the two fast magnetosonic waves, λ_{ana}, in the first degenerate case of the RMHD system given by expression (2.54). This expression always returns values lower than the speed of light, even in the most extreme relativistic cases examined. In addition, we have found through numerical testing that these values are lower and upper bounds to the real fastest and slowest magnetosonic wave speeds (as computed by the numerical solution of the quartic, λ_{num}), respectively. This property makes them ideal for use in the HLLE flux formula (2.64). Figure 2.3 shows the relative difference between λ_{ana} and λ_{num} for the right

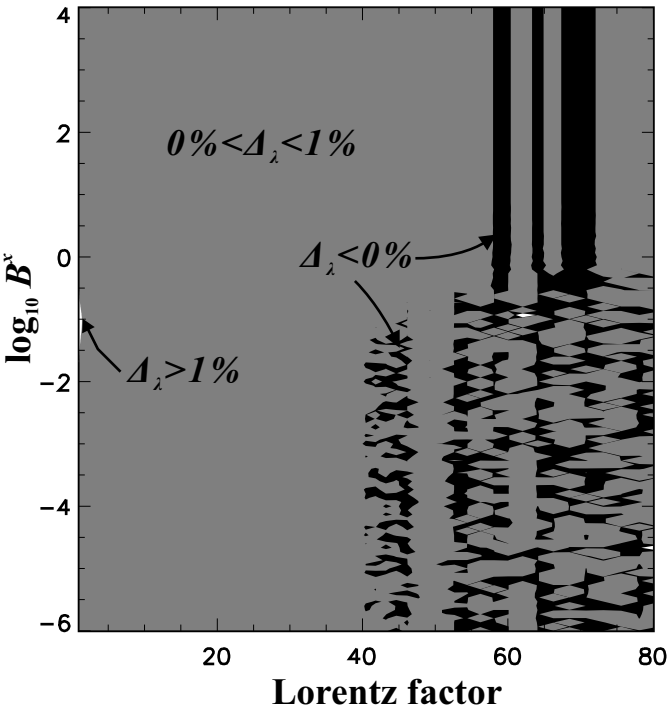

Figure 2.3: Contour plot of the relative difference between the analytic fast magnetosonic eigenvalue and the numerical solution of the system's quartic equation, Δ_λ. In the white region $\Delta_\lambda > 1\%$, in the grey region $0 < \Delta_\lambda \leq 1\%$ and in the black region $\Delta_\lambda \leq 0$. This plot illustrates that the numerical solution becomes unreliable for $W > 40$, where it sporadically assumes values larger than the speed of light.

going fast magnetosonic wave speed,

$$\Delta_\lambda = \frac{\lambda_{ana} - \lambda_{num}}{\lambda_{ana}} \,. \tag{2.66}$$

The plot covers a large fraction of the parameter space by varying B^x and $v^x = v^y$, with $p = 0.01$, $\rho = 0.1$, $v^z = 0$, and $B^y = B^z = 1$. It shows that λ_{ana} is an upper bound to λ_{num} in all the grey and white areas of the parameter space. Moreover, we can see that the numerical solution fails for Lorentz factors $W > 40$, where it sporadically assumes values larger than the speed of light (the black areas in Fig. 2.3).

The complexities described above together with the fact that the RMHD system is not strictly hyperbolic (see Sec. 2.1.5) make it very difficult to implement more refined flux formulas like Roe-type solvers (Roe, 1981), or Marquina's flux (Donat & Marquina, 1996), because all of them make use of the complete set of eigenvalues and eigenvectors (see Aloy et al., 1999*c*, for an overview). Since the eigenvectors depend on the eigenvalues, inaccurate values for the latter will lead to inaccurate results of the former, thus making any scheme unstable, which uses eigenvectors to compute numerical fluxes. The regions in the phase space where the degeneracies of the system occur will lead to further instabilities. Our implementation of the HLLE flux (2.64) combined with well behaved expressions for the fastest signal speeds does not suffer from these problems, and is also computationally much more efficient than any method that makes use of the full spectral decomposition.

2.2.6 Spatial interpolation

The original Godunov method uses piecewise constant functions to approximate the spatial distribution of the variables, thus setting the spatial accuracy of the code to first order, which means that errors of discretisation are of the order $\mathcal{O}(\Delta x)$. In order to increase the accuracy to second or third order (discretisation errors $\mathcal{O}(\Delta x^2)$ or $\mathcal{O}(\Delta x^3)$), the zone-averaged values of the primitive variables, $\mathbf{V} = \{p, \rho, \mathbf{v}, \mathbf{B}\}$, are interpolated within the cells (Toro, 1997). This is achieved by using a piecewise linear method or a piecewise parabolic method (Colella & Woodward, 1984), respectively. Since the primitive variables are needed in the equation of state (2.20), interpolating them instead of the conserved ones has several advantages: (i) it is less time consuming as the primitives only need to be recovered (see 2.2.8) once per sub time step as opposed to every time when the equation of state needs to be evaluated; (ii) the interpolated states can be checked for thermodynamic consistency; and (iii) the sound speed and other derived thermodynamic quantities are straightforwardly obtained.

Piecewise linear method (PLM)

We use a modified version of the *minmod* linear inter-cell interpolation algorithm (e.g. LeVeque, 1991). For every variable a_i in zone i we construct a slope, Δ_i:

$$s_+ = \frac{a_{i+1} - a_i}{x_{i+1} - x_i} \ , \quad s_- = \frac{a_i - a_{i-1}}{x_i - x_{i-1}} \quad \text{and} \tag{2.67}$$

$$\Delta_i = 0.5 \ (\text{sign}(s_+) + \text{sign}(s_-)) \ \min(|s_+|, |s_-|) \ . \tag{2.68}$$

Values at the interface $i + 1/2$ are then computed according to

$$a_{i+1/2,L} = a_i + \Delta_i (x_{i+1/2} - x_i) \quad , \tag{2.69}$$

$$a_{i+1/2,R} = a_{i+1} + \Delta_{i+1} (x_{i+1/2} - x_{i+1}) \ . \tag{2.70}$$

For conserving monotonicity of the data, $\Delta_i = 0$ where local maxima and minima of the variable occur, i.e. the scheme switches back first order piecewise constant data.

We apply this algorithm to the variables

$$\{\ln \rho, \ln p, W\mathbf{v}, \mathbf{B}\} \ . \tag{2.71}$$

A further modification of the original minmod algorithm for RMHD applications is to limit the absolute value of the slope to 2.0 for the interpolation of $\ln \rho$ and $\ln p$ in those zones where the magnetisation parameter β (2.17) is larger than a certain threshold (between 4 and 10 in our applications).

Piecewise parabolic method (PPM)

The explicit algorithm used here is described in detail in Martí & Müller (1996). It was developed and tuned for RHD.

For each zone i the quartic polynomial which has zone-averaged values a_{i-2}, a_{i-1}, a_i, a_{i+1}, a_{i+2} is obtained, where a is the variable to be reconstructed. The polynomial then interpolates the structure in the zone and provides the values at the left and right interfaces of the zones, $a_{L,i}$ and $a_{R,i}$. These reconstructed values are then modified such that the parabolic profile defined by $a_{L,i}$, $a_{R,i}$ and a_i becomes monotonic inside the zone. The modified, interpolated values at the zone interfaces are then used to calculate the corresponding conserved variables which are the input values of the local Riemann problem solved by (2.64). Near contact discontinuities the interpolation procedure is slightly modified to produce narrower jumps. The scheme switches locally to a piecewise constant approximation in the vicinity of shocks in order to avoid spurious post shock oscillations (Appendix I in Martí & Müller, 1996).

2.2.7 Time integration

Time integration of equation (2.56) is done using a multi-step Runge–Kutta algorithm developed by Shu & Osher (1988) which provides third order accurate integration in time. Our implementation also includes a second order accurate version of the algorithm. Dropping the vector notation from (2.56), the update procedure of the states from U^n to U^{n+1} is divided into three Runge–Kutta steps:

$$U' = U^n + \Delta t \mathcal{D}(U^n) \,, \tag{2.72}$$

$$U'' = \frac{1}{4}(3U^n + (U' + \Delta t \mathcal{D}(U'))) \,, \tag{2.73}$$

$$U^{n+1} = \frac{1}{3}(U^n + 2(U'' + \Delta t \mathcal{D}(U''))) \,. \tag{2.74}$$

Important advantages of the Shu & Osher scheme (2.72)–(2.74) are that it preserves the total variation diminishing (TVD) property of the method, and that it only requires the information of the previous time step, and therefore needs less memory than the generic third order Runge–Kutta algorithm.

2.2.8 Recovery of primitive variables

The code evolves the conserved quantities $\{D, \mathbf{S}, \tau, \mathbf{B}\}$ and not the primitive variables $\{p, \rho, \varepsilon, \mathbf{v}, \mathbf{B}\}$. Therefore an algorithm has to be included, which computes the latter from the zone-averaged values of the former set. Since the conserved quantities can be written in terms of the primitives in analytic, closed form, but not the other way round, one has to employ numerical iteration algorithms.

We use (2.26) and (2.20) to construct two functions of the Lorentz factor, W, and the auxiliary variable $Z \equiv DW(1 + \gamma\varepsilon)$,

$$\mathcal{F}_1(Z, W) = \frac{\tau + D}{1 + \mathbf{B}^2} - \frac{Z + \mathbf{B}^2}{1 + \mathbf{B}^2} + \frac{(\mathbf{B} \cdot \mathbf{S})^2}{2Z^2(1 + \mathbf{B}^2)} + \frac{\gamma - 1}{\gamma} \frac{Z + DW}{W^2(1 + \mathbf{B}^2)} + \frac{\mathbf{B}^2}{2W^2(1 + \mathbf{B}^2)} \tag{2.75}$$

and

$$\mathcal{F}_2(Z,W) = 1 - \frac{1}{W^2} - \frac{1}{(Z+\mathbf{B}^2)^2}\left(\mathbf{S}^2 + 2\frac{(\mathbf{B}\cdot\mathbf{S})^2}{Z} + \mathbf{B}^2\left(\frac{\mathbf{B}\cdot\mathbf{S}}{Z}\right)^2\right) . \quad (2.76)$$

The combined zero of both functions – computed by a two dimensional Newton–Raphson iteration (function `mnewt` in Press et al., 1992) – yields values for Z and W which are then used to compute the primitives via

$$v^i = \frac{S^i + \frac{b^0}{W}B^i}{Z+\mathbf{B}^2} \quad \text{where} \quad \frac{b^0}{W} = \frac{\mathbf{B}\cdot\mathbf{S}}{Z} , \quad (2.77)$$

$$\rho = \frac{D}{W} \quad \text{and} \quad \varepsilon = \frac{1}{\gamma}\left(\frac{Z}{DW} - 1\right) . \quad (2.78)$$

The thermal pressure, p, can then be computed simply through (2.20).

The following checks are done to determine whether the recovery mechanism has provided the correct results:

- The relative difference between p and p_{alt} has to be smaller than 10^{-6}, where p_{alt} is computed according to the alternative formula

$$p_{alt} = Z + \mathbf{B}^2\left(1 - \frac{1}{2W}\right) - \frac{1}{2}\left(\frac{\mathbf{B}\cdot\mathbf{S}}{Z}\right)^2 - \tau - D . \quad (2.79)$$

- The velocities have to be smaller than the speed of light.
- Pressure and density have to be larger than predefined minimum values (far smaller than the characteristic values of the problem) in order to prevent vacuum zones. For example, the minimum value for the thermal pressure is set to 10^{-20} in a problem where the characteristic value is around 10^{-4}.

If any of these tests fails for a zone, the values are interpolated from those of the neighbouring zones. The recovery may fail when one of the terms in the total energy τ, Eq. (2.26), is much larger than the others, e.g. when the Lorentz factor is very large, while the pressure is small. Subtracting of that term from τ will lead to numerical errors.

2.2.9 Conservation of $\nabla \cdot \mathbf{B} = 0$

Although the constraint (2.16) is implicitly conserved by equations (2.24), their spatial discretisation and evolution by approximate solvers produces small errors which may grow and lead to unphysical results. Therefore, every MHD code has to include a method to keep $\nabla \cdot \mathbf{B} = 0$.

In principle there are two different approaches to ensure this (see Tóth, 2000, for an overview):

(i) *Divergence cleaning* which removes the unphysical monopole part of the magnetic field. The three most popular methods in this category are (a) the 8-wave-formulation by Powell (1994), (b) the projection of the numerical solution of $\mathbf{B}$ onto a subspace of zero divergence solutions (first suggested by Brackbill & Barnes, 1980, in the context of MHD), or (c) General Lagrange Multiplier methods like hyperbolic divergence cleaning (Munz et al., 2000). All of these methods require additions to the base numerical scheme, and have been developed for Newtonian MHD. While they have been used and tested for Newtonian MHD, their application to RMHD is not straightforward. Method (a) introduces a non-physical wave into the system, and thus violates the conservative properties of the system of equations. Method (b) requires a time consuming solution of a Poisson equation in every sub time step. In the hyperbolic divergence cleaning approach (c), the divergence errors are propagated off the grid by a wave equation (Dedner et al., 2002). However, we have not found an operative RMHD counterpart of this method, because the speed of light limits the speed of this wave, i.e. errors are not removed from the grid sufficiently fast, which is not the case in Newtonian MHD.

(ii) *Constrained transport* (Evans & Hawley, 1988) where one updates the magnetic field in a way that exactly conserves $\nabla \cdot \mathbf{B}$ in a specific discretisation. If the initial magnetic field has zero divergence in this discretisation, then this will be maintained to the accuracy of machine round off errors as long as the boundary conditions are compatible with the constraints. Most published applications of this approach use a staggered grid representation of the magnetic field, where the field components are defined at the cell interfaces and are interpolated to the zone centres in every time step in order to compute the fluxes. Tóth (2000) showed that it is possible to apply this idea without the need for a staggered grid. Staggered grid discretisations of the magnetic fields in combination with Godunov type, Riemann solver methods were published by Dai & Woodward (1998), Balsara & Spicer (1999) or Ryu et al. (1998).

In our code we use the method described by Ryu et al. (1998). We define two sets of magnetic field vectors (see Fig. 2.4):

1. the zone centred vector $\overline{\mathbf{B}}_{i,j}$ defined at coordinate (i, j) and
2. the *staggered* interface magnetic field $\mathbf{B}_{i,j}$ where $B^x_{i,j}$ is defined at $(i - 1/2, j)$ and $B^y_{i,j}$ at $(i, j - 1/2)$. Note that we have introduced a slight inconsistency in the notation in order to avoid formulae cluttered with indices.

The zone centred vector, $\overline{\mathbf{B}}$, is computed (temporarily) in the sweeps by simple interpolation from the staggered field components,

$$\overline{B}^x_{i,j} = \frac{1}{2}(B^x_{i,j} + B^x_{i+1,j}) \; . \tag{2.80}$$

It is required for setting the boundary conditions and source terms, and for the calculating the fluxes of the other variables. The field components are updated according to

$$(B^x_{i,j})^{n+1} = (B^x_{i,j})^n - \frac{\Delta t}{\Delta y}(\Omega_{i,j+1} - \Omega_{i,j}) \quad \text{and} \tag{2.81}$$

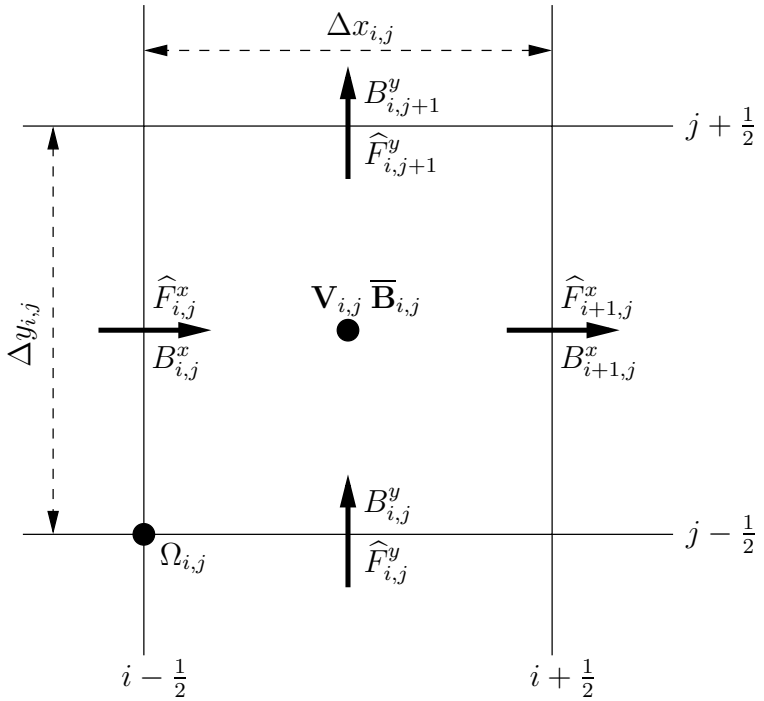

Figure 2.4: Illustration of the grid zone (i, j) and the positions of the staggered magnetic and electric fields, the fluxes and the zone centred variables.

$$(B^y_{i,j})^{n+1} = (B^y_{i,j})^n + \frac{\Delta t}{\Delta x}(\Omega_{i+1,j} - \Omega_{i,j}) \ , \tag{2.82}$$

where

$$\Omega_{i,j} = \frac{1}{4}(\widehat{F}^y(B^x)_{i-1,j} + \widehat{F}^y(B^x)_{i,j} + \widehat{F}^x(B^y)_{i,j-1} + \widehat{F}^x(B^y)_{i,j}) \tag{2.83}$$

is the flux interpolated electric field component in z-direction defined at the lower left corner of the zone (i, j). Here $\widehat{F}^y(B^x)_{i,j}$ is the numerical flux of B^x in y-direction across interface $i - 1/2, j$. It is easy to show that Eqs. (2.81)–(2.83) conserve the following discretisation of the divergence:

$$(\nabla \cdot \mathbf{B})_{i,j} \equiv \frac{B^x_{i+1,j} - B^x_{i,j}}{\Delta x_{i,j}} + \frac{B^y_{i,j+1} - B^y_{i,j}}{\Delta y_{i,j}} \ . \tag{2.84}$$

Figure 2.4 illustrates the locations of the different variables on the grid.

2.2.10 Boundary conditions

At the boundaries the computational grid is extended by four so-called *ghost zones*, which serve to enforce the boundary conditions for the primitive variables before the spatial interpolation is done, and before the Riemann solver is called. The number of ghost zones employed in this process depends on the order of the spatial interpolation algorithm (one for PLM, four for PPM).

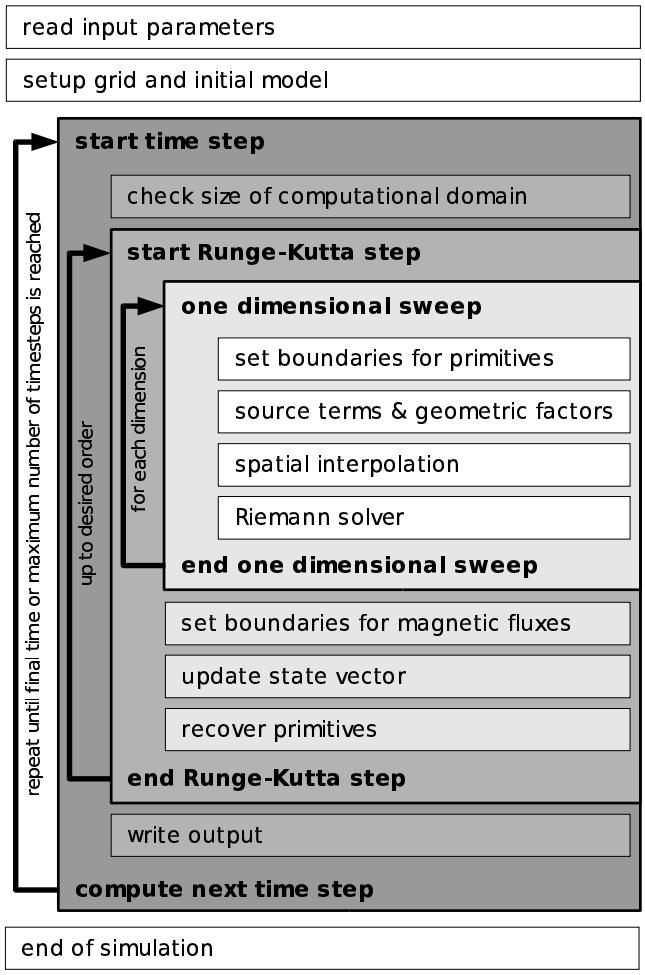

Figure 2.5: Flow diagram of the code.

A second boundary routine is called after the dimensional sweeps (see Fig. 2.5). It sets the boundary values for the magnetic field fluxes, Eq. (2.83). These only need to be enforced in the first ghost zone (see Eq. (2.83)), e.g. for computing $\Omega_{1,1}$ one has to set both $\widehat{F}^y(B^x)_{0,1}$ and $\widehat{F}^x(B^y)_{1,0}$. Usually we will copy the fluxes from a grid zone to its adjacent ghost zone, to enforce zero flux gradients.

2.2.11 Code structure

The code is based on the 3D relativistic hydrodynamics code *GENESIS* (Aloy et al., 1999*b*). While we have kept the general structure, most of the modules were substituted by their RMHD counterparts. The code is written in FORTRAN 77/90, and relies on the cpp preprocessor software to allow the program to perform on many different machine architectures. Preprocessing options also manage the parallelisation through *OpenMP*, and the selection of different algorithms for the different parts of the code.

A flow diagram of the code is displayed in Fig. 2.5. After the input parameters are read, the grid is constructed and all variables are initialised. The size of the

first time step, Δt^1, is given by the input parameters and is usually chosen to be very small. From the second time step onwards Δt is increased by 20% until it reaches the nominal value set by the CFL condition (2.58). In the beginning of each time step the code determines the active part of the computational domain, i.e. the number of grid zones involved in the simulation. For example, if there is a jet propagating into a grid filled with a uniform medium at rest, the equations are only evolved in that part of the grid where the fluid is affected. In this way one saves at least a factor of 2 of computational time when simulating jets. During each of the three Runge-Kutta sub time steps (Sec. 2.2.7) appropriate boundary conditions and geometric factors are provided, the numerical fluxes are computed along each spatial dimension, and the vector of source terms is calculated. Subsequently, the vector of conserved variables is updated, before the primitive variables are recovered by the method described in Sec. 2.2.8. After the third Runge-Kutta step the time step is complete, and the data output routines are called. Until the simulation reaches the final time given by the input parameters, the size of the next time step is computed, and the procedure starts from the beginning (Fig. 2.5).

All the results presented in this work were produced on IBM p690 Regatta systems at the Rechenzentrum Garching (RZG) of the Max-Planck-Gesellschaft.

2.3 Code validation

Before a numerical simulation code is used to solve a physical problem, it is necessary to validate its results by comparing them with known solutions of test problems. To this end one sets up a couple of Riemann problems in one or more dimensions, and checks whether the code can resolve all the waves that result from the breakup of the initial discontinuity. Ideal test cases would be those where an analytical solution to the problem is known. However, in RMHD there are not too many tests with known solutions, mainly because a closed solution for the general RMHD Riemann problem has not been found yet (Sec. 2.2.3). An alternative way of testing a RMHD code is to cross-check its test results against those obtained by other authors for the same test problems. With this aim in mind we have validated our code against the 1D test problems from Balsara (2001) which were also reproduced by Del Zanna et al. (2003). In 2D we have used the results of Komissarov (1999*a*).

2.3.1 1D test problems

Table 2.1 lists the parameters of the five Riemann problems described in Balsara (2001). The first four of these test were also considered by Del Zanna et al. (2003). Every test involves a discontinuity placed in the centre of a computational domain of 1600 grid zones. We ran each of the five problems twice: (1) using PLM interpolation, where we chose a threshold of $\beta = 4$ for the slope limiting (see Sec. 2.2.6), and (2) using PPM. A Courant number of $f_{\rm cfl} = 0.5$ was used in all of the test runs.

The first test, shown in Fig. 2.6, is the Newtonian MHD test of Brio & Wu (1988)

adapted to RMHD by van Putten (1993). It displays a fast rarefaction wave and a compound wave propagating to the left, a contact discontinuity, and a slow shock and a fast rarefaction wave propagating to the right. The higher order of the parabolic interpolation compared to the linear one is obvious from the difference in the number of points both methods need to resolve discontinuities. While the PLM scheme requires more than 20 points to resolve the contact discontinuity, PPM only needs 2 points compared to 10 points in Balsara. Our implementation of PPM also resolves both shock waves better than in Balsara (2001), i.e. the scheme can also handle the magnetically dominated right state of this particular Riemann problem, where the slow shock causes a problem for Balsara's method. Since both of our schemes display an overshooting of v^x at the rarefaction (Fig. 2.6c), we attribute this to our Riemann solver. The same overshooting is also visible in Del Zanna et al. (2003), whose results are a little less resolved than our PPM results.

The results of the blast wave test problems 2 and 3 are displayed in Figs. 2.7 and 2.8, respectively. Again, for both of our runs, the resulting waves are the same as in Balsara (2001). Test 2 is a blast wave with a moderate initial pressure difference. Its initial discontinuity breaks up into a fast rarefaction wave and a slow rarefaction propagating to the left, a contact discontinuity, and a slow shock and a fast shock propagating to the right (Fig. 2.7). All waves are well resolved using PPM, while PLM smears both shock waves across many zones. A maximum Lorentz factor of 1.36 is reached in both runs (Fig. 2.7e), which was also found by Balsara (2001). Test 3 is a blast wave with a strong initial pressure difference. It also develops two rarefaction waves propagating to the left, for example displayed in Figs. 2.8a and 2.8b, both captured equally well by PPM and PLM. However, the high density structure on the right is neither resolved in our runs nor in Balsara (2001). Nevertheless, using PLM and PPM, we obtain the same maximum Lorentz factor of about 3.4 (Fig. 2.8e) as Balsara (2001). This illustrates that despite the numerical viscosity of the algorithm we can obtain the physically correct overall structure for this test problem. The comparison with Del Zanna et al. (2003) shows that our PPM results are again

Table 2.1: Parameters for the 1D Riemann problems.

No.	initial state	ρ	p	v_x	v_y	v_z	B_y	B_z	B_x	γ	t_{final}
1	left	1.0	1.0	0.0	0.0	0.0	1.0	0.0	0.5	2.0	0.4
	right	0.125	0.1	0.0	0.0	0.0	-1.0	0.0	0.5	2.0	0.4
2	left	1.0	30.0	0.0	0.0	0.0	6.0	6.0	5.0	5/3	0.4
	right	1.0	1.0	0.0	0.0	0.0	0.7	0.7	5.0	5/3	0.4
3	left	1.0	1000.0	0.0	0.0	0.0	7.0	7.0	10.0	5/3	0.4
	right	1.0	0.1	0.0	0.0	0.0	0.7	0.7	10.0	5/3	0.4
4	left	1.0	0.1	0.999	0.0	0.0	7.0	7.0	10.0	5/3	0.4
	right	1.0	0.1	-0.999	0.0	0.0	-7.0	-7.0	10.0	5/3	0.4
5	left	1.08	0.95	0.4	0.3	0.2	0.3	0.3	2.0	5/3	0.55
	right	1.0	1.0	-0.45	-0.2	0.2	-0.7	0.5	2.0	5/3	0.55

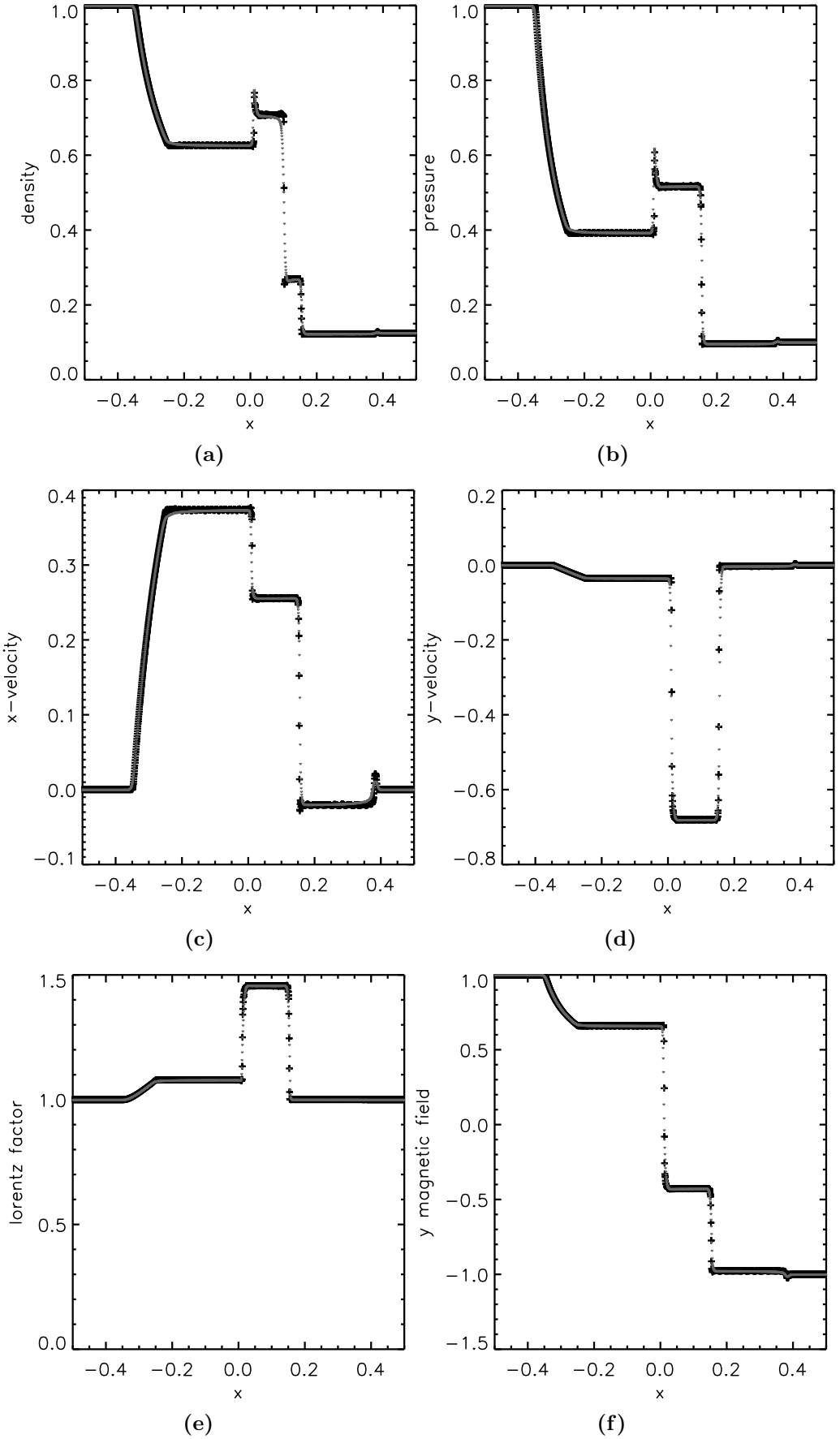

Figure 2.6: First 1D test problem. Relativistic analogue of the Brio & Wu (1988) test. The black crosses are the results with interpolation via PPM, the grey dots are computed with PLM.

slightly better resolved in test No. 2, while we get slightly worse results in the stronger blast wave test No. 3. This is visible from the height of the high density shell (Fig. 2.8a) which is 40% larger for PPM than for PLM, but approximately 2% smaller than in Del Zanna et al. (2003).

Figure 2.9 shows the results of test No. 4, a strong relativistic shock reflection test with two streams approaching each other at Lorentz factors of 22.366. This set up produces two fast and two slow shocks. Both PPM and PLM handle this test very well, but PLM requires more zones to resolve the slow shocks. At the initial collision point ($x = 0$) a certain amount of "wall heating" occurs, which is a numerical pathology of approximate Riemann solvers (e.g. Donat & Marquina, 1996). The problem arises because an excess of entropy is generated at the collision point at $t = 0$. This can diffuse numerically only slowly, because the fluid is at rest at that point. Higher order reconstruction schemes help to confine the problem to a small number of points initially but generate less diffusion. Hence the "hole" in the rest mass density (Fig. 2.9a) is larger with PPM (confined to only three grid zones with a relative error of about 10%) than with PLM (the "hole" is much more spread out with an error of 5%). In this test our PLM results are of similar quality than those of Balsara (2001) and Del Zanna et al. (2003), while our PPM implementation requires less zones to resolve the slow shocks.

Figure 2.10 shows the results of the fifth 1D test, a Riemann problem where all the velocities and magnetic field components are non zero initially. It shows a fast shock, an Alfvén wave, and a slow rarefaction propagating to the left, a contact discontinuity, and a slow shock, an Alfvén wave, and a fast shock propagating to the right. PLM and PPM perform similar on the fast shocks, while PPM is superior to PLM on all other structures. The PPM results are again better or comparable to those of Balsara (2001) apart from the spikes in v^z (Fig. 2.10e) and B^z (Fig. 2.10g) in the left Alfvén wave, where our method is off by about 3% compared to the values in Balsara (2001).

In summary, our code solves all of the test problems presented in Balsara (2001) correctly. As a rule of thumb, the PPM runs require less zones to resolve structures (in particular those of slowly moving waves) than both methods described in Balsara (2001) and Del Zanna et al. (2003), which are closer to our PLM results.

2.3.2 2D test problems

While the one-dimensional tests have shown that our code can resolve all the waves appearing in RMHD reasonably well, two-dimensional calculations introduce further complexities related with the constraint that the divergence of the magnetic field should remain zero (Sec. 2.2.9), which is trivially fulfilled for 1D tests.

Cylindrical explosion test

The cylindrical explosion test consists of a strong shock propagating into a magnetically dominated medium. Although there is no analytic solution to verify against,

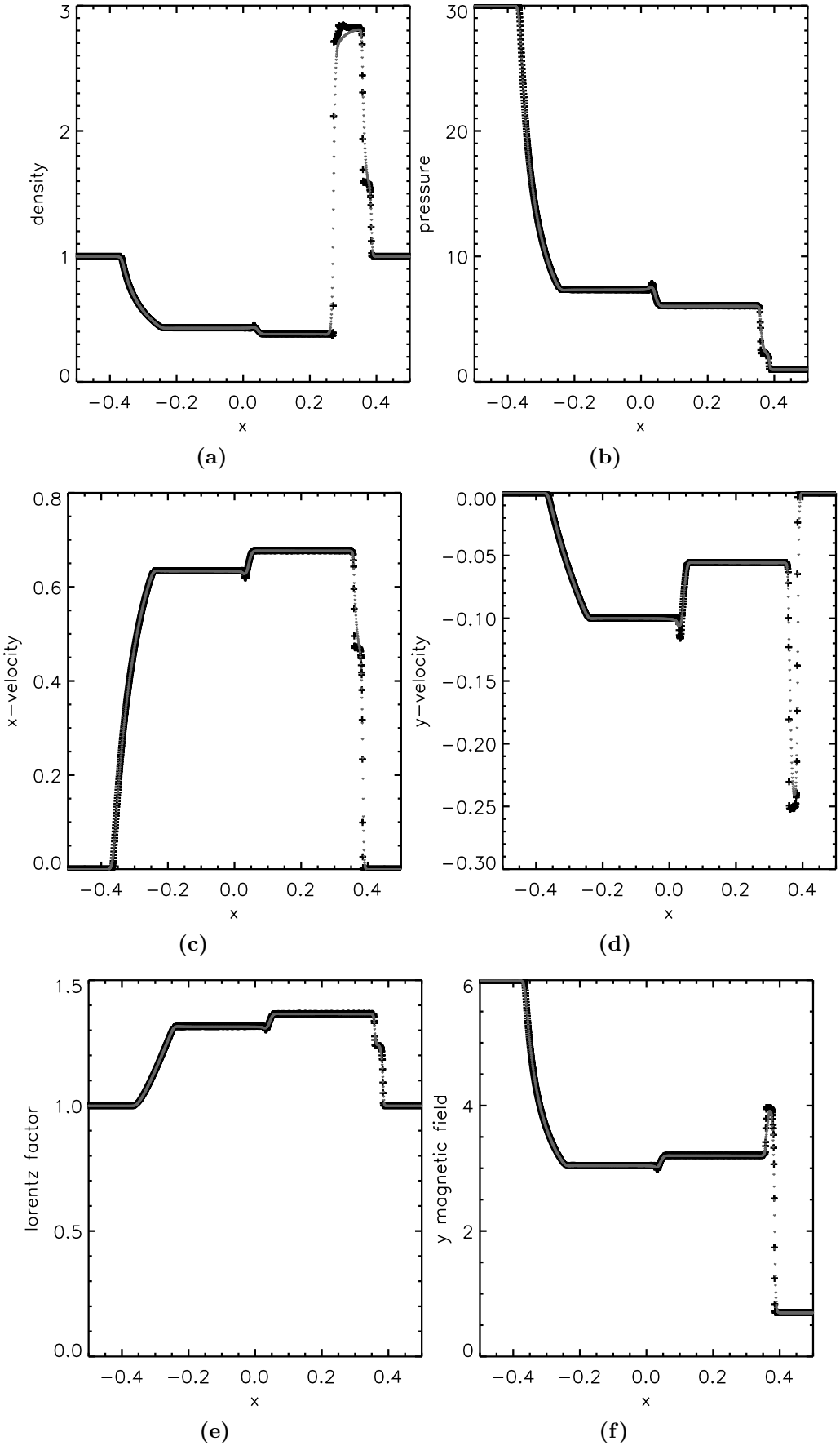

Figure 2.7: Second 1D test problem. Blast wave test with moderate initial pressure difference. The crosses are the results of the PPM run, the grey dots those of the PLM run.

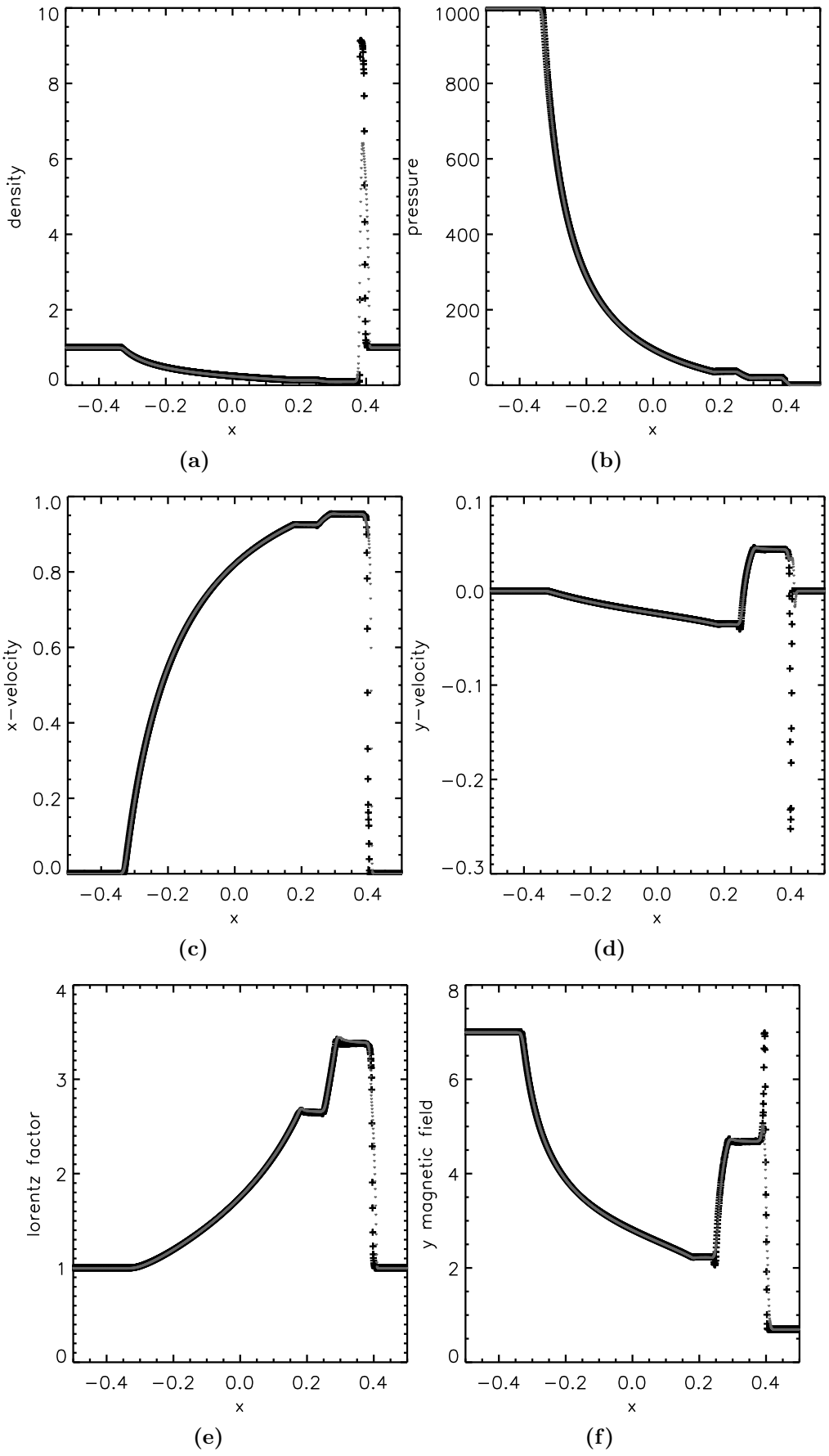

Figure 2.8: Third 1D test problem. Blast wave test with large initial pressure difference. The crosses are the results of the PPM run, the grey dots those of the PLM run.

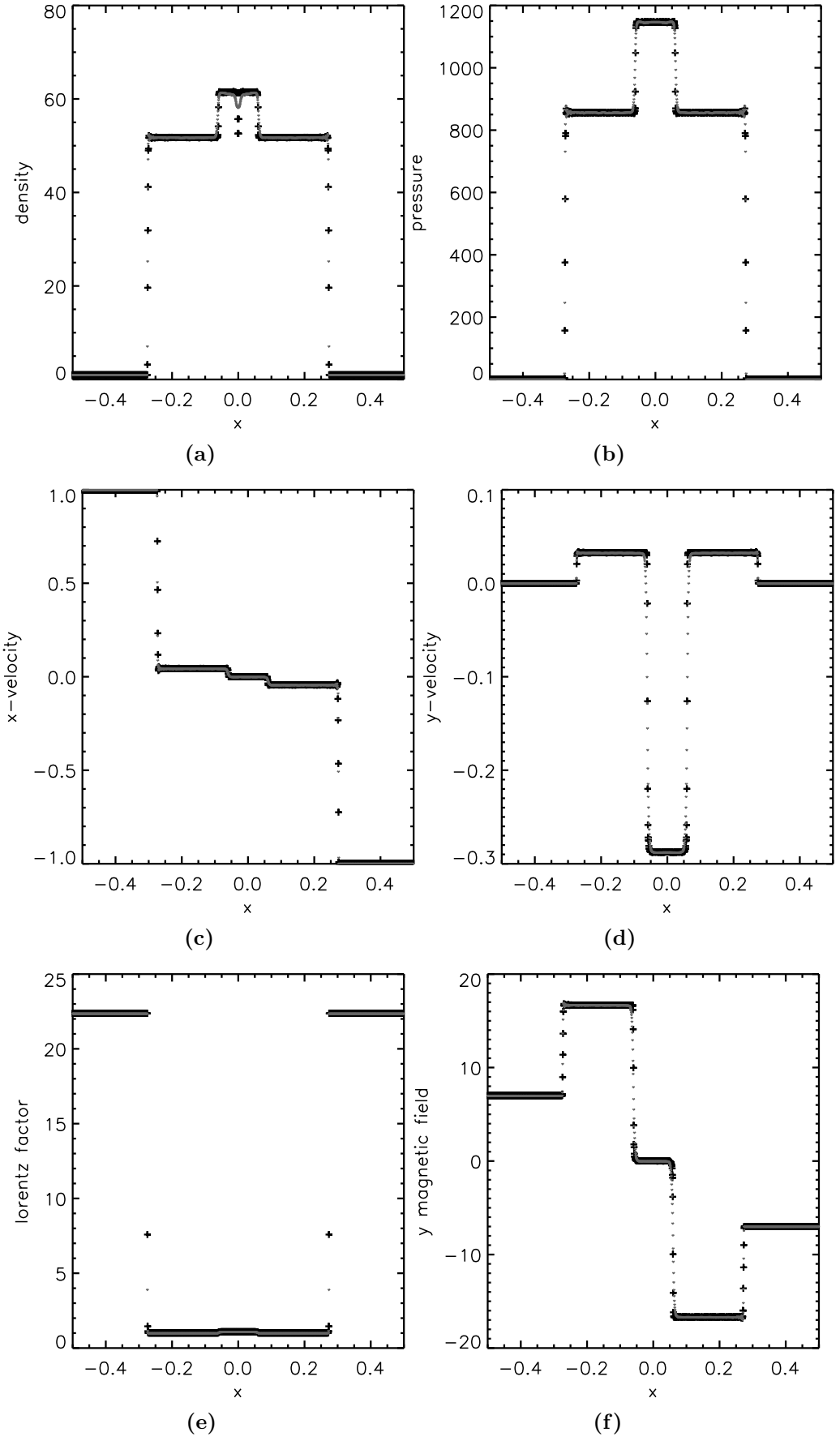

Figure 2.9: Fourth 1D test problem. Shock reflection test. The black crosses are the results of the PPM run, the grey dots those of the PLM run.

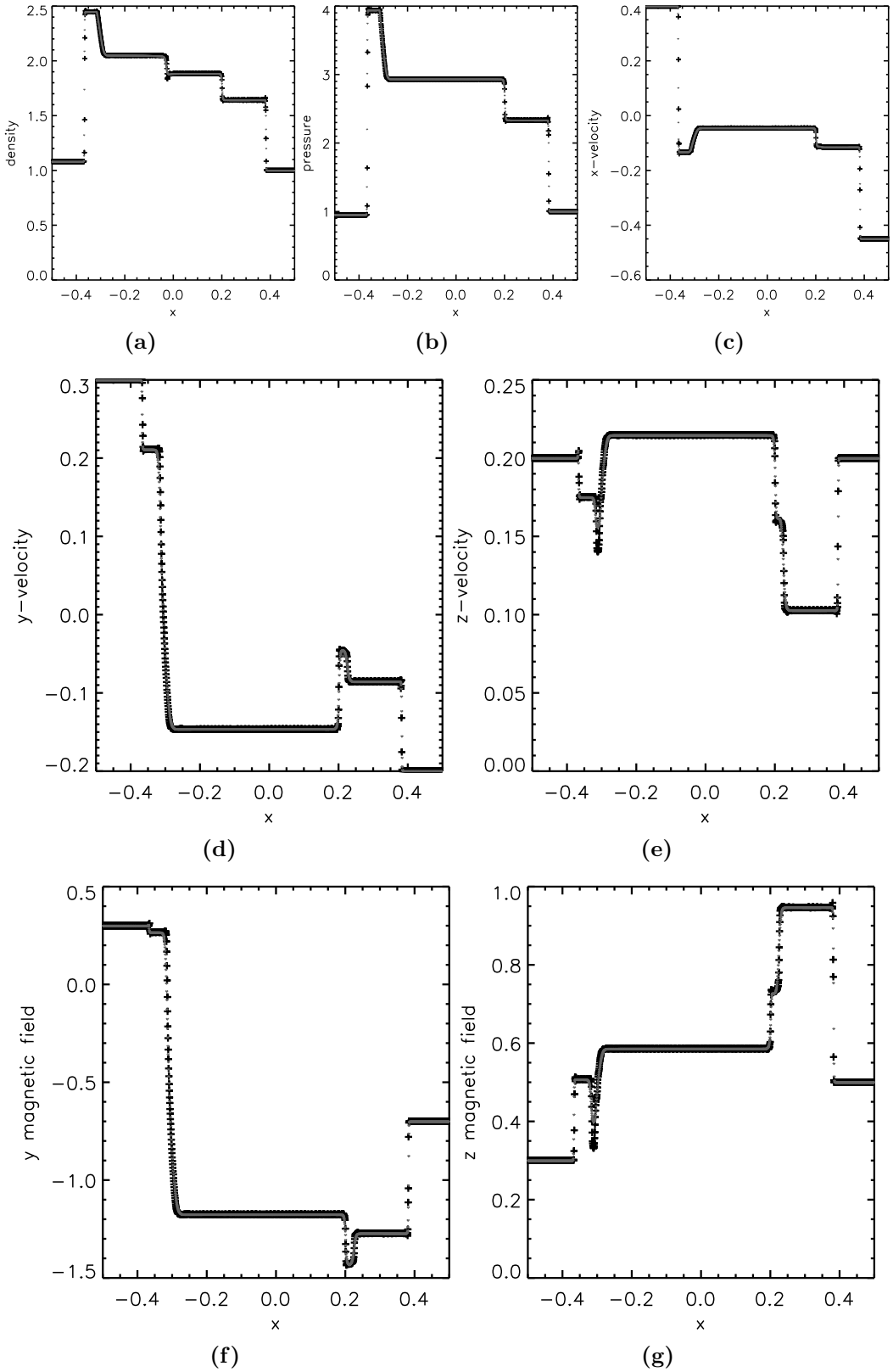

Figure 2.10: Fifth 1D test problem. A non-coplanar Riemann problem displaying all the MHD waves (see text for details). The black crosses are the results of the PPM run, the grey dots those of the PLM run.

this test still has very useful properties which make it a standard test of multidimensional numerical schemes for gas dynamics and MHD. For example, it encompasses all the degeneracies of the RMHD eigensystem (Sec. 2.1.5). Its simple setting makes it easy to spot bugs or weaknesses of a scheme which might not be seen so clearly in more complicated problems. Results for different cylindrical explosion problems in RMHD have been published (1) by Dubal (1991) indicating severe problems with his scheme, (2) by van Putten (1995) reaching only a maximum velocity of $v = 0.35$, (3) by Komissarov (1999*a*), and (4) by Del Zanna et al. (2003).

We have chosen a setup very similar to that in Komissarov (1999*a*): a cylinder of high pressure and density is located in the centre of a square Cartesian grid, which initially contains a uniform, strong magnetic field. The grid has 200 by 200 zones spanning 12 by 12 units of distance. In the centre of the grid there is a circle of radius 0.8 where $\rho = 10^{-2}$ and $p = 1$. Between a radius of 0.8 and 1.0 the values smoothly decrease to those of the homogeneous ambient medium ($\rho = 10^{-4}$ and $p = 5 \times 10^{-4}$). Initially, the magnetic field is $B^x = 0.1$, and the velocity is zero everywhere. The simulations were carried out on an IBM Power4 processor and required about 300 seconds of CPU time.

Figures 2.11 and 2.12 show the results of this test at time $t = 4.0$ using PLM and PPM, respectively. One recognises an outer fast shock, which is almost circular, because the fast magnetosonic speed varies little across the grid. The innermost region is also circular and bounded by a reverse fast shock. The expansion of this region is almost circular, because the Lorentz force is small there. In between these two shocks there are two more discontinuities, bounded on the outside by the compressed magnetic field (see the field lines in Figs. 2.11d and 2.12d). The constrained transport works in both cases as demonstrated by the plots of $\nabla \cdot \mathbf{B}$ (Figs. 2.11b and 2.12b).

While the overall picture is very much the same in both cases, there are some obvious differences. The maxima and minima of both magnetic field components are slightly different in the two methods, see panels (a) and (b) in Figs. 2.11 and 2.12. In addition, the PPM results show oscillations on a 5% level. These are a consequence of the staggered grid approach keeping the code divergence free (see Sec. 2.2.9), because the linear interpolation (2.80) of the staggered field components is of different order than the spatial PPM reconstruction described in Sec. 2.2.6. Increasing the resolution removes this problem. Figure 2.13 shows plots of the thermal pressure along $x = 0$ for two different resolutions: 200 by 200 zones (upper panel) and 800 by 800 zones (lower panel). While PPM (black crosses) requires less points than PLM (grey dots) in discontinuities in the higher resolution run, there is no such trend in the lower resolution run. At both resolutions PPM produces small oscillations.

Toroidal field jets

Up to now there exists only one publication where a RMHD code is applied to the simulation of strongly relativistic magnetised jets. Komissarov (1999*b*) presents two models of axisymmetric RMHD jets injected into a non-magnetised, homogeneous

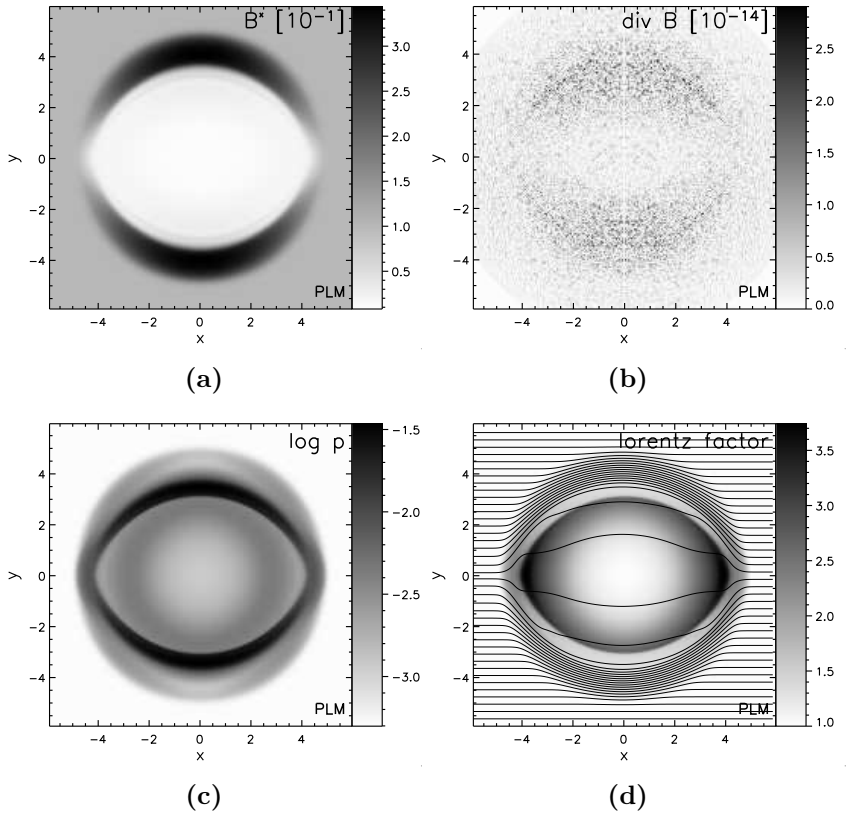

Figure 2.11: Cylindrical explosion test with PLM reconstruction.

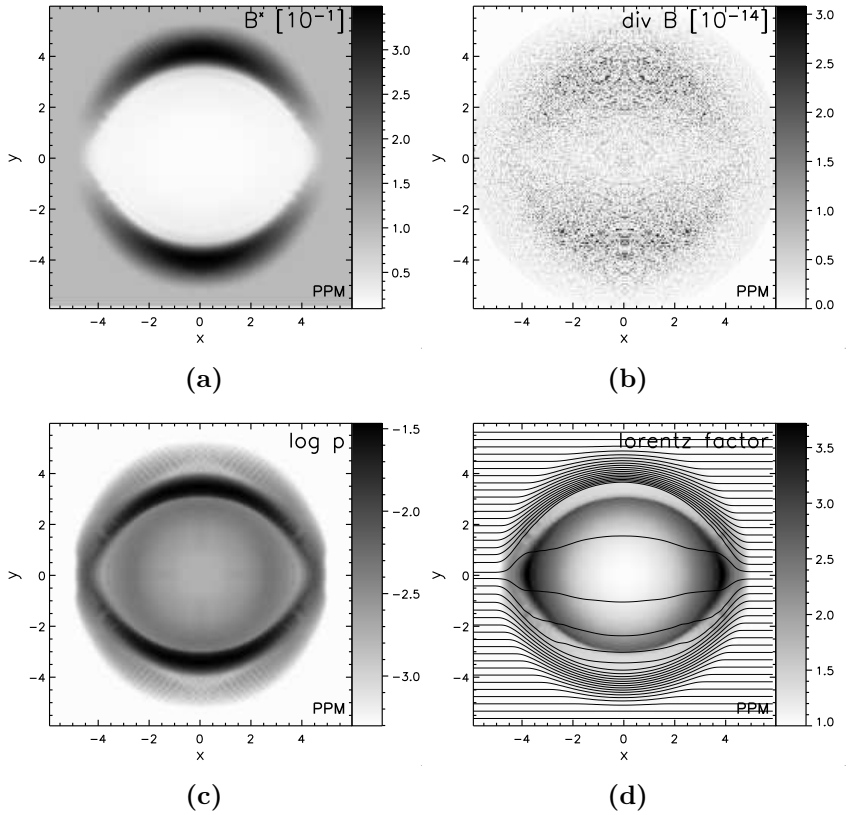

Figure 2.12: Cylindrical explosion test with PPM reconstruction.

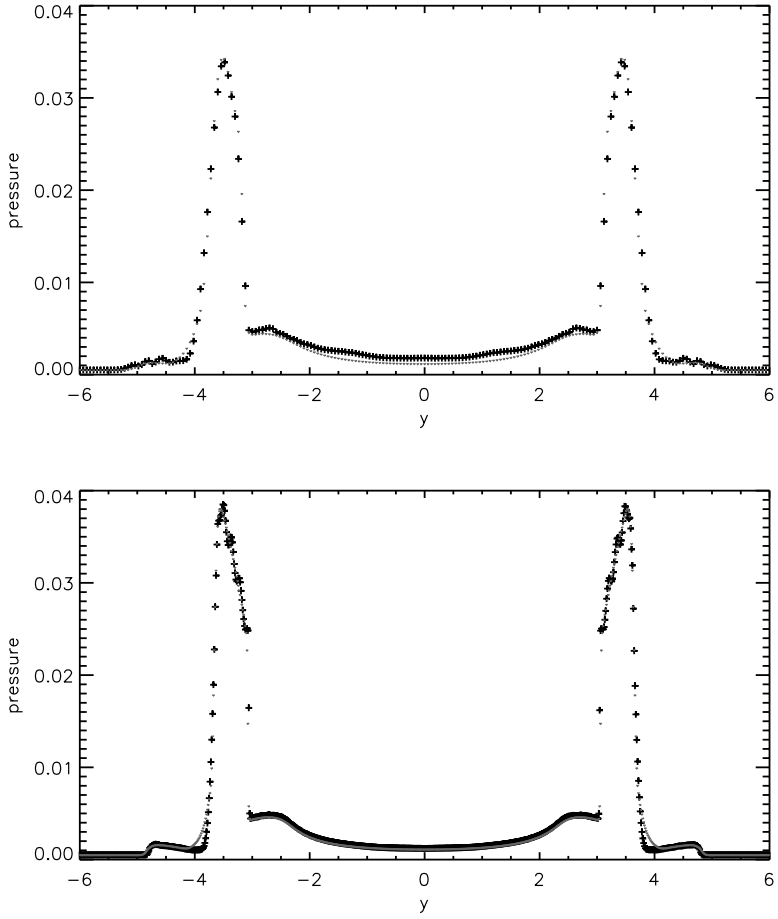

Figure 2.13: Plot along $x = 0$ of the thermal pressure of the cylindrical explosion test. The top panel shows the results for the original grid of 200 by 200 zones, while the bottom panel is the result of the same test on a grid of 800 by 800 zones. The black crosses are the PPM results, the grey dots are the PLM results.

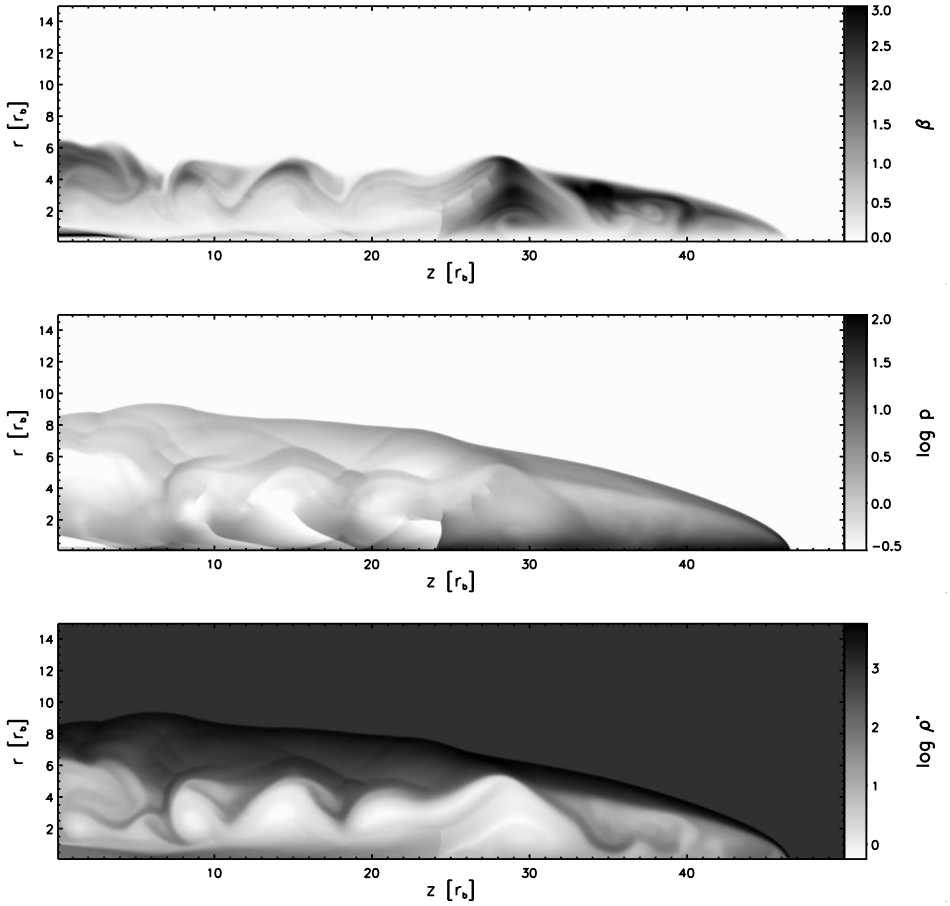

Figure 2.14: Jet model A from Komissarov (1999*b*) at time 110. For a direct comparison we have the same variables, β (top), pressure (middle) and the relativistic density $\rho^* = \rho W^2$ (bottom) at the same time $t = 110$ as in Komissarov (1999*b*).

ambient medium. A toroidal field component is added to the inflowing jet plasma. We have repeated both calculations described there. For the details of the setup of the simulations we refer the reader to Komissarov (1999*b*).

Figure 2.14 shows the results of jet model A at evolutionary time 110 computed with the PLM spatial reconstruction. Directly comparing these plots to Fig. 3 in Komissarov (1999*b*) we can identify the same number and position of shocks on the jet axis. In addition the length and position of the *nose cone*, the high pressure region that makes up the tip of the jet, only differ by a few percent. Differences in the cocoon structure are to be expected given the different numerical schemes used to obtain both results. For the low Poynting flux model, model B, we find a similar good agreement with the results of Komissarov (1999*b*).

2.3.3 Convergence Tests

The tests discussed in the previous subsections are mainly devoted to demonstrate the robustness of the code when simulating relativistic flows and shocks. They also show that PPM is of higher accuracy than PLM, which should be third and second

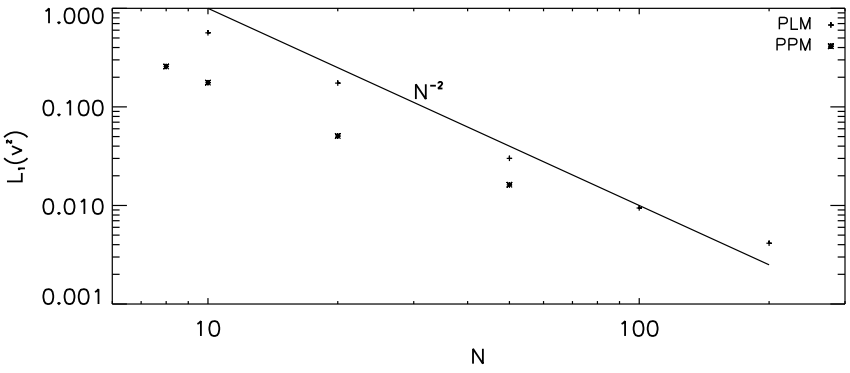

Figure 2.15: Convergence test for the 2D Alfvén wave problem. Not that the convergence is of slightly lower order in PPM, the absolute error in PPM is smaller than in PLM.

order accurate, respectively, for flows without discontinuities. This, however, is only valid when the staggered magnetic field components are zero. Otherwise, the second order accurate interpolation of the staggered field components, Eq. (2.80), reduces the order of the method. This has to be studied in an appropriate test simulation. To this end we computed the propagation of relativistic circularly polarised Alfvén waves as described in Del Zanna et al. (2003).

The initial conditions for the test are the following: in a generic Cartesian reference frame (ξ, η, χ) we set $\rho = 1$, $p = 0.1$, $B^\xi = B_0 = \sqrt{2}$, $v^\xi = 0$,$B^\eta = -0.01\cos(2\pi\xi)$, and $B^\chi = -0.01\sin(2\pi\xi)$. In the limit of small wave amplitudes, the total magnetic field strength is conserved, the Alfvén speed is $B_0/\sqrt{\rho h^*}$, and the relation between velocity and magnetic field fluctuations is such that $v^\eta = B^\eta/\sqrt{\rho h^*}$ and $v^\chi = B^\chi/\sqrt{\rho h^*}$. On a 2D grid we consider a propagation in $x = y$ direction such that $(\xi, \eta, \chi) = ((x+y)/\sqrt{2}, (-x+y)/\sqrt{2}, z)$. We have assumed periodic boundary conditions, and a grid size of $[0, \sqrt{2}] \times [0, \sqrt{2}]$ in order to satisfy these conditions.

The convergence can be tested by measuring the relative error of the numerical solution of v^z after one period, T. As in Del Zanna et al. (2003), we evaluate the L_1 norm of v^z,

$$L_1(v^z) = \frac{\sum_{i,j} \left| v^z_{i,j}(t=T) - v^z_{i,j}(t=0) \right|}{\sum_{i,j} |v^z_{i,j}(t=0)|} \,. \tag{2.85}$$

The errors are plotted in Fig. 2.15 for both PPM and PLM as functions of the number of grid points $N = N^x = N^y$. As expected, the staggered grid formulation of the magnetic field reduces PPM from third to second order. The reduced second order accuracy of the PPM/staggered field implementation leads to a convergence rate which is slightly smaller than the second order convergence rate of PLM. The absolute errors, however, remain smaller in PPM. In a second test (not shown here) with the staggered field components absent, i.e. $B^x = B^y = 0$, we have verified that PPM is indeed third order as expected from the 1D test results presented in Sec. 2.3.1.

3 Parameter Study

3.1 Introduction to jet simulations

The numerical grid

All jet simulations in this work were performed on a 2D equidistant grid in cylindrical coordinates, (r, z) assuming axisymmetry. Thus every grid zone (i, j) at position (r_i, z_j) has a volume of $2\pi r_i \Delta r \Delta z$. In fact, the simulations themselves are *2.5-dimensional* as we evolve all three spatial components using Eqs. (2.30)–(2.37), and thus include toroidal magnetic fields and motion.

The simulated jets are produced by injecting beam matter into the grid through a nozzle at $z = 0$ of width $0 < r < 1$ (Fig. 3.1). This also fixes the basic length scale used for measuring distances which is the *beam radius*, $r_b \equiv 1$. Outside the nozzle, i.e. for $1 < r < r_{\max}$ and $z = 0$ we impose special reflecting boundary conditions by implying that the axial and toroidal velocity and field components are mirrored. This is justified by the presence of a twin counter jet in real radio galaxies and eliminates the Lorentz force in the equatorial plane. The assumed axisymmetry also implies reflecting boundary conditions on the symmetry axis at $r = 0$ where the radial and toroidal velocity and magnetic field components are mirrored, i.e. they are zero at zero radius. At the two outer edges of the grid, i.e. $r = r_{\max}$ and $z = z_{\max}$ we impose zero gradient boundary conditions. Material is allowed to freely leave the grid there.

We assume that the computational domain is initially filled with a uniform medium of density $\rho = 1$ at rest having the same thermal pressure and adiabatic index as the jet. The initial magnetic field configuration depends on the type of simulation.

Jet parametrisation

Every jet simulation is fully specified by setting a few independent parameters:

- the flow speed of the beam, v_b, where the subscript b stands for beam;
- the ratio of the rest mass densities of the beam fluid and the external medium, η;
- the adiabatic index, γ, used in the equation of state (2.20);

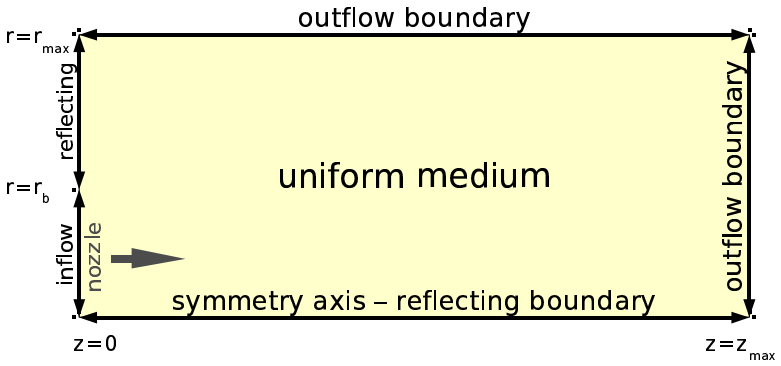

Figure 3.1: Diagram of a 2D cylindrical grid. The sizes of the different boundaries are not proportional.

- the classical beam Mach number $M_b = v_b/c_s$ (which controls the thermodynamic relativistic effects of the model) or its relativistic analogue,the proper Mach number, $\mathcal{M}_b = M_b W_b/W_s$, where $W_s \equiv (1-c_s^2)^{-1/2}$ is the Lorentz factor associated with the local sound speed (Königl, 1980);

- the magnetisation parameter, β (see Eq. (2.17)), both of the beam fluid and the external medium.

Another parameter, σ, defined by Eq. (2.18), roughly measures the ratio of Poynting flux and mass flux. It will prove useful when discussing the simulations. It is not independent of the others, therefore not needed to specify a jet model.

Magnetisation parameter

When simulating a jet with a non-uniform magnetic field, the magnetisation parameter of the beam is given by the average value, $\overline{\beta}$, across the beam. In our simulations of jets with toroidal magnetic fields presented below we have assumed that the beam has a core of uniform electric current with radius r_m—called magnetisation radius—and a shell without any current. Then the (toroidal) magnetic field in the beam, $b_b^\phi = B^\phi \cdot W$, is the following:

$$b_b^\phi = \begin{cases} b_0 \frac{r}{r_m} & \text{if } r < r_m \ , \\ b_0 \frac{r_m}{r} & \text{if } r \geq r_m \ , \\ 0 & \text{if } r > r_b \ . \end{cases} \tag{3.1}$$

Averaging (3.1) over a beam cross section and dividing by the uniform thermal beam pressure, p_b, yields

$$\overline{\beta} = \frac{b_0^2 r_m^2 (0.25 - \ln r_m)}{p_b} \ . \tag{3.2}$$

From p_b, $\overline{\beta}$ and r_m one can obtain b_0 through (3.2). In the simulations with a purely poloidal magnetic field we have chosen a simpler initial setup: the grid is initially

filled with a uniform, axial magnetic field, B^z, which according to the definition of the parameter β (2.17) is given by

$$|b|^2 = \left(\frac{B^z}{W}\right)^2 + (v^z B^z)^2 = 2\frac{\beta}{p_b} \quad \Rightarrow \quad B^z = \sqrt{2\frac{\beta}{p_b}}\,. \tag{3.3}$$

Through the nozzle the same field is injected with the flow.

Analysis tools

In Chapter 1 we have already described the morphological features of jets obtained from numerical simulations (see Sec. 1.4 and Fig. 1.4). We will point out these features by presenting snapshot images of the rest mass density, the thermal pressure, the magnetic fields, the Lorentz factor and other quantities. For further analysis of the results we introduce a number of global quantities:

- the *head position* of the jet is the z–coordinate of the leading bow shock and, therefore, the length of the cavity, l_c;
- the *cylindrical aspect ratio*, $A_c \equiv l_c/r_c$, is the aspect ratio of a cylinder which has the same volume and length, l_c, as the cavity, i.e. $r_c = \sqrt{V_c/(\pi l_c)}$;
- the *cocoon mass*, M_{cc} (see below for a working definition of cocoon);
- *cavity averages* which are number averages in order not give to much weight to the large zones at larger radii. We will use cavity average of the thermal pressure and the β parameter;
- the *hot spot pressure* which is the pressure averaged over a small number of zones downstream of the contact discontinuity at the termination of the beam (defined via the tracer variable, see next paragraph).

Local quantities that will be used are

- the *beam averages*, quantities averaged over the first 10 zones in radial direction and plotted along the axis; and
- *magnetic field lines*.

For tracing the beam material we evolve another variable in our code that represents the beam mass fraction, $f \equiv \frac{\rho_b}{\rho}$. This tracer variable is set to $f = 1$ for the material injected through the nozzle and to $f = 0$ for the ambient medium. In the following, the beam mass fraction will be used to divide the different parts of the jet: zones where $f \geq 0.9$ belong to the beam, and zones where $0.1 < f < 0.9$ belong to the cocoon. The same scheme was used by Scheck et al. (2002) which simplifies a comparison with their results (Cha. 4). The cavity is defined as all the region where $f > 0$. Note that cavity and cocoon are different things according to this

definition, whereas in the literature the terms cocoon and cavity are sometimes used interchangeably.

A one dimensional estimate for the head advance speed of a non-magnetised, relativistic jet can be obtained by equating the momentum flux of the beam and the ambient gas in the frame of the working surface (Martí et al., 1997):

$$v^{1d} = \frac{\sqrt{\eta_R^*}}{1+\sqrt{\eta_R^*}} v_b \ , \tag{3.4}$$

where $\eta_R^* = \eta_R W_b^2$. $\eta_R = \frac{\rho_b h_b}{\rho_a h_a}$ is the ratio of the enthalpies of the beam and the ambient medium (subscript a stands for ambient medium). Even though this does not hold for magnetised jets, it will, as below, proven to be a very good estimate in most of the simulations.

The evolution of 2D jets can be divided into two phases (Scheck et al., 2002): (1) a 1D phase where the velocity is constant and approximated by (3.4); and (2) a 2D phase where 2D effects become important and the jet decelerates. The 2D phase starts when the first major vortex shedding occurs at the terminal Mach disk.

3.2 Model parameters

We have selected three of the jet models of Martí et al. (1997) to study the effects of different magnetic field configurations on the dynamics and morphology of relativistic jets. All of these jets are light, supersonic and gas pressure matched with the ambient medium. In the toroidal field models the magnetisation radius was chosen to be $r_m = 0.6$, and the magnetic field (3.1) is injected with the beam into a uniform, non-magnetised medium. In the poloidal field runs, the whole grid is filled with a uniform, purely axial magnetic field of the same strength as that injected with the beam according to (3.3), otherwise the external medium is the same as in the toroidal field models. The simulations were performed on a grid of 420 by 2000 zones covering a domain of 10.5 by 50 beam radii, i.e. the resolution is $40/r_b$. The purely hydrodynamic and toroidal field models were carried out employing PLM spatial interpolation while the poloidal field runs were done with PPM interpolation. All models were evolved until the head of the jet reached the edge of the computational domain in the z-direction.

Table 3.1 lists the parameters of all models. We use the same model names as Martí et al. (1997) extended by suffixes describing the magnetic field strength, for example, the toroidal field model of the C2 series with an average magnetisation of 1 (i.e. the equipartition model) is called C2-1, and the corresponding poloidal field model is called C2-pol-1. All models have $\sigma < 1$, i.e. they have a low Poynting flux. The models of the B1 and the C2 series only differ in the adiabatic index, γ, and those of the C1 and the C2 series only differ in the velocity of the beam, v_b.

Note that we use different boundary conditions (reflecting outside the nozzle, see previous section) compared to Martí et al. (1997), who imposed zero gradients outside the jet nozzle. Therefore, the results of our purely hydrodynamic reference simulations are slightly different from their results.

All the simulations presented in this section were carried out on the IBM p690 Regatta computer of the Max-Planck-Society's Rechenzentrum Garching. They required between 8 and 30 hours on a shared memory node with 32 Power4 1300 MHz processors.

3.3 C2 series

C2-0 to C2-10/3: purely hydrodynamic and toroidal field models

Figures 3.2 to 3.4 show images of the rest mass density, the thermal pressure and the Lorentz factor of the purely hydrodynamic model C2-0, and the toroidal field models C2-1/20, C2-1 and C2-10/3 (from top to bottom). Apart from differences in details, one morphological feature is especially noticeable: with growing toroidal field strength, the supersonic part of the beam ends further and further away from the leading edge of the bow shock (see the $f = 0.9$ tracer contours in Fig. 3.2 or the Lorentz factor images in Fig. 3.4). The high density and pressure structure between the termination of the supersonic beam and the head of the jet is called *nose cone* (Clarke et al., 1986) or *plug* (Lind et al., 1989). It is made up of entrained ambient material. Both the density and the pressure in the nose cone are very high, and show turbulent structures. Moreover, the pressure in the nose cone is relatively smooth and particularly high on the axis (due to magnetic confinement; see the equipartition contours in Fig. 3.3). The nose cone makes the head of the jet appear narrower for higher values of $\overline{\beta}$.

Concentrating on the first recollimation shock on the axis, one recognises, that it

Table 3.1: Parameters of the different models.

Model	field config.	η	γ	v_b	M_b	$\mathcal{M}_b$	$\overline{\beta}$	σ
C2-0	none	0.01	5/3	0.99	6.0	41.95	0	0
C2-1/20	toroidal	0.01	5/3	0.99	6.0	41.95	1/20	0.0017
C2-1/2	toroidal	0.01	5/3	0.99	6.0	41.95	1/2	0.0171
C2-1	toroidal	0.01	5/3	0.99	6.0	41.95	1	0.0341
C2-10/3	toroidal	0.01	5/3	0.99	6.0	41.95	10/3	0.1135
C2-pol-1	poloidal	0.01	5/3	0.99	6.0	41.95	1	0.0341
B1-0	none	0.01	4/3	0.99	6.0	41.95	0	0
B1-1/20	toroidal	0.01	4/3	0.99	6.0	41.95	1/20	0.0022
B1-1/2	toroidal	0.01	4/3	0.99	6.0	41.95	1/2	0.0222
B1-1	toroidal	0.01	4/3	0.99	6.0	41.95	1	0.0445
B1-10/3	toroidal	0.01	4/3	0.99	6.0	41.95	10/3	0.1482
B1-pol-1	poloidal	0.01	4/3	0.99	6.0	41.95	1	0.0445
C1-0	none	0.01	5/3	0.9	6.0	13.61	0	0
C1-1	toroidal	0.01	5/3	0.9	6.0	13.61	1	0.0279
C1-10/3	toroidal	0.01	5/3	0.9	6.0	13.61	10/3	0.0931
C1-pol-1	poloidal	0.01	5/3	0.9	6.0	13.61	1	0.0279

is located closer to the nozzle and gets stronger (i.e. it reaches higher values of thermal pressure) with increasing magnetic field strength, and has a more extended post-shock state. In C2-0 the post-shock state extends from $z = 12$ to $z = 18$, in C2-1/20 from $z = 8$ to $z = 17$; in C2-1 from $z = 6$ to $z = 14$; and finally, in C2-10/3 from $z = 5$ to $z = 14$. In fact, in C2-10/3, it is impossible to distinguish between the end of the post-shock state of the first cross shock and the start of the second cross shock, therefore they have been counted as one. In general, the cross shocks on the axis are stronger in the more magnetised models, while their number seems to be independent of the degree of the magnetic field strength.

How the beam material reacts to the toroidal magnetic field can be inferred from the tracer contour in Fig. 3.2. In C2-1/20 the beam material fills up the low density bubble at the head of the jet. With increasing toroidal fields this bubble is shifted away from the head and becomes larger in size. In C2-10/3 it roughly stretches from $z = 20$ up to $z = 35$, and has become confined by a shell of highly magnetised material (see the equipartition contours in Fig. 3.3). The position of the bubble nearer to the nozzle follows from the fraction of the length of the jet that is occupied by the nose cone, which grows with increasing magnetic field strength. The Mach disk and terminal shock of the beam reside in the middle of the bubble. The beam flow stops at the Mach disk and the matter has to flow around it to reach the head of the jet (Fig. 3.4). In the case of model C2-1, the flow around the Mach disk reaches relativistic speeds with Lorentz factors of 3 or more. The beam itself ends at the Mach disk, i.e. it does not penetrate into the nose cone. But even if the beam is not stopped before the head of the jet, already the small degree of magnetisation of model C2-1/20 leads to a decrease of the bulk Lorentz factor in the beam well before it reaches the head of the jet. In general, the beam Lorentz factor will decrease with an increasing magnetisation of the beam.

Figure 3.5 displays the magnetisation and magnetic field distribution of models C2-1 and C2-10/3. In both models the magnetisation β decreases drastically in the first cross shock due to an increase in thermal pressure. It remains low inside the beam until this reaches the terminal shock. β increases again downstream of the shock, and becomes even larger where shocked plasma flows away radially from the jet axis. The pinching force provided by the toroidal field in this region suppresses further sideways expansion of the jet and pushes a large fraction of the plasma into the nose cone. In model C2-10/3 this pinching is strongest at $z = 38$ (see the bottom panel of Fig. 3.4). The nose cone contains primarily highly magnetised plasma which leads to a strong pinching force confining the flow close to the axis. The high magnetisation of the material around the bubble is interesting. The magnetic field accumulates at the inside of the high density shell of the jet, where the thermal pressure is low, leading to a large value of β. This magnetic shell may influence the emission properties of the jet, because it may appear very bright, in contradiction to observations of astrophysical sources. The magnetic field itself is largest in the beam and in the nose cone (lower two panels in Fig. 3.5).

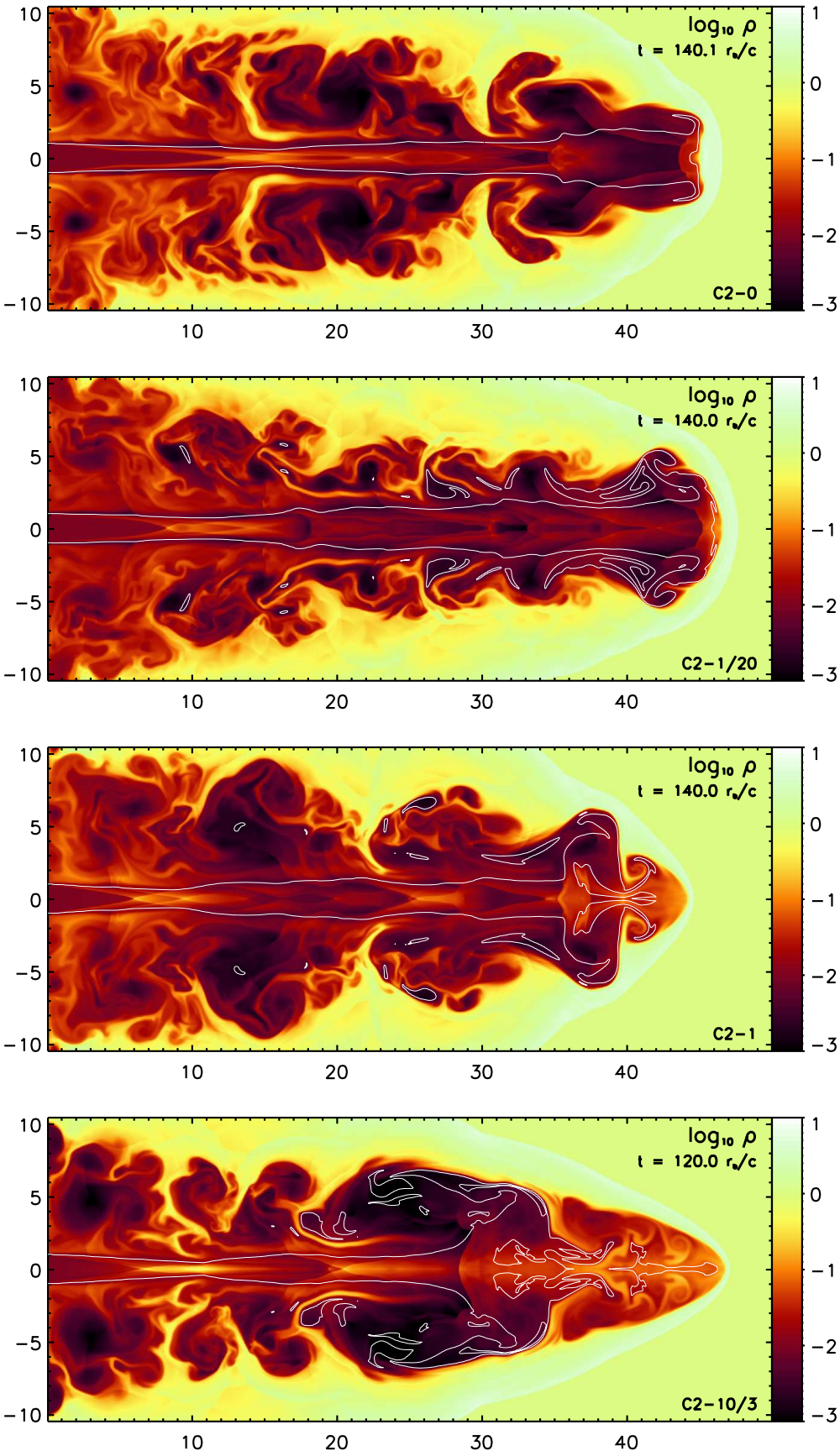

Figure 3.2: Snapshots of the logarithm of the rest mass density of models C2-0, C2-1/20, C2-1 and C2-10/3 (from top to bottom). The white lines are contours of the tracer variable $f = 0.9$

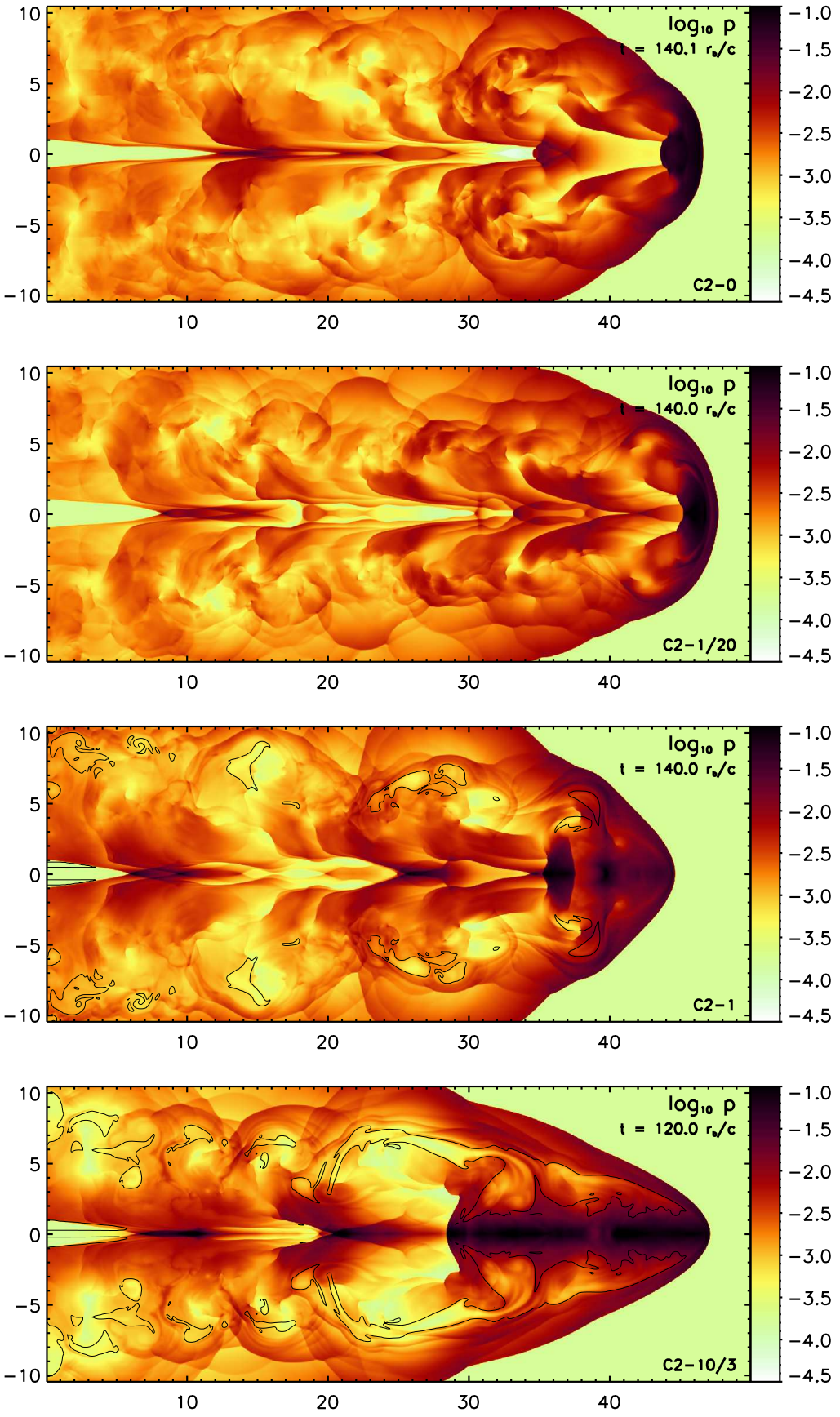

Figure 3.3: Snapshots of the logarithm of the thermal pressure of models C2-0, C2-1/20, C2-1 and C2-10/3 (from top to bottom). The black contour is the line of equipartition where $\beta = 1$.

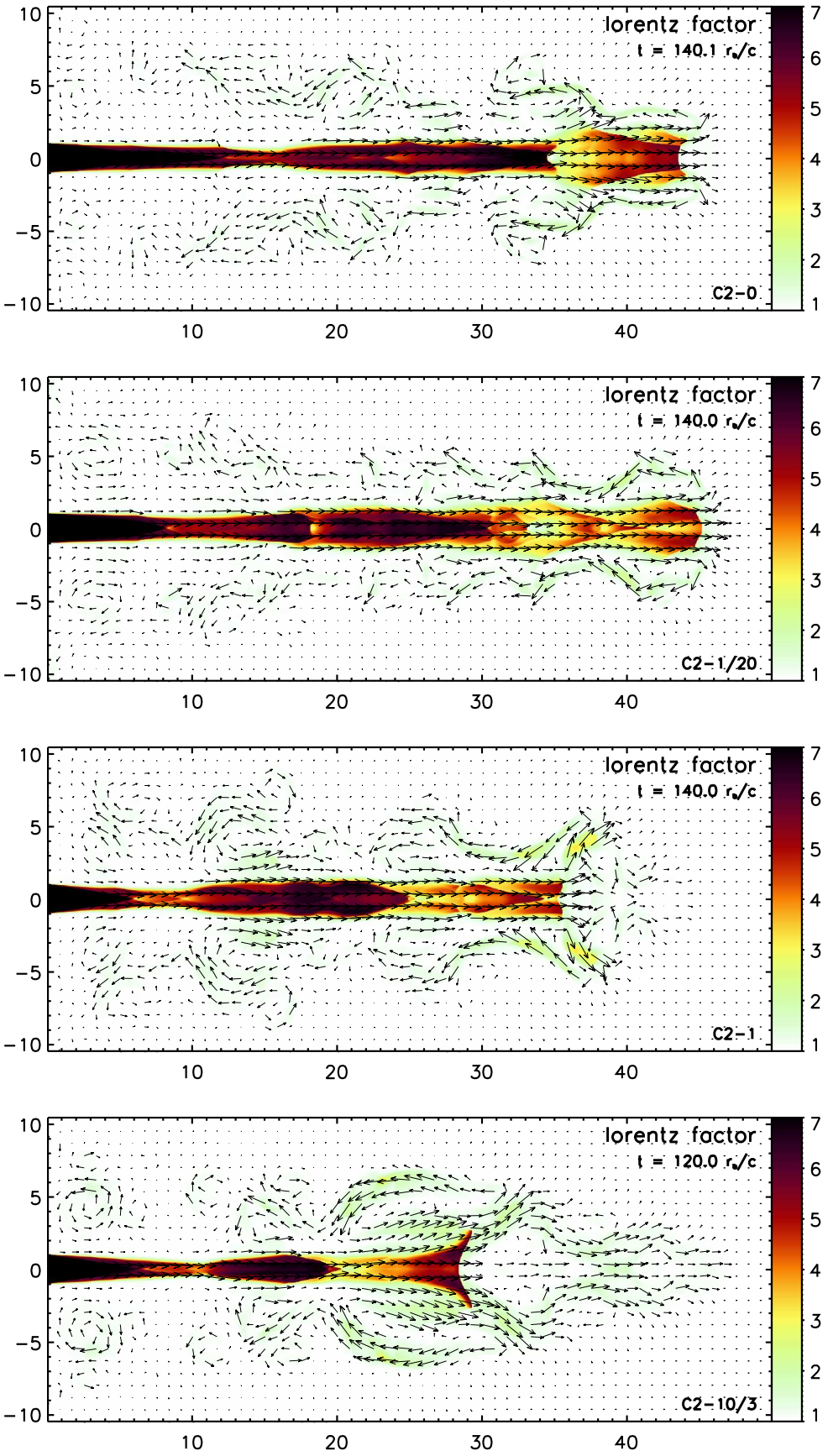

Figure 3.4: Snapshots of the Lorentz factor with velocity vectors of models C2-0, C2-1/20, C2-1 and C2-10/3 (from top to bottom).

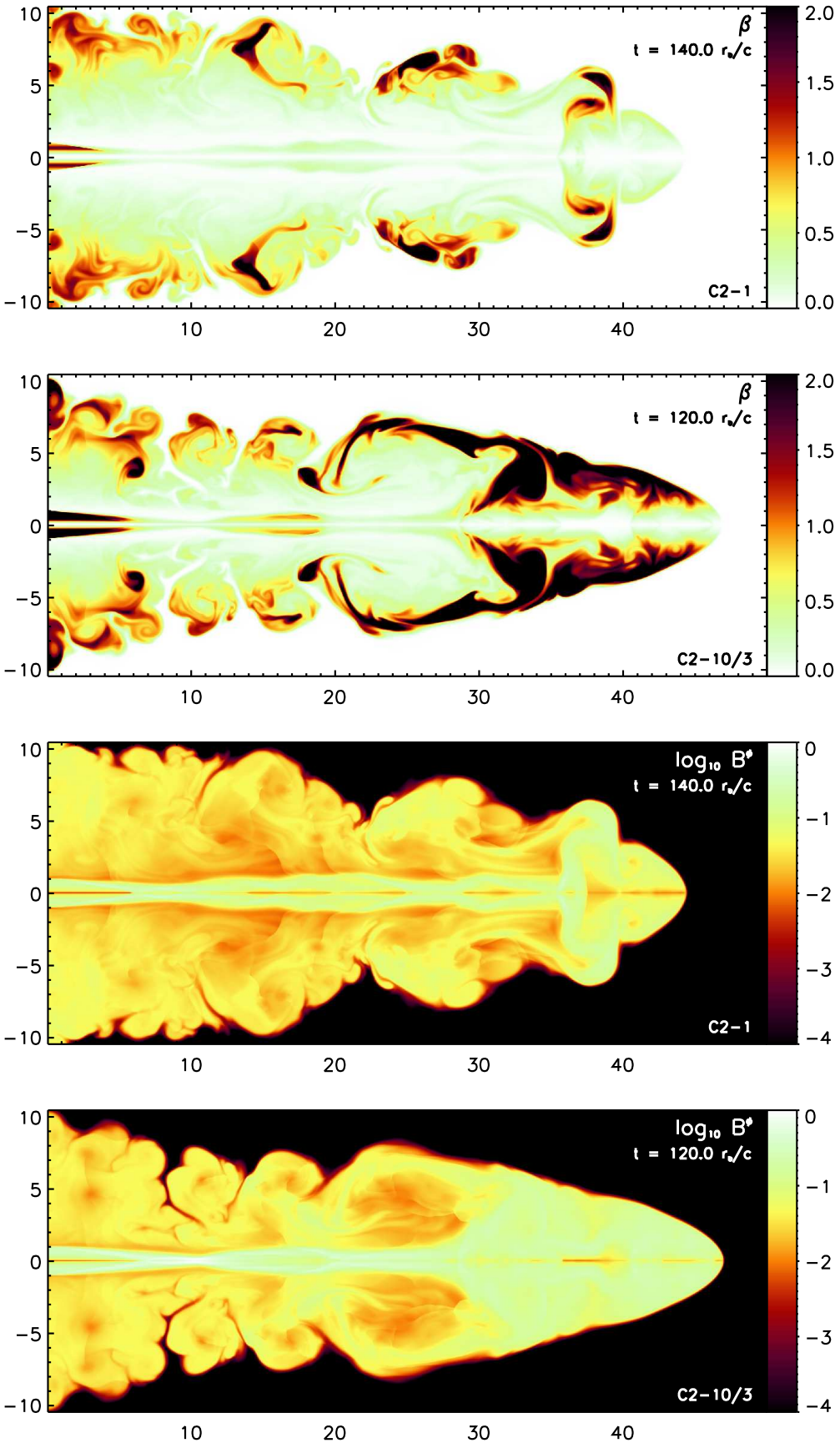

Figure 3.5: Snapshots of β (top two panels) and B^{ϕ} (bottom two panels) of the two strongly magnetised models of the C2 series.

C2-pol-1: poloidal field model

Figure 3.6 shows the rest mass density, the thermal pressure and the Lorentz factor of the poloidal field model C2-pol-1. The strength of the magnetic field and its geometry are displayed in Fig. 3.7. Although the overall morphology and structure of the jet and the cocoon of this model are very similar to those of the other C2 models, there are a number of striking differences. In particular, we will compare model C2-pol-1 with the hydrodynamic model C2-0, and the toroidal field model of the same magnetisation (C2-1).

First of all, instead of forming a narrow nose cone structure, the beam broadens close to its termination point, giving the head of the jet a hammer-like appearance. The beam plasma flows along the field lines which are bend sidewards by the expansion of the leading bow shock. This behaviour is not only reflected by the tracer contour in the top panel and the velocity vectors in the bottom panel of Fig. 3.6, but also by the field lines plotted in the top panel of Fig. 3.7.

Another difference between model C2-pol-1 and the other models is in the strength of the cross shocks on the axis. While the first cross shock in model C2-pol-1 occurs much nearer to the nozzle (at $z = 7$) than in model C2-0, it is also much weaker and has a smaller post-shock region in axial direction than any other model. Downstream of this shock, the beam pressure and density remain low until the flow reaches the second cross shock, which is also weak compared to that of the other models. It is especially weak compared to the toroidal field model with the same average β. The reason for this behaviour is the magnetic field in the beam: the Lorentz force on the axis repels waves driven into the beam. Therefore, during the whole evolution the beam remains much less affected by shocks than in the other models. The terminal shock, however, is as strong as in model C2-1 or C2-0.

Not only the beam but also the cocoon is much more homogeneous in model C2-pol-1 than in the other C2-models. This becomes especially apparent when comparing the pressure images in Figs. 3.3 and 3.6. The poloidal field model shows much fewer waves anywhere in the cocoon, whereas the other models show a much more turbulent behaviour. The back flow of beam material through the cocoon is almost straight (Fig. 3.6, bottom panel). This is a major difference to the toroidal field and purely hydrodynamic cases, where the back flow is much more violent.

Figure 3.7 shows that the magnetic field is almost completely expelled from the cocoon. In the top panel one can see that the absolute value of the field strength remains on a very low level. The narrow bright filaments in that image trace the magnetopauses, i.e. the surfaces where the magnetic field changes direction and hence becomes zero. The magnetopauses are surrounded by areas of higher magnetic field strength giving rise to the impression of extended, twisted filaments. The β parameter depicted in the bottom panel is nearly zero everywhere in the jet, further demonstrating the expulsion of the magnetic field from the cavity. The field accumulates in the shell of the jet, where the thermal pressure is very large yielding a low value of β. It is remarkable, that the poloidal field has such a large effect on the pressure in the beam and the cocoon, even though β is very small everywhere.

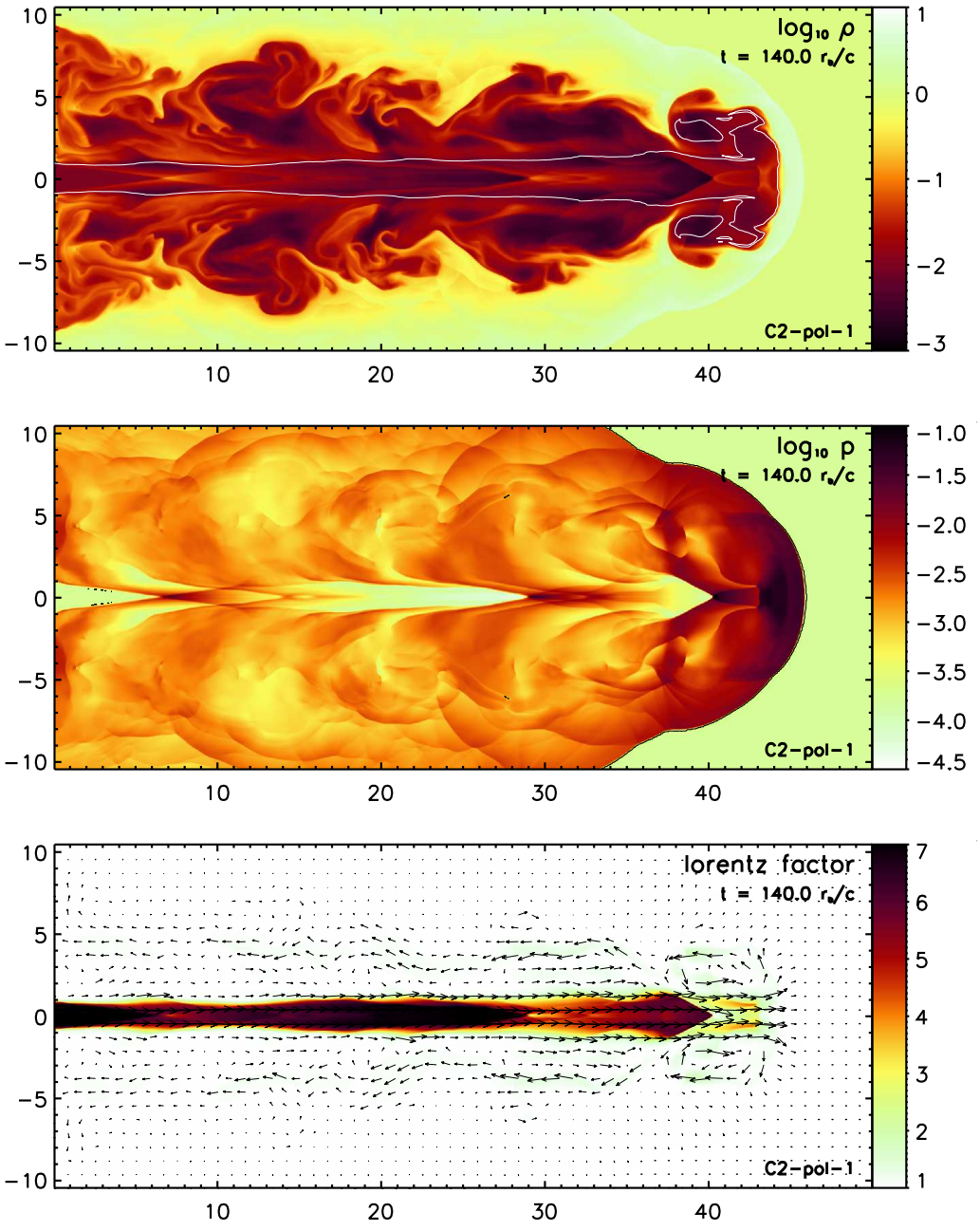

Figure 3.6: Snapshots of the poloidal field model C2-pol-1. From top to bottom: rest mass density with $f = 0.9$ contour (white), thermal pressure with $\beta = 1$ contour (black) and Lorentz factor with velocity vectors.

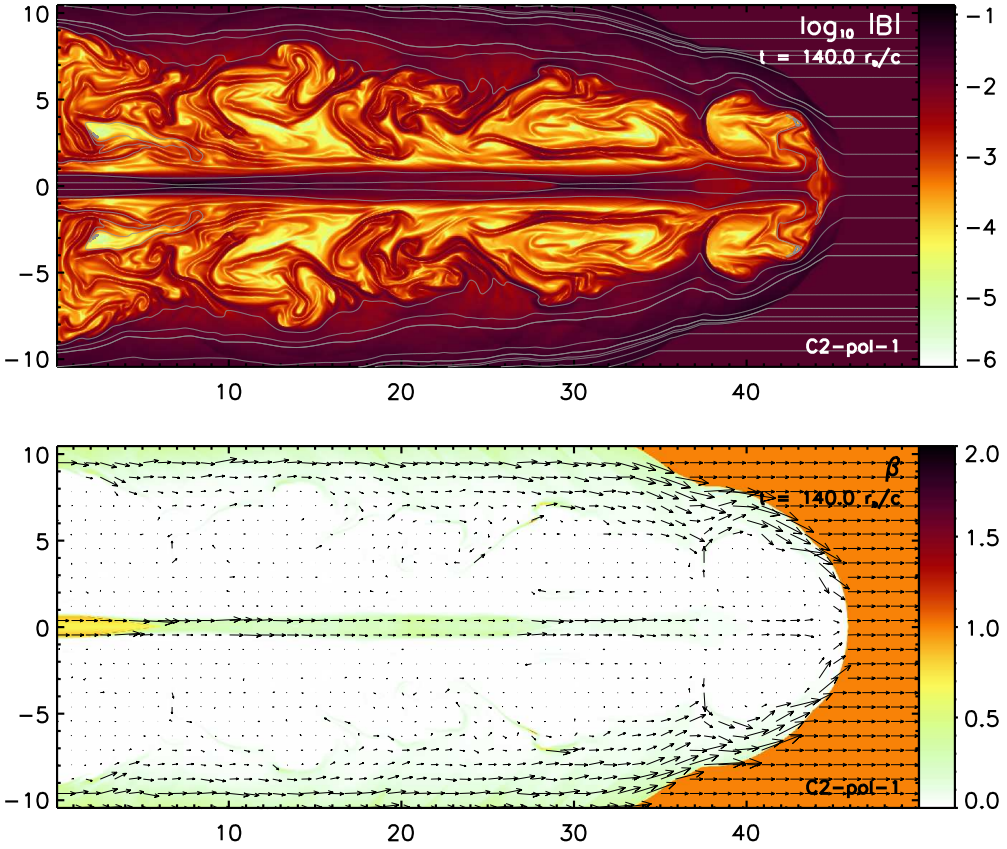

Figure 3.7: Snapshots of the poloidal field model C2-pol-1. The top panel shows the logarithm of the absolute value of the magnetic field strength with field lines superimposed. The lines are placed randomly, but weighted with the local field strength, such that on average their density reflects the field strength. The bottom panel shows β together with the magnetic field vectors.

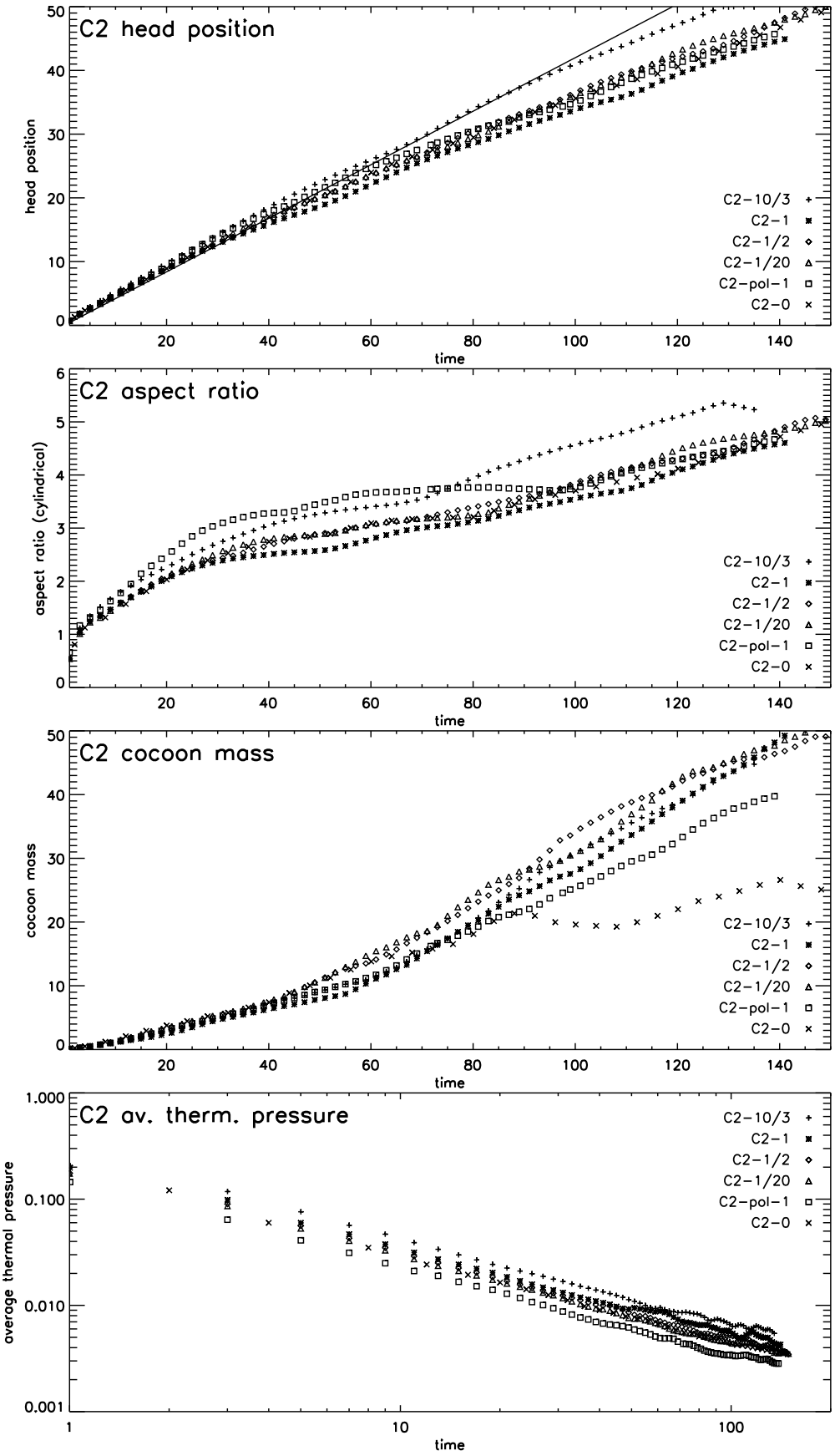

Figure 3.8: Head position, cylindrical aspect ratio, cocoon mass, and average cavity thermal pressure (top to bottom) as a function of time for all C2 models. The straight line in the top panel shows the 1D velocity given by Eq. (3.4). Time is measured in code units, i.e. r_b/c

C2: temporal evolution

The top panel of Fig. 3.8 shows the position of the jet's head versus time for all of the C2 models, including a straight line for the 1D velocity given by Eq. (3.4). Apart from model C2-10/3 the differences between the models are not large, i.e. in all the models the jet propagates at essentially the same speed. The 1D estimate gives a very good approximation to the speed in the 1D phase and becomes an upper bound in the 2D phase. Remarkably, there is no simple dependence of propagation speed on magnetic field strength: while C2-10/3 propagates fastest, C2-1 is slowest, C2-1/20 is second fastest, and the remaining models fall in between. The propagation speed of magnetised jets depends on a number of competing effects related to the strength and the configuration of the magnetic field. However, our simulations do not show a clear trend with those two parameters which means that the dependency is not linear in any of those two. The high speed of C2-10/3 can be explained by its large nose cone which has a high density and pressure, therefore increasing the momentum of the jet's head while at the same time reducing the effective area of the bow shock in the direction of propagation.

The second panel of Fig. 3.8 shows the cylindrical aspect ratio of the different models against time. Due to the fact that the jet reaches the radial boundary of the grid quite early in all of the models, the aspect ratios converge to that of the grid, which is roughly 5. The differences between the models are less then they would be on a larger grid, i.e. this plot has to be interpreted with caution. Nevertheless, our explanation for the high propagation speed of model C2-10/3 is further supported by the large aspect ratio found for this model. The other models do not show a trend.

The third panel of Fig. 3.8 shows the cocoon mass against time, i.e. the total mass with $0.1 < f < 0.9$. Obviously a toroidal magnetic helps to entrain mass. The models without magnetic field and with poloidal magnetic field entrain considerably less mass into their cocoons. The reasons for this behaviour are: (a) matter is locked into the high density nose cones, and (b) pinching modes excited by toroidal magnetic field lead to more mixing in the cocoon.

The average thermal cavity pressure of all C2 models is displayed in the bottom panel of Fig. 3.8, which follows a power law distribution of the same index in all models. Since they all have the same beam thermal pressure, a transfer of toroidal magnetic field energy to the plasma's thermal energy density must occur. Therefore, the average thermal pressure is larger for a larger toroidal magnetic field at any time of the simulation. This trend is reversed when considering poloidal magnetic fields: in model C2-pol-1 the average thermal pressure is even lower than in the non-magnetic model indicating a transfer of thermal energy into magnetic field energy.

3.4 B1 series

B1-0 to B1-10/3: purely hydrodynamic and toroidal field models

The results of the non-magnetised and toroidal field models of the B1 series are displayed in Figs. 3.9 to 3.11. The rest mass density (Fig. 3.9) shows some of the trends of the C2 series, but not all of them. In particular, the effects caused by the toroidal magnetic field do not scale linearly with magnetic field strength; the weakly magnetised model B1-1/20 behaves much different from the equipartition model B1-1 and the strongly magnetised model B1-10/3. The more magnetised models also develop nose cones preceded in the case of B1-10/3 by a magnetically confined bubble. In addition both B1-10/3 and B1-1 display a widening of the beam combined with low density pockets that are filled with beam material. The rest mass density and the pressure (Fig. 3.10) show much more structure in the two more strongly magnetised cases than in the non-magnetised case. B1-1/20, however, is exceptionally smooth. In all variables very little structure is present, as if the weak magnetic field inhibits any structure formation.

The first recollimation shock on the axis shows the same trend as in the C2 series of models. Due to magnetic pinching the shock gets stronger and occurs closer to the nozzle for stronger toroidal field. In model B1-0 the post-shock state extends from $z = 16$ to $z = 25$, in B1-1/20 from $z = 15$ to $z = 25$, in B1-1 from $z = 9$ to $z = 15$ and in B1-10/3 from $z = 6$ to $z = 18$, respectively. The strong pinching of the beam in the latter two cases leads to the widening of the beam downstream of the shock and to a reduced Lorentz factor (Fig. 3.11). The same picture holds for the second cross shock, which is also stronger than for the weak field or non-magnetised case. The flow patterns around the terminal Mach shock of the beam, described for the strongly magnetised C2 models, are also visible in models B1-1 and B1-10/3, although to a lesser degree.

In model B1-1/20 the pinching is very weak and no difference to the non-magnetised model can be recognised. Instead it is even better collimated than model B1-0, and the flow remains highly relativistic up to the terminal shock of the beam, where the beam plasma is deflected and flows backwards smoothly in a very thin layer around the beam. This behaviour explains why model B1-1/20 has propagated further than the other models in the same time. This implies, that with the right combination of parameters, a small toroidal field helps to collimate the beam without producing too much pinching, which helps to keep the jet stable.

Figure 3.12 shows the magnetisation, β, and B^ϕ for the two models B1-1 and B1-10/3. As for the corresponding C2 models the initial magnetisation of the beam is reduced very much in the first cross shock. It is strongest near the beam's terminal shock, where the plasma flows radially away from the axis leading to the formation of the nose cone through the forward directed Lorentz force. Apart from the fact that the structures are much narrower than in the C2 models, the overall distribution of β and B^ϕ is very similar everywhere in the cavity. β varies radially: it is lowest near the axis and increases until it reaches its maximum value in the magnetic shell. B^ϕ remains largest in the beam and in the nose cone.

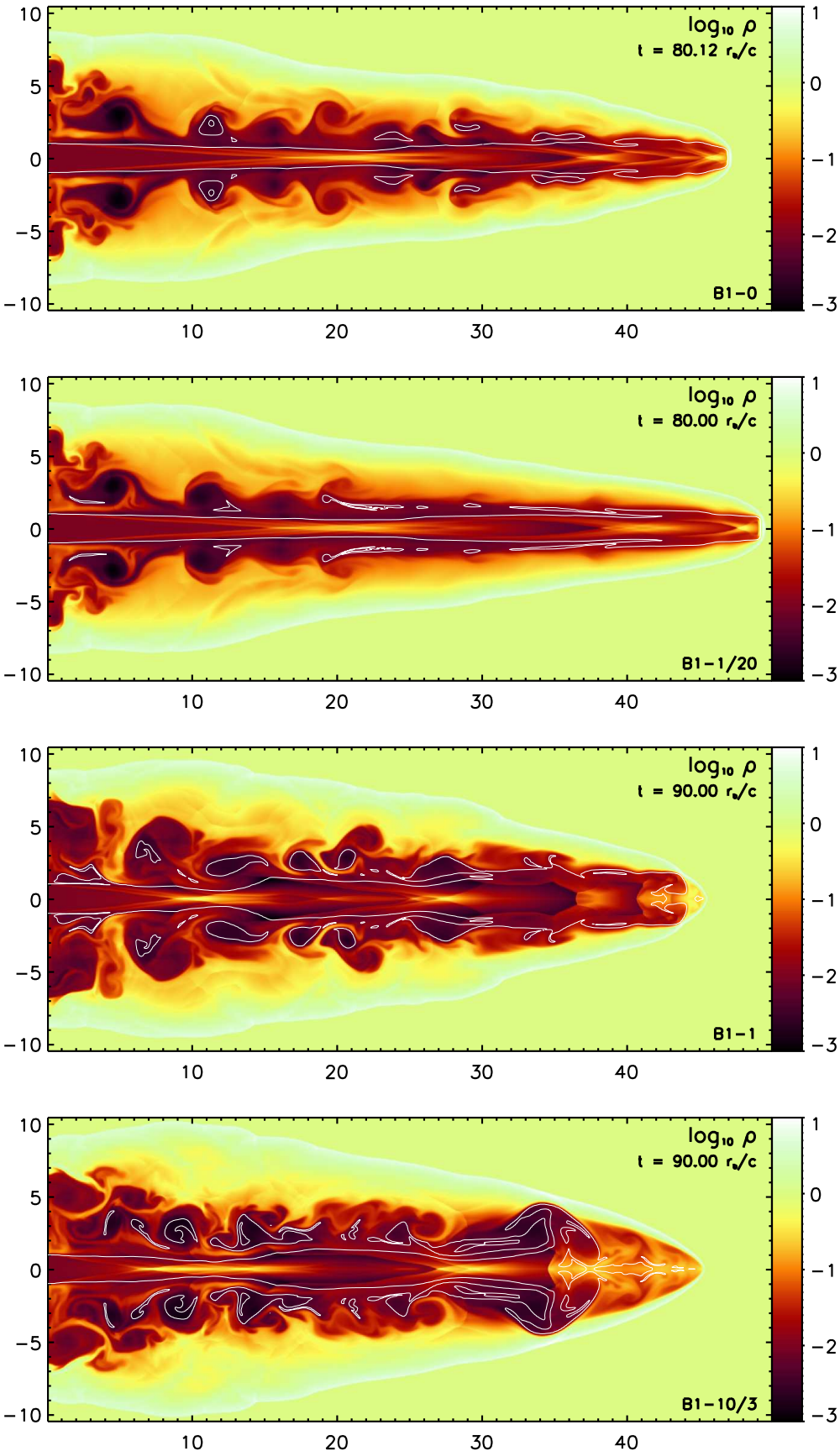

Figure 3.9: Snapshots of the logarithm of the rest mass density of models B1-0, B1-1/20, B1-1 and B1-10/3 (top to bottom). The white lines are contours of the tracer variable $f = 0.9$

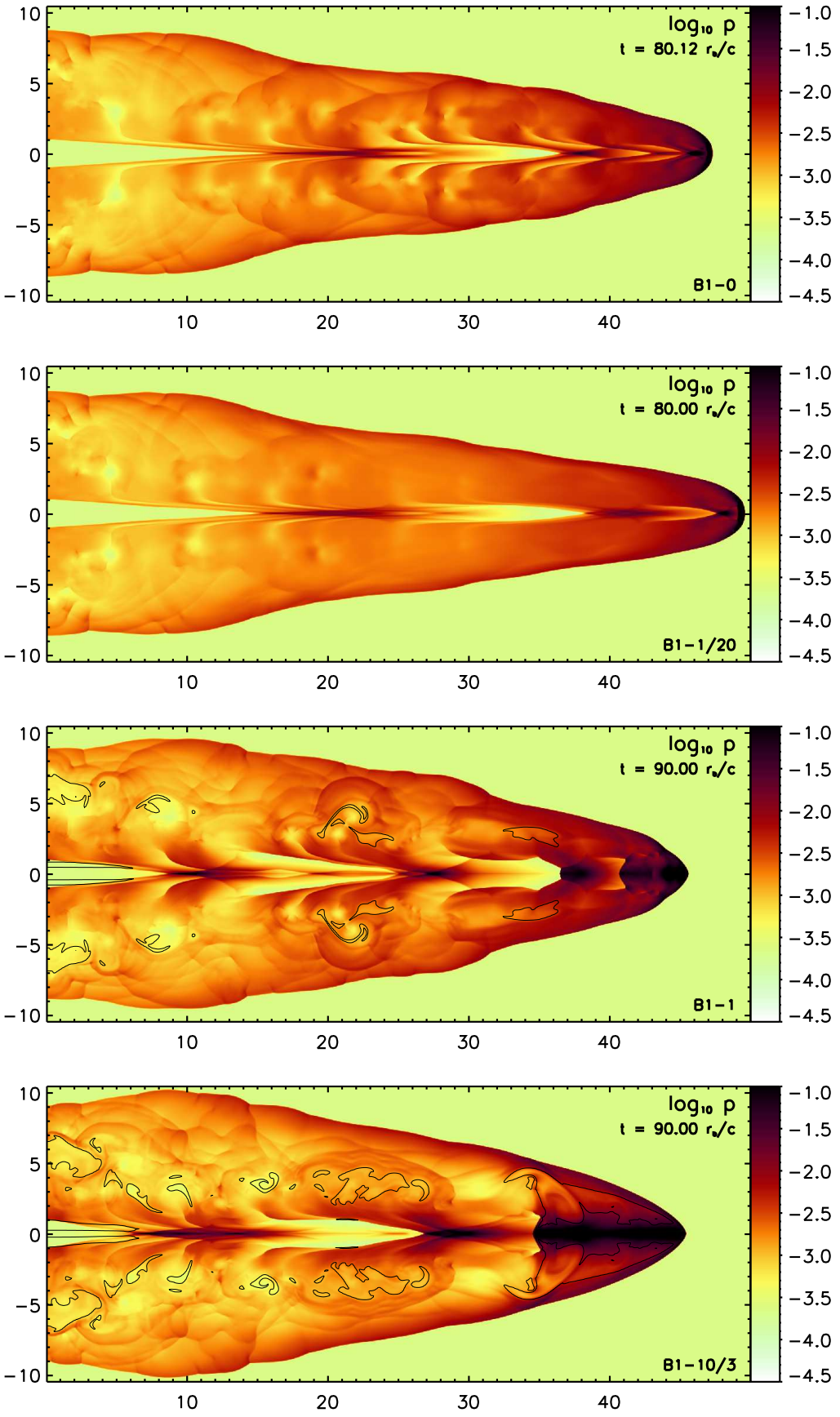

Figure 3.10: Snapshots of the logarithm of the thermal pressure of models B1-0, B1-1/20, B1-1 and B1-10/3 (top to bottom). The black contour is the line of equipartition where $\beta = 1$.

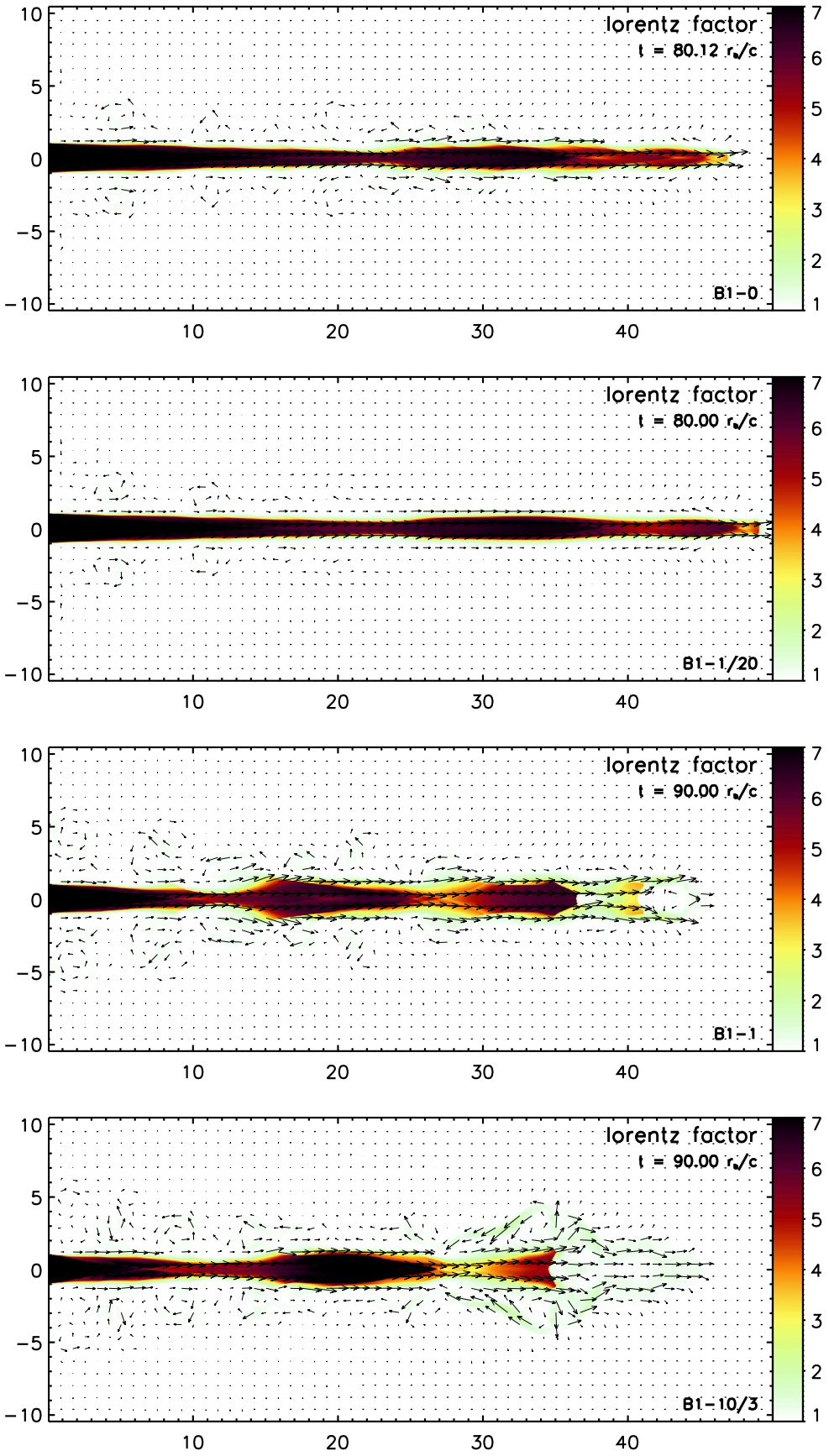

Figure 3.11: Snapshots of the Lorentz factor with velocity vectors of models B1-0, B1-1/20, B1-1 and B1-10/3 (top to bottom).

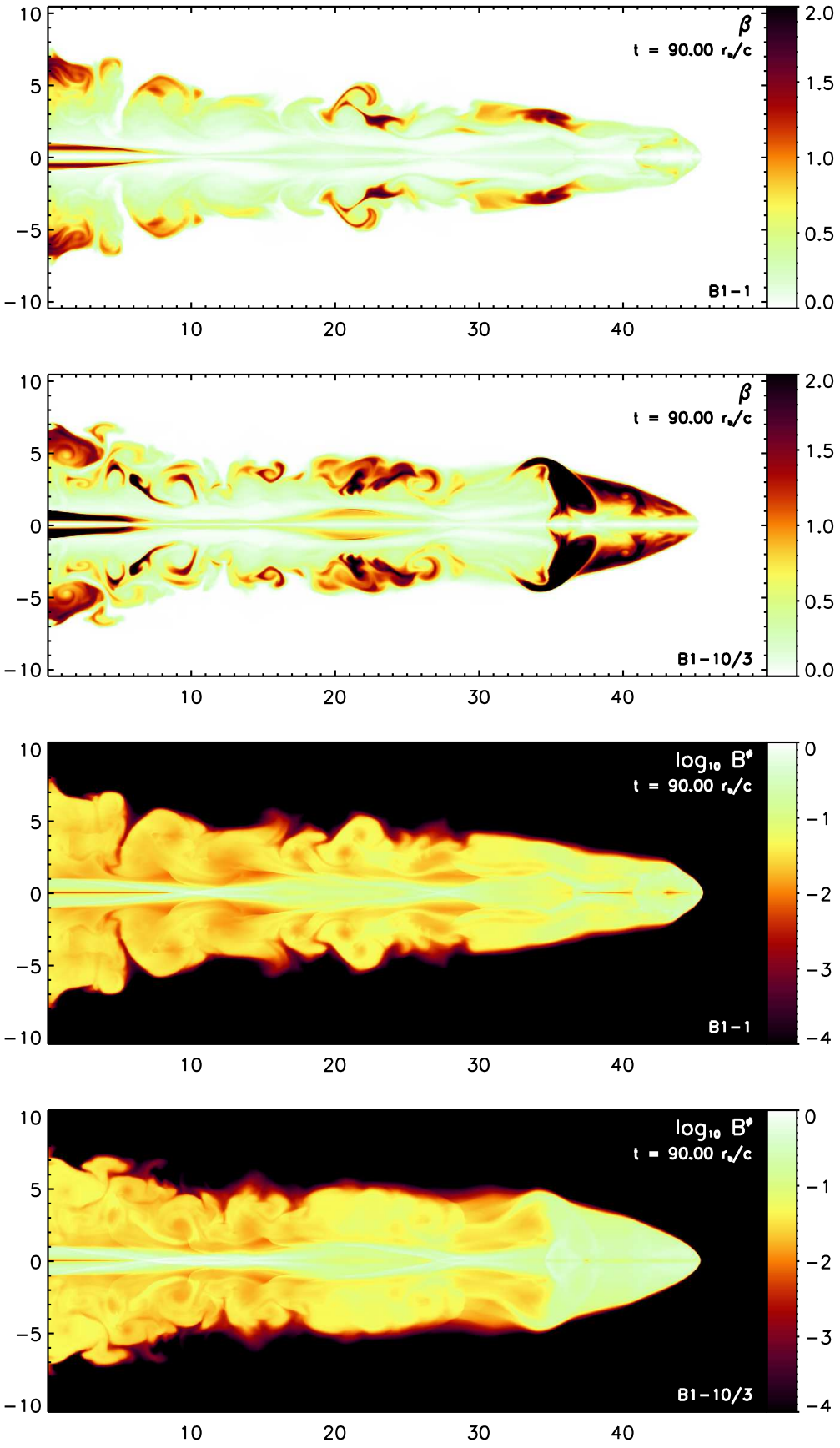

Figure 3.12: Snapshots of β (upper two panels) and B^{ϕ} (lower two panels) for the two strongly magnetised models of the B1 series.

B1-pol-1: poloidal field model

Figure 3.13 shows snapshots of the rest mass density, the thermal pressure and the Lorentz factor of model B1-pol-1. The magnetic field strength and the β parameter of the same model are displayed in Fig. 3.14. Most of the features described for model C2-pol-1 are also present in B1-pol-1: the whole jet is extraordinary smooth, both in density and pressure, the cocoon showing only an indication of an eddy. The beam is almost undisturbed, and the cross shocks are very weak. The back flow is confined to a narrow region directly around the beam, and is absolutely straight. But whereas model C2-pol-1 develops a hammer-like head with beam plasma flowing away radially from the axis, B1-pol-1 shows no such behaviour. Instead the beam remains well collimated up to the very tip of the jet until it reaches the terminal shock. This is possibly a consequence of the magnetisation parameter: the $\beta = 1$ contours in the pressure snapshot (Fig. 3.13) show that most of the beam itself is strongly magnetised. This is confirmed by the distribution of the β parameter (Fig. 3.14, bottom panel). Values between $1 < \beta < 2$ hold for the most part of the beam.

The smoothness of the cocoon can doubtlessly be explained by the presence of the axial field. As shown in the top panel of Fig. 3.14, the field almost retains its purely axial structure. It is only twisted in the narrow low density sheet around the beam, and even there, the twist seems to be mostly aligned with the axis. This does not favour the formation of eddies, which could drive strong shocks into the beam. As in C2-pol-1, $\beta \approx 10^{-6}$ in a large part of the cavity, which however, does not diminish the effect of the poloidal field on the morphology of the jet.

When comparing to the toroidal field models of the B1 series, it is most surprising that the overall morphology of the leading bow shock is so similar given the differences in the internal structure and in the beam. However, since the final evolutionary times of the complete B1 series are so small (because these jets propagate faster and reach the edge of the computational grid sooner than in other models), we suppose that the differences would affect the propagation and dynamics of the jet more strongly later in the evolution.

Temporal evolution

The top panel of Fig. 3.15 shows the head position, l_c, of the B1 jets versus time. Again, the propagation speed does not depend linearly on the magnetic field strength. However, in contrast to the C2 jets (Fig. 3.8), the weakest toroidal field jet propagates faster than all other models, followed by the pure hydro model and the poloidal field model. At $t = 80$ the strongest toroidal field model has the smallest l_c. The reason for this behaviour has already been described above: the weak toroidal field collimates the beam of B1-1/20 and smoothes the surrounding cocoon. In addition, the form of the leading bow shock is equally pointy in all of the B1 jets. This behaviour is also reflected by the aspect ratio (Fig. 3.15). The only difference here is that the poloidal field model B1-pol-1 is even more elongated than model B1-1/20, because the initial axial field inhibits sideways expansion and leads to the elongated morphology of this model. Note that, in this case, the 1D estimate is a lower bound

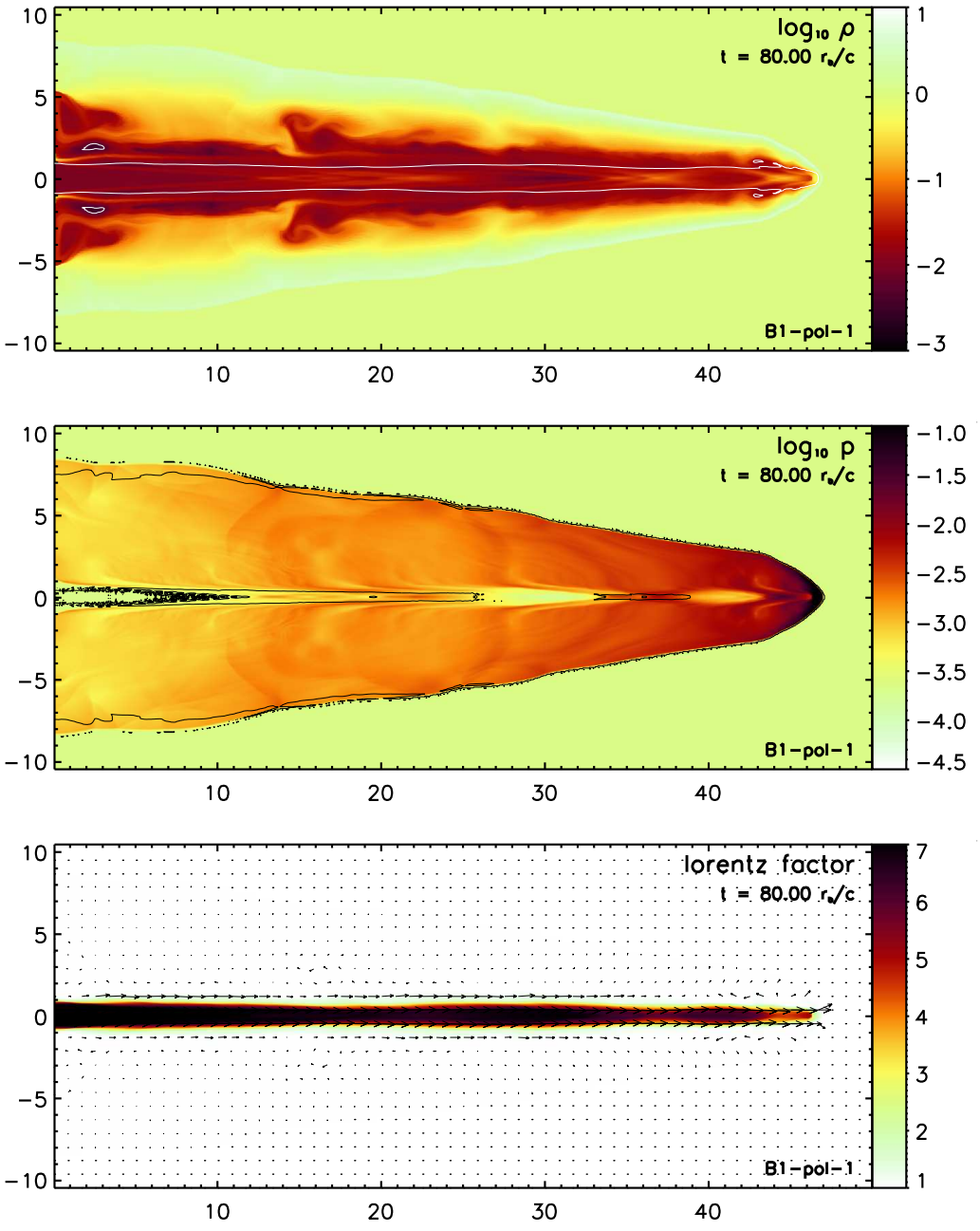

Figure 3.13: Snapshots of the poloidal field model B1-pol-1. From top to bottom: rest mass density with $f = 0.9$ contour (white), thermal pressure with $\beta = 1$ contour (black) and Lorentz factor with velocity vectors.

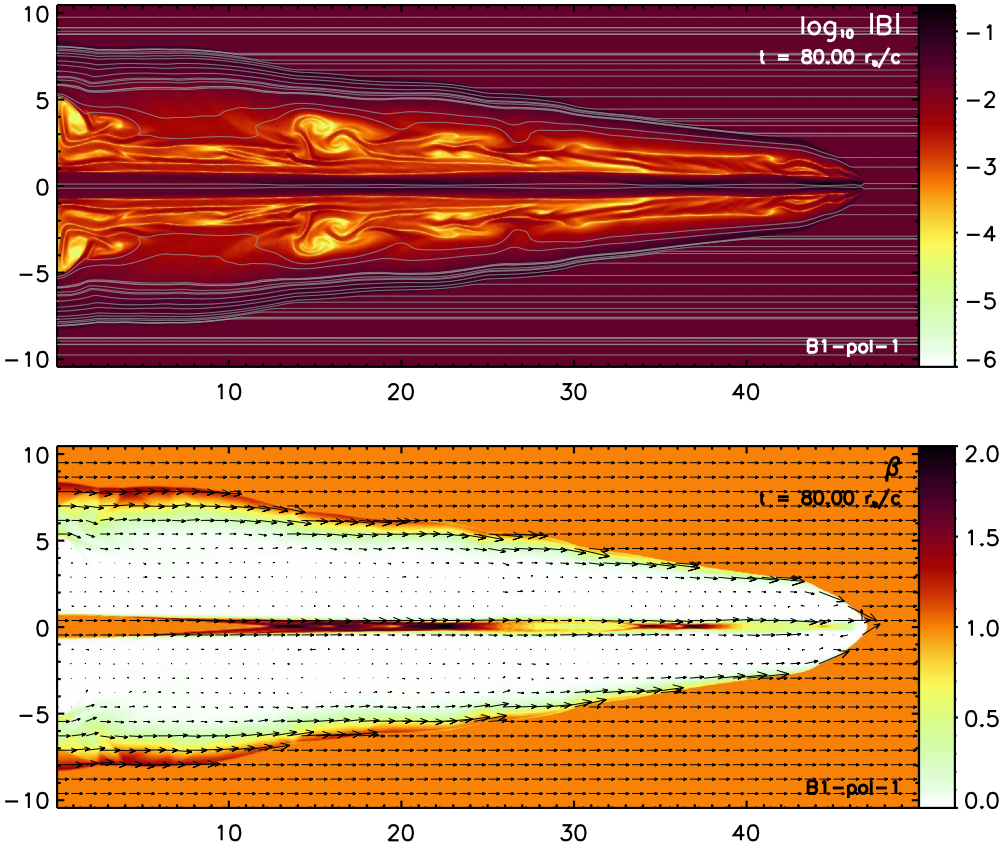

Figure 3.14: Snapshots of the poloidal field model B1-pol-1. The top panel shows the logarithm of the absolute value of the magnetic field strength with field lines superimposed. The lines are placed randomly but weighted with the local field strength, such that on average their density reflects the field strength. The bottom panel shows β together with magnetic field vectors.

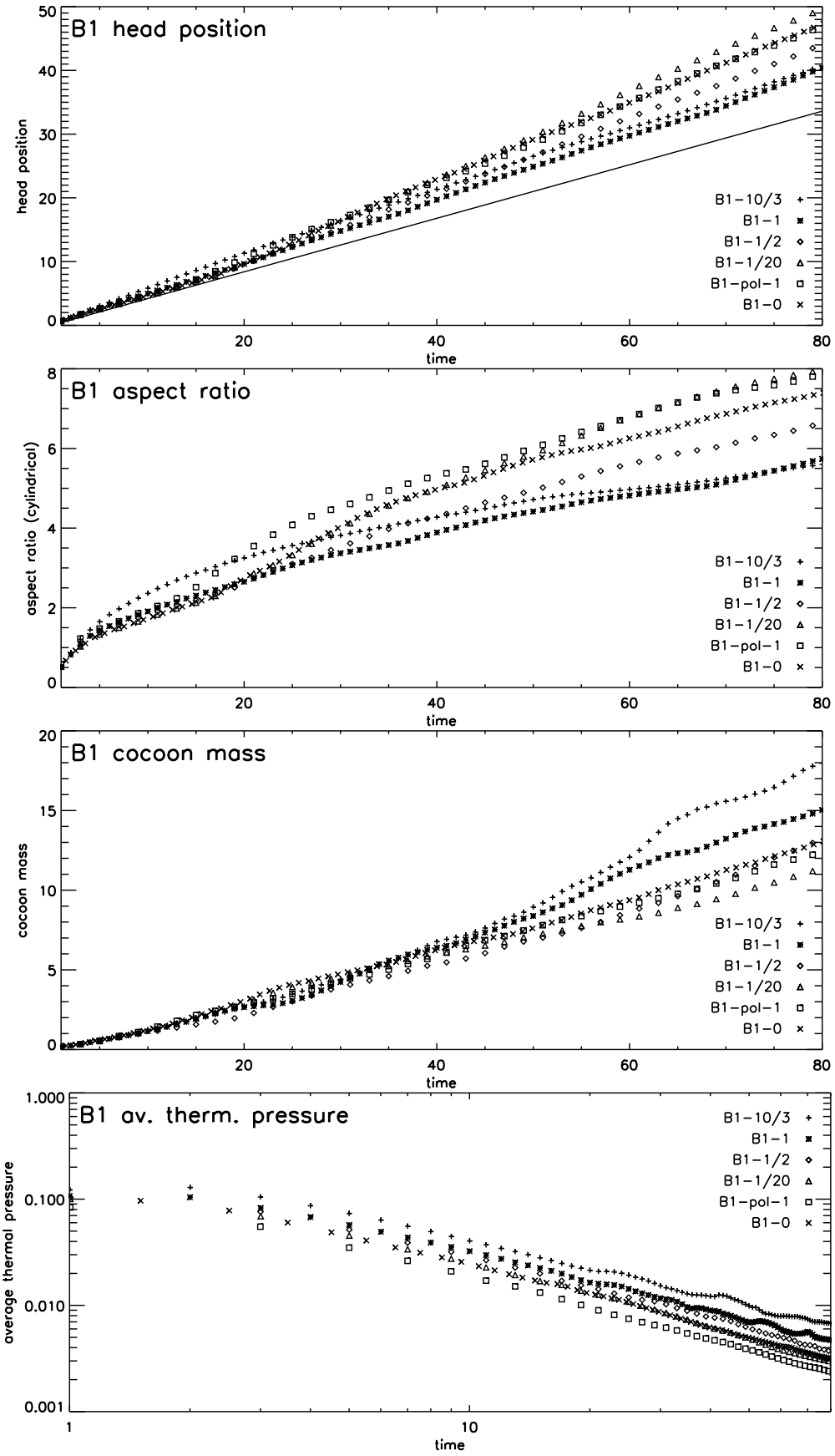

Figure 3.15: Head position, cylindrical aspect ratio, cocoon mass, and average cavity thermal pressure (from top) as a function of time for all B1 models. The straight line in the top panel shows the 1D velocity given by Eq. (3.4).

for the propagation velocity.

The cocoon mass of the B1 models (Fig. 3.15, third panel) follows the same trend as in the C2 series, although the differences between the models are not as drastic. The stronger toroidal field models B1-1 and B1-10/3 entrain considerably more mass than the other models, whereas the weakest toroidal field model B1-1/20 entrains the least mass of all B1 jets. This is to be expected from the same two reasons described above: the beam plasma of B1-1/20 does not mix very much with the ambient plasma, and its cocoon morphology is the smoothest of all the models described here.

The temporal evolution of the average thermal pressure in the jet also follows the same trend as for the C2 jets. Toroidal magnetic field energy is transfered to thermal energy leading to an overall larger average pressure. In the poloidal field case the behaviour is the opposite. As before, the average pressure follows a power law distribution.

3.5 C1 series

Toroidal and poloidal field models

Figures 3.16 to 3.18 show the rest mass density, the thermal pressure and the Lorentz factor of all the models of the C1 series, respectively. Many of the effects of the different magnetic field configuration described in the previous sections also hold for the C1 series, some of them greatly enhanced compared to the other models.

Concentrating on the toroidal field models (middle panels in Figs. 3.16 to 3.18), we can immediately see the large nose cones in both models. In model C1-10/3 the nose cone covers up 50% of the total length of the jet. It has a high density and pressure spine consisting of beam plasma preceded by a large low density bubble filled up with beam material. The same structure is visible in the results of C1-1, although the nose cone is only half as long as in C1-10/3.

A second effect already observed in the B1 and C2 series is the growing strength of the cross shocks with increasing toroidal field. In the case of the C1 models this is not only true for the first cross shock (which is also closer to the nozzle in the toroidal field models), but for all four cross shocks visible in the pressure images of models C1-0, C1-1 and C1-10/3 (Fig. 3.17). These snapshots also indicate the reason for this behaviour: according to the $\beta = 1$ contours both toroidal field models are dominated by magnetic pressure in most of their cocoons. The distribution of the β parameter (Fig. 3.19) further illustrate this. It also explains the high pressure and density spine of the nose cone of model C1-10/3, which is confined by completely magnetically dominated material.

The strong cross shocks in the two toroidal field models lead to an early decrease of the Lorentz factor in the beam, which, in particular in the second cross shock, drops to values near 1. This does not imply, however, that the propagation speed of the whole jet is lower in the toroidal field cases. Quite the opposite is true. The back flow of beam plasma through the cocoon is confined by the toroidal field, and

is thus slower and less expansive than in C1-0 (Fig. 3.18).

The poloidal field model C1-pol-1 also shows the same, but enhanced, features as model C2-pol-1. The density and pressure morphology look very similar to that of C1-0, which also has a similar propagation speed. However, the pressure distribution (bottom panel of Fig. 3.17) reveals that the cross shocks on the axis are weaker than in the non-magnetised model. In addition, the pressure in the cocoon is slightly more homogeneous. The tracer contour in the density snapshot (bottom panel of Fig. 3.16) shows the same hammer-like head structure as observed in model C2-pol-1. In combination with the field line plot (top panel of Fig. 3.20) it becomes clear that the beam material follows the magnetic field lines at the end of the jet and flows away radially from the axis, thereby forming the hammer-like head structure.

Model C1-pol-1 displays the same magnetisation structure as C2-pol-1, but the shell has a larger magnetisation (bottom panel of Fig. 3.20). The magnetic field is almost completely expelled from the jet's cocoon, being reduced by four to five orders of magnitude compared to the initial value (top panel of Fig. 3.20). Only twisted filaments of larger magnetic field strength survive inside the cocoon, which also have a higher density than the rest of the cocoon.

Temporal Evolution

The top panel of Fig. 3.21 shows the head position, l_c, of all the C1 models versus time. The straight line is given by the 1D velocity, Eq. (3.4), which is that of three of the models up to an evolutionary time of $t \approx 80$. Only model C1-10/3 propagates faster from the very beginning of its evolution, and shows no sign of slowing down during the whole simulation time. The head's position grows linearly with time until the jet leaves the computational domain. The other three models leave the 1D phase at around $t = 80$ and start slowing down. Model C1-1 is still faster than the poloidal field and non-magnetised models, the latter two following a similar trajectory. Thus, there is a clear distinction between the different field configurations: toroidal fields lead to a speed up of the propagation by almost 100% in the case of model C1-10/3 and about 20% in the case of model C1-1 compared to C2-0. The poloidal field does not have a large effect on the propagation speed of the jet; model C1-pol-1 shows only a slightly stronger deceleration compared to model C1-0 at the very end of the simulation.

The cylindrical aspect ratio is displayed in the second panel of Fig. 3.21. As with the C2 series this plot has to be treated with caution, since all the models reach the edge of the grid in radial direction quite early in the simulation. Thus all the aspect ratios will converge to the aspect ratio of the grid itself, which is approximately 5. Nevertheless, the differences between the models are larger than suggested by their propagation speeds alone. While model C1-10/3 has a much larger aspect ratio than any of the other models, probably because of its long nose cone, the two equipartition models, C1-1 and C1-pol-1, have similar aspect ratios for the first 140 time units. After that point C1-1 evolves differently and its aspect ratio almost doubles until the end of the simulation. C1-pol-1, however, maintains a constant aspect ratio of around 2.4 until it reaches the end of the radial grid at $t \approx 300$. The aspect ratio

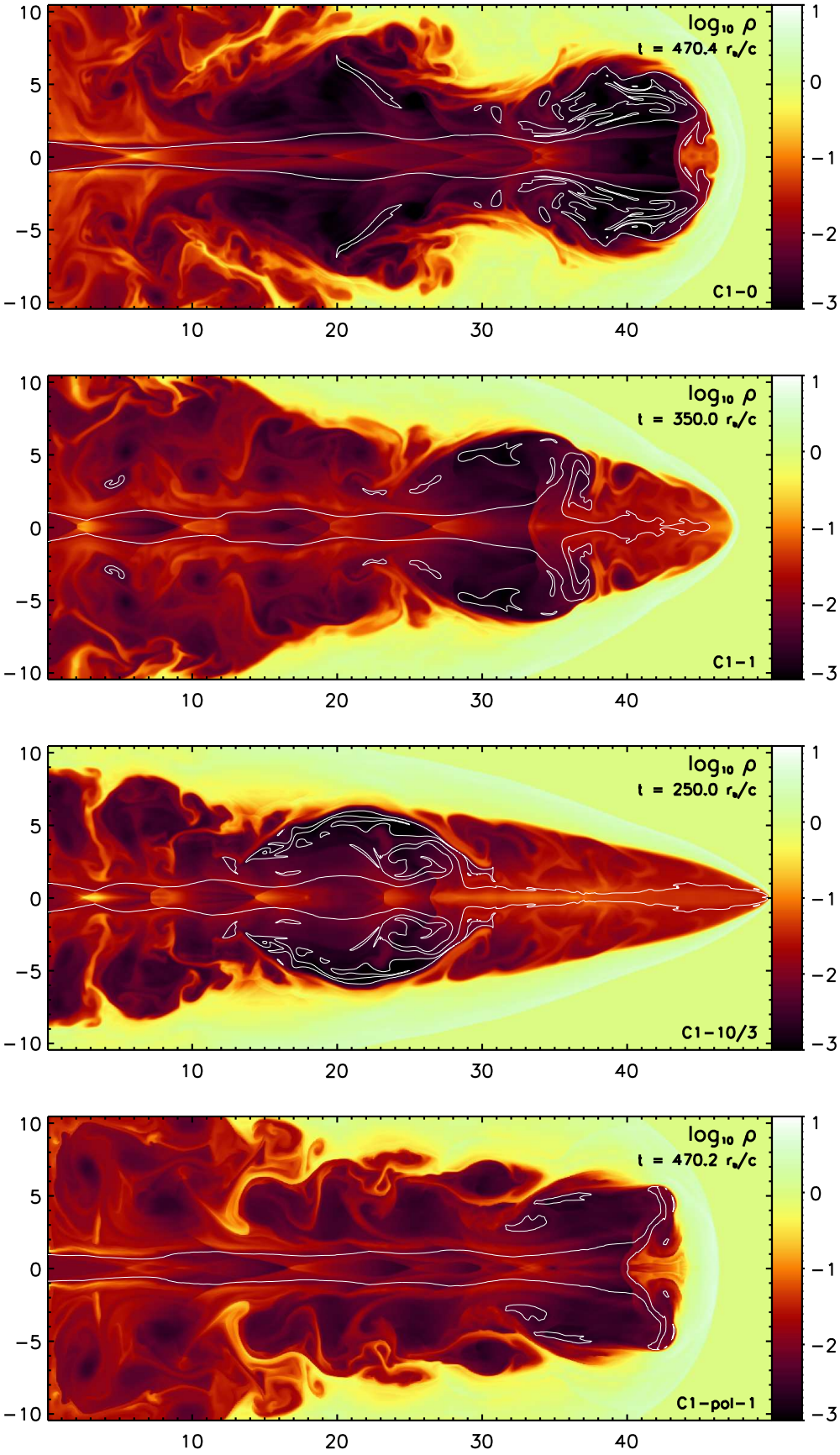

Figure 3.16: Snapshots of the logarithm of the rest mass density of all C1 models. The white lines are contours of the tracer variable $f = 0.9$

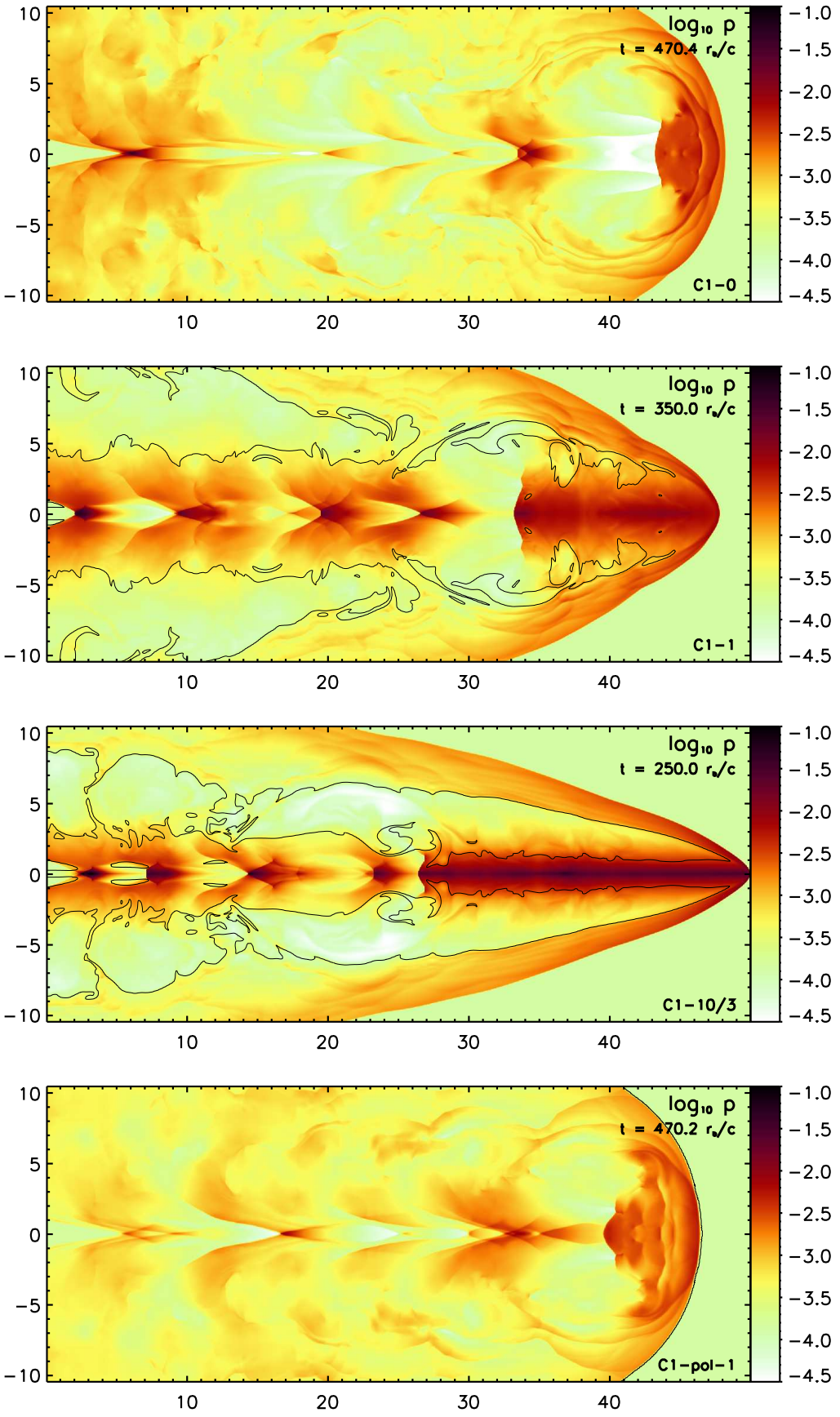

Figure 3.17: Snapshots of the logarithm of the thermal density of all C1 models. The black contour is the line of equipartition where $\beta = 1$.

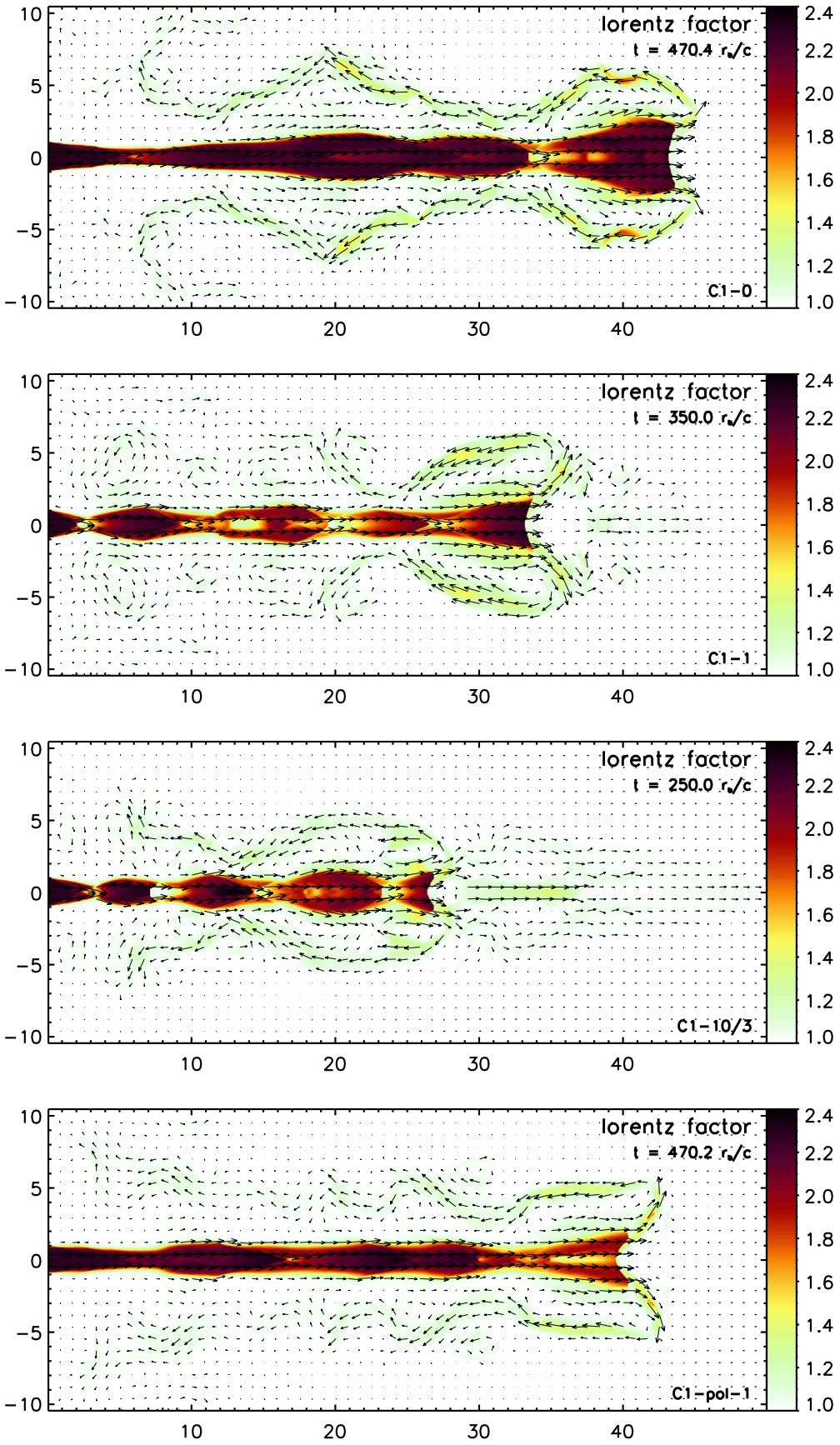

Figure 3.18: Snapshots of the Lorentz factor with velocity vectors of all C1 models.

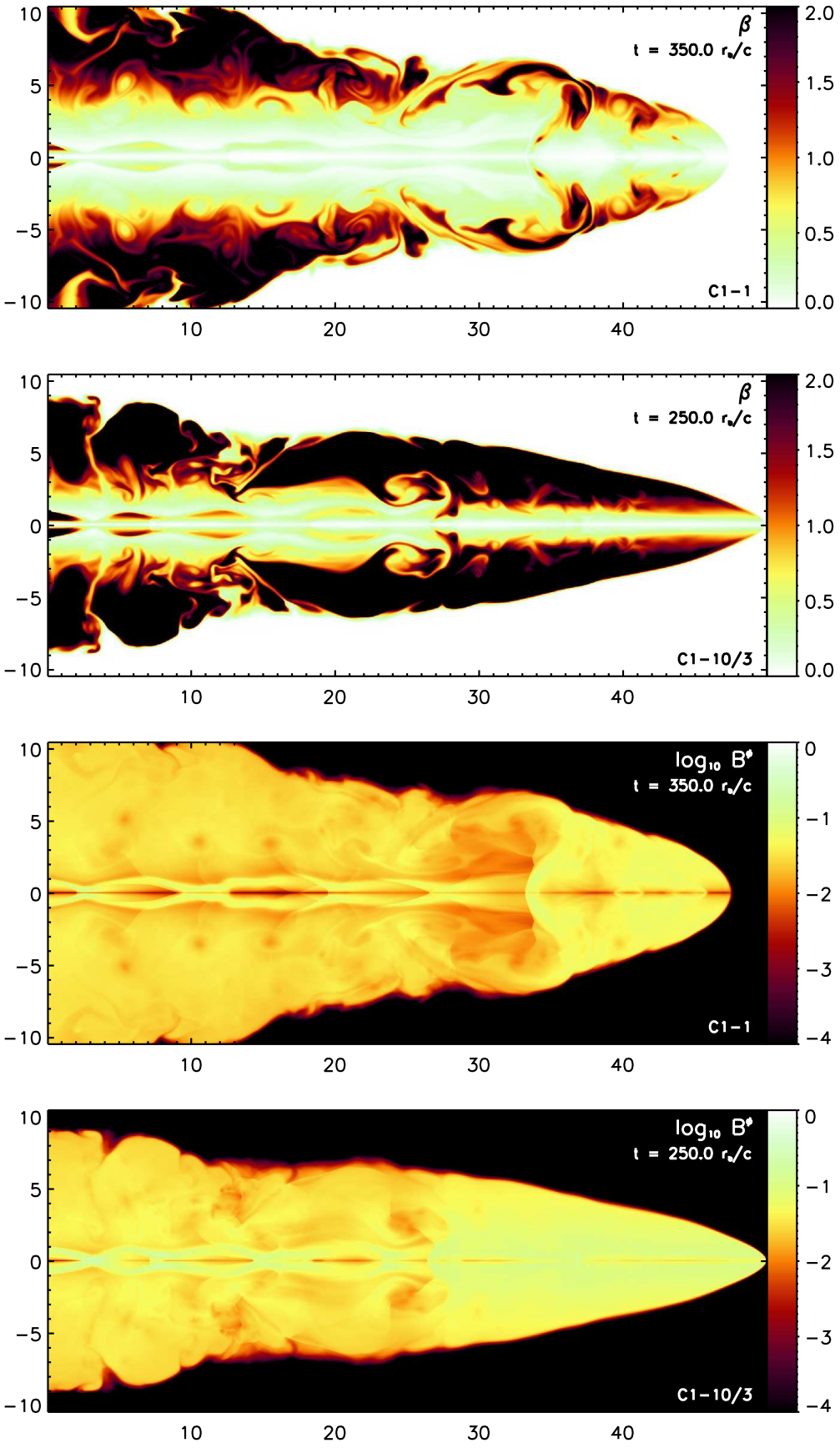

Figure 3.19: Snapshots of β (upper two panels) and B^{ϕ} (lower two panels) for models C1-1 and C1-10/3.

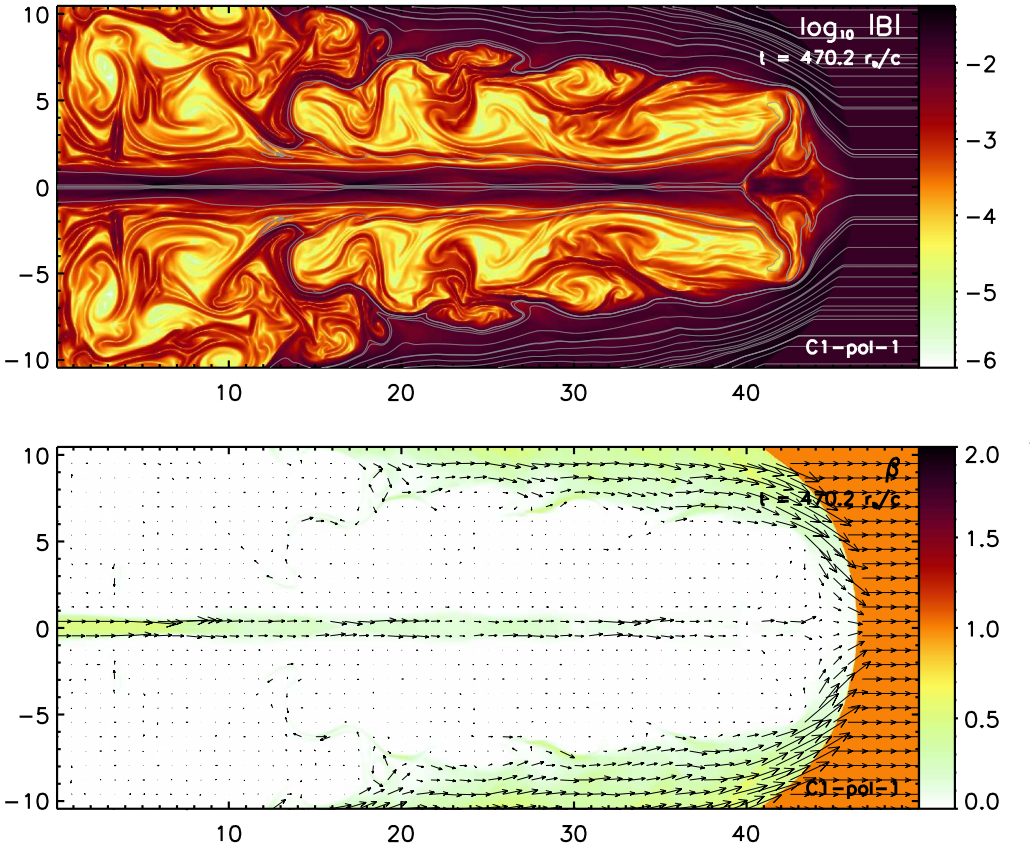

Figure 3.20: Snapshots of the poloidal field model C1-pol-1. Absolute value of the magnetic field with randomly placed field lines and β with vectors of magnetic field.

of C1-0 is even smaller in the beginning, but starts to divert from that low value earlier in the simulation.

The plots of the cocoon mass vs. time, displayed in the third panel of Fig. 3.21, show a radically different behaviour from that of the B1 and C2 series of models. Whereas in the other two series the toroidal field models carry the most mass in their cocoons, C1-pol-1 is the record holder in the C1 series. C1-10/3, the model with the strongest toroidal field even carries the least mass. This can be explained by the magnetic confinement to the axis: since the density is high near the axis, where the zone volumes are small, the total mass is not as large as in the case where the cocoon is more spread out sideways. Therefore, C1-10/3 with its extreme aspect ratio does not carry as much mass as C1-pol-1 with a low aspect ratio, but where the cocoon extends further radially and thus encompasses a larger volume. The mass of the cocoon of C1-1 only starts growing rapidly at $t \approx 160$, approximately the same time when the aspect ratio of this model starts to increase, too. This is also the point in time when C1-1 starts forming its high density nose cone. C1-0 carries less mass than the two equipartition models and only a little bit more than the extreme toroidal field model. Note that the mass in the C1 models is much smaller than that in the C2 models at the same time because of the smaller propagation speeds. For the same reason the mass in C1 is larger than that in the C2 models when comparing

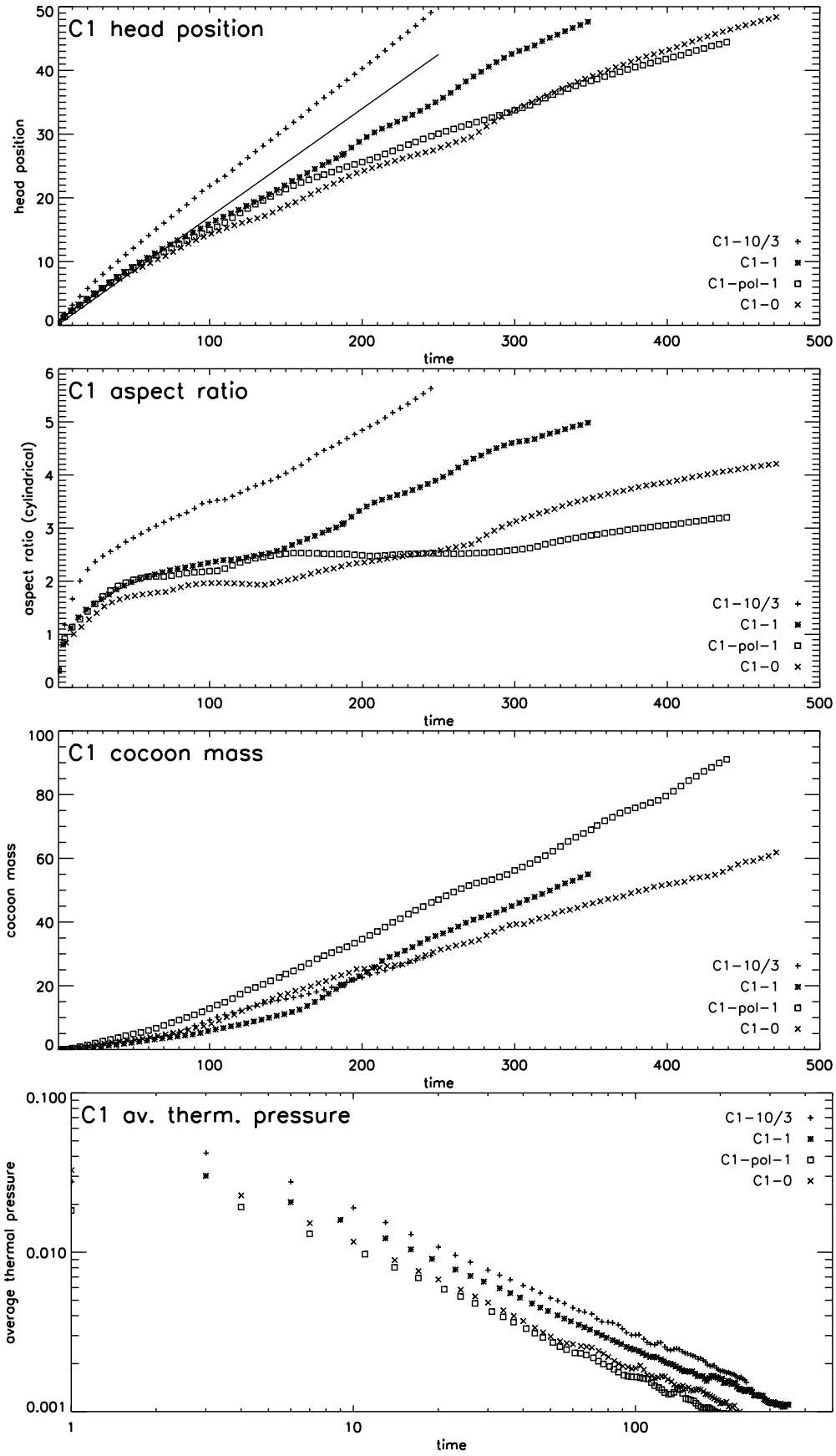

Figure 3.21: Plots of the head position, the cylindrical aspect ratio, the cocoon mass, and the average cavity thermal pressure against time for the different models. The straight line in the top panel shows the 1D velocity given by Eq. (3.4).

at the end of the simulations.

The bottom panel of Fig. 3.21 gives the average thermal pressure in the jet versus time. As already seen in the case of the B1 and C2 series, the evolution follows a power law distribution. Furthermore, the trend that higher toroidal field leads to higher thermal pressure, and that poloidal field leads to lower thermal pressure is confirmed by the C1 series of models.

3.6 Discussion

The most remarkable result of the simulations is that the inclusion of the magnetic field leads to diverse effects which do not always scale linearly with the relative strength of the magnetic field. There are, however, some clear trends which we will discuss here.

Morphology

The most prominent feature caused by the toroidal magnetic field is the nose cone. As found in previous Newtonian (e.g. Clarke et al., 1986; Lind et al., 1989; Kössl et al., 1990) and relativistic simulations (Komissarov 1999*b*, see also Sec. 2.3.2) this structure occurs for jets with toroidal fields of equipartition strength or larger and $\sigma \gtrsim 0.01$. The reason for the formation of the nose cone is the magnetic pinching by the Lorentz force which acts inwards radially near the beam. The magnetised beam plasma (which in a non-magnetised beam is deflected from the Mach disk shock and flows backwards inflating the cocoon) is partially forced to flow around the Mach disk into the nose cone. Only a smaller fraction of the beam plasma (namely the less magnetised fraction for which the Lorentz force is not as strong) flows backwards into the bubble like structure that resides upstream of the nose cone, thus forming a similar cocoon as the hydrodynamic model. This procedure explains a number of the properties of nose cones: (a) the larger the magnetisation of the beam plasma, the stronger is the Lorentz force acting on its flow. Thus, more of the shocked beam plasma is forced into the nose cone which in turn gets larger with larger magnetisation of the beam at the cost of a lower inflation of the cocoon; (b) nose cones contain larger magnetic fields than cocoons, because only the weakly magnetised plasma flows into the cocoon, and (c) the tracer variable in the nose cone is larger for large magnetisation, as a larger fraction of the beam plasma is injected into the nose cone. The high magnetic field in the nose cone itself is the cause for the confinement to a narrow region with a high pressure (approximately two orders of magnitude higher than the external pressure in the $\overline{\beta} = 10/3$ models) and high density ($\sim 10\rho_b$) spine.

Since a considerable fraction of shocked beam plasma is locked in the nose cone, it cannot flow back in the direction of the nozzle and drive the radial expansion of the cavity. However, most of the toroidal field models do not appear thinner than their corresponding hydrodynamic reference models, their aspect ratios are not much different (Figs. 3.8, 3.15, 3.21). In fact, B1-1 and B1-10/3 have lower aspect

ratios than B1-0. How is this possible, when they have "lost" part of their shocked beam plasma into their nose cones? It is again the Lorentz force that acts upon the back flowing beam plasma, but this time in outwards radial direction. This creates an additional driving force for the expansion of the cavity, and can explain the opposite trends observed in the evolution of the aspect ratios of C1-10/3 and B1-10/3. While both models have the same strong magnetic field, the nose cone of the former is much larger than that of the latter, leaving a much lower fraction of highly magnetic field plasma to drive the radial expansion of the cavity.

According to Komissarov (1999*b*), low Poynting flux jets should not form prominent nose cones even if the magnetisation parameter is large. However, we see the most prominent nose cone in C1-10/3 where σ has a considerable lower value than in B1-10/3 or C2-10/3 which have the same $\overline{\beta}$.

Owing to the same inward directed Lorentz force that produces the nose cones the internal cross shocks are stronger in the toroidal field models than in the corresponding hydrodynamic jet models. In the poloidal field case, however, the effect is opposite: the magnetic field makes the jet less susceptible to shock waves driven into the beam perpendicular to the field lines as the magnetic pressure on the axis repels shock waves. While the cross shocks in hydrodynamic jets are produced mainly by shock waves driven into the beam from the outside (e.g. by eddies in the cavity), the cross shocks in the toroidal field cases are of different nature. They are created intrinsically by the inwards pointing magnetic stress such that even models with smooth cocoons like B1-1/20 show strong cross shocks. Still, in all models the mean magnetisation in the beam becomes negligible after the plasma has passed through the first recollimation shock (apart from B1-pol-1 where the beam remains almost completely unperturbed), such that even in the most strongly magnetised models, the field never reaches equipartition values in the cross shocks or in the hot spot. This has consequences for observations where equipartition is usually assumed for the magnetic field in the hotspot and other bright emission features of radio sources. However, there might be configurations of the magnetic field which lead equipartition values, although this hypothesis has to be tested by simulations combining poloidal and toroidal fields on different footings.

We should point out that the setup of the toroidal and the poloidal field models differs in more respects than the field direction alone. In the toroidal field models B^ϕ is injected together with the beam into a domain filled with a non-magnetised medium. In the poloidal case however, the grid is initially already filled with the same field strength that is injected with the beam. Hence, the poloidal field models are not only pressure matched in thermal pressure, but also total pressure matched, p^* being the same inside the beam and in the ambient medium. In contrast, the toroidal field models are over-pressured in p^* by a factor of $1 + \overline{\beta}$.

Another interesting result is the almost completely featureless cocoon in model B1-1/20. It seems that the low toroidal field strength in combination with the other parameters of the model suppresses the formation of shocks or eddies in the cocoon and thus keeps the beam undisturbed from external effects. The propagation efficiency becomes optimal and the collimation remains nearly perfect until the end of the simulation. Although this behaviour is not repeated in model C2-1/20 (and we

have not computed the model C1-1/20), it still implies that with the right combination of parameters, the morphology of jets can be influenced by magnetic fields of a strength far below equipartition.

Dynamics

The evolution of 2D jets can be divided into a 1D phase and a 2D phase. The models of the B1 series do not reach the 2D phase in our simulations. Their propagation velocity remains constant until the jets have reached the end of the computational domain. The C1 and C2 models, however, reach the 2D phase sufficiently early in our simulations. Especially in the C1 models, where the evolutionary times are very large, we can see the different phases clearly: the propagation velocities are constant and coincide with the estimated 1D velocity [Eq. (3.4)] up to $t \approx 50$, where the jets start to decelerate. The aspect ratios become nearly constant at about the same time (top panels of Fig. 3.21, all models but C1-10/3). A similar behaviour is observed for all C2 models. Model C1-10/3 is different, because its dynamics are completely dominated by the high density nose cone, thus its propagation is more ballistic and not influenced by 2D effects.

An interesting result is that the propagation velocity of most of the C1 and C2 models in the 1D phase of their evolution agrees very well with the 1D estimate. This implies that different morphologies of the working surfaces in the toroidal field models, or their p^* over–pressured beams, do not influence the propagation in the 1D phase. It would be interesting to simulate models with higher Poynting flux to find out whether this affects the 1D propagation. Models B1 all propagate faster than estimated by Eq. (3.4). This is a consequence of the reflecting boundary conditions, which we have used outside the nozzle and which in this case influence strongly the propagation of the jets.

4 Long Term Evolution of a Powerful Magnetised Jet

Simulations of the long term evolution of extragalactic jets can address many aspects of jet physics. One can study the influence of the ambient medium (e.g. model the galactic halo), plasma compositions, or the influence of magnetic fields. We are interested in the impact of equipartition magnetic fields on the long term evolution of powerful jets, particularly on the morphology and the dynamics of large scale jets and their cavities. In this regard we examine a different aspect than Scheck et al. (2002), whose main goal was to establish a link of the jets' dynamics and morphology with their plasma composition.

4.1 Simulation setup

For setting up long term simulations we have chosen the same parameters as Scheck et al. (2002) in their cold baryonic model. In this way we can compare with their results straightforwardly. The parameters used by Scheck et al. (2002) are such that the jet has a kinetic power of $L_{kin} = 10^{46}$ erg/sec and a 1D velocity (3.4) of $v^{1d} = 0.2c$. With an external density of $\rho_{ext} = 1.67 \times 10^{-27}$ g/cm^3 and a beam radius of $r_b = 0.366$ kpc these requirements yield the following parameters:

η	W_b	M_b	γ_b
10^{-3}	7.95	16.4	1.42

Using these parameters we have constructed two different models. Model LA0 is a hydrodynamic reference model with $\overline{\beta} = 0$. It should evolve similar to model BC of Scheck et al. (2002), the only difference being that we have set up the model as pressure matched with the ambient medium, while Scheck et al.'s model was slightly over pressured. Model LA1 is like LA0 but with a toroidal field of equipartition strength (i.e. $\overline{\beta} = 1$) added to the jet inflow. We have used the same profile of B^ϕ as in the short term simulations given by Eq. (3.1) with a magnetisation radius of $r_m = 0.6$. The resulting jet model has a very low Poynting flux with $\sigma = 5.199 \times 10^{-3}$. Since we have seen that the equipartition models in the short term simulations are strongly affected by the toroidal field (Cha. 3), we can expect a similar behaviour here. We have restricted the magnetic field to a purely toroidal component, because (1) toroidal magnetic fields affected the morphology and dynamics much more than poloidal magnetic fields in the parameter study of short term simulations, and (2)

the accuracy of our spatial interpolations methods is of higher order in the absence of poloidal fields allowing for a smaller grid resolution (see below). Please note that Scheck et al. (2002) have chosen the parameters such that the jet is comparable to a typical FR II radio galaxy like e.g. Cyg A.

The computational domain spans a region of $200r_b \times 500r_b$ (approximately 73.2 kpc $\times$ 183 kpc) covered by an equidistant grid of 2400 by 6000 zones. This yields a resolution of 12 zones/r_b, which is twice the resolution of Scheck et al. (2002). The boundary conditions and grid setup are the same as in the short term simulations, and are described in Sec. 3.1. For spatial interpolation we have used PPM which is of third order spatial accuracy in case of a purely toroidal field (see Sec. 2.3.3) thus allowing for the relatively small spatial resolution compared to the short runs, which used a PLM interpolation instead.

Each of the two simulations took about 600 hours on an IBM p690 Regatta node of 32 1300 MHz Power4 CPUs. The final evolutionary times of 6580 $r_b/c \approx 7.85 \times 10^6$ y (LA0) and 6780 $r_b/c \approx 8.09 \times 10^6$ y (LA1), respectively.. These times are still relatively short compared to the typical lifetime of a radio galaxy ($10^7 - 10^8$y), but are of the same order of magnitude. We will compare the results at the final time of model LA0.

4.2 Results

4.2.1 Morphology

Rest mass density and thermal pressure

In Fig. 4.1 we have plotted snapshots of the rest mass density of both models. Superposed are the tracer contours $f = 0.9$ and $f = 0.1$, in order to mark the beam and the cocoon. Despite its magnetisation, LA1 does not have a nose cone. Since all of the equipartition toroidal field models of the short term simulations develop a nose cone, this is surprising, but probably due to σ being more than five times smaller in model LA1 than in the short term models. In fact, the missing nose cone of the magnetic model makes the two density snapshots look very similar at first glance, but there are a number of differences which we would like to point out. Model LA1 has a smaller cocoon than model LA0: the $f = 0.1$ contour extends from 90 kpc to 130 kpc in z direction and up to 5 kpc in radial direction in model LA1, whereas in LA0 it ranges from 80 kpc to 135 kpc in z-direction and up to 7 kpc in radial direction. The remainder of the cavity has a much higher density, especially at the base of the jet, where the density is up to two orders of magnitude larger near the beam in model LA1 than that of model LA0. On average, the density of model LA1 is half an order of magnitude larger than that of model LA0 in the region the region $r < 15$ kpc and $z < 70$ kpc. In the same region, the density distribution of model LA0 is much less homogeneous than that of LA1, which exhibits less filaments and a smaller number of eddies. Moreover, the eddies in model LA1 are larger. Finally, a slight difference can be observed in the overall form of the bow shock, which is convex in LA0, while it is concave in the case of LA1 up to $z \approx 25$ kpc and from 80

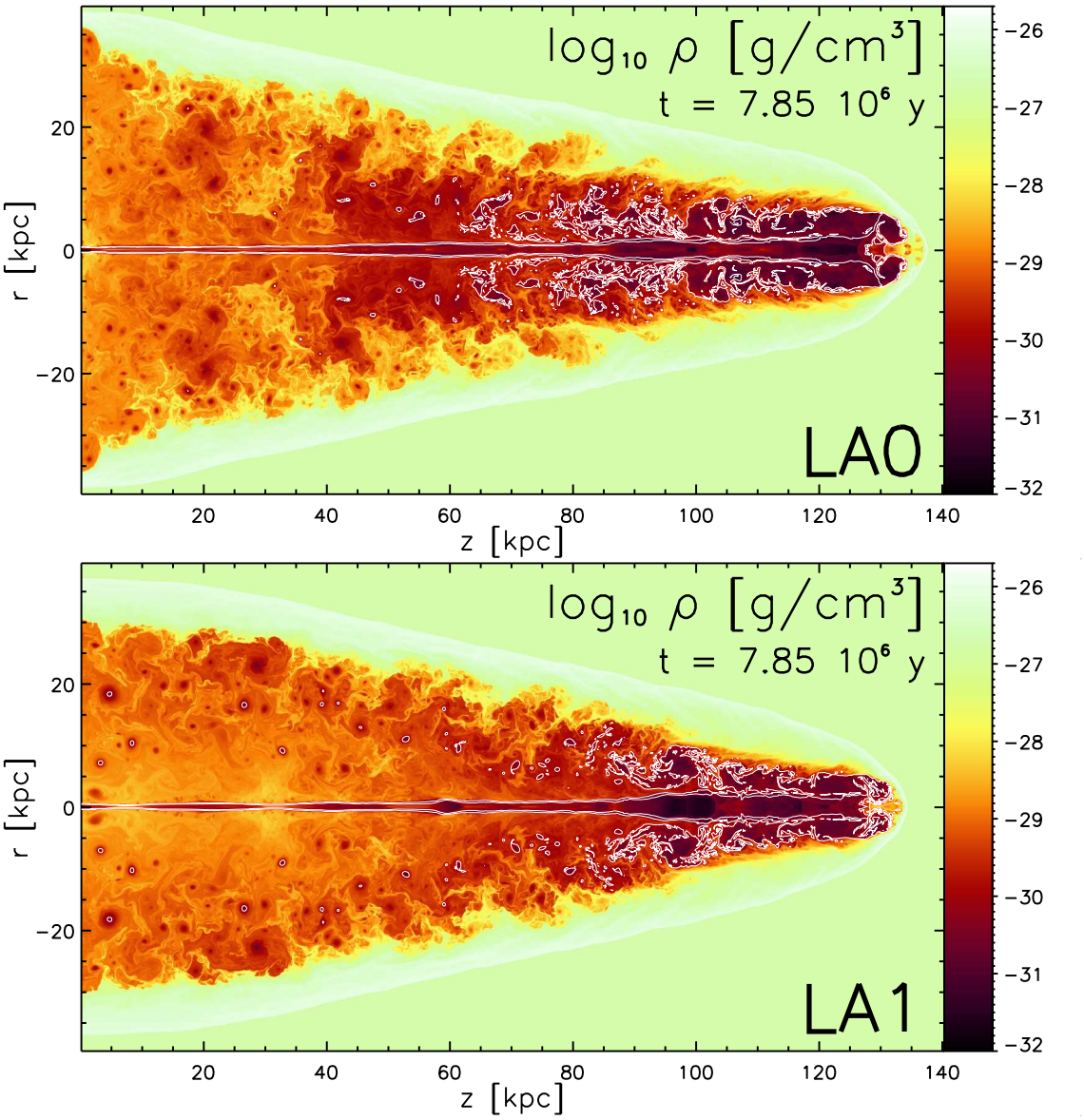

Figure 4.1: Rest mass density snapshots of the long term simulation models. Superposed are tracer contours with $f = 0.9$ (inner contour) and $f = 0.1$ (outer contour).

to 130 kpc and convex in between.

Another difference between the two models is visible in the tracer contours in Fig. 4.1. The beam of LA1 is pinched strongly at $z \approx 7$ kpc and $z \approx 32$ kpc, whereas the beam of LA0 is almost undisturbed in that region. In the top panel of Fig. 4.2 we have plotted the beam averaged rest mass density along the jet axis of models LA1 and LA0 in solid and dashed lines, respectively. The plots show that the density of model LA1 is disturbed much more by the cross shocks than that of model LA0; up to a distance of 100 kpc from the nozzle the maxima (minima) of the curve are half an order magnitude larger (smaller) in the magnetic model compared to the hydrodynamic one.

Snapshots of the thermal pressure distribution of both models are displayed in Fig. 4.3. Here the difference between the two models are less subtle than in the

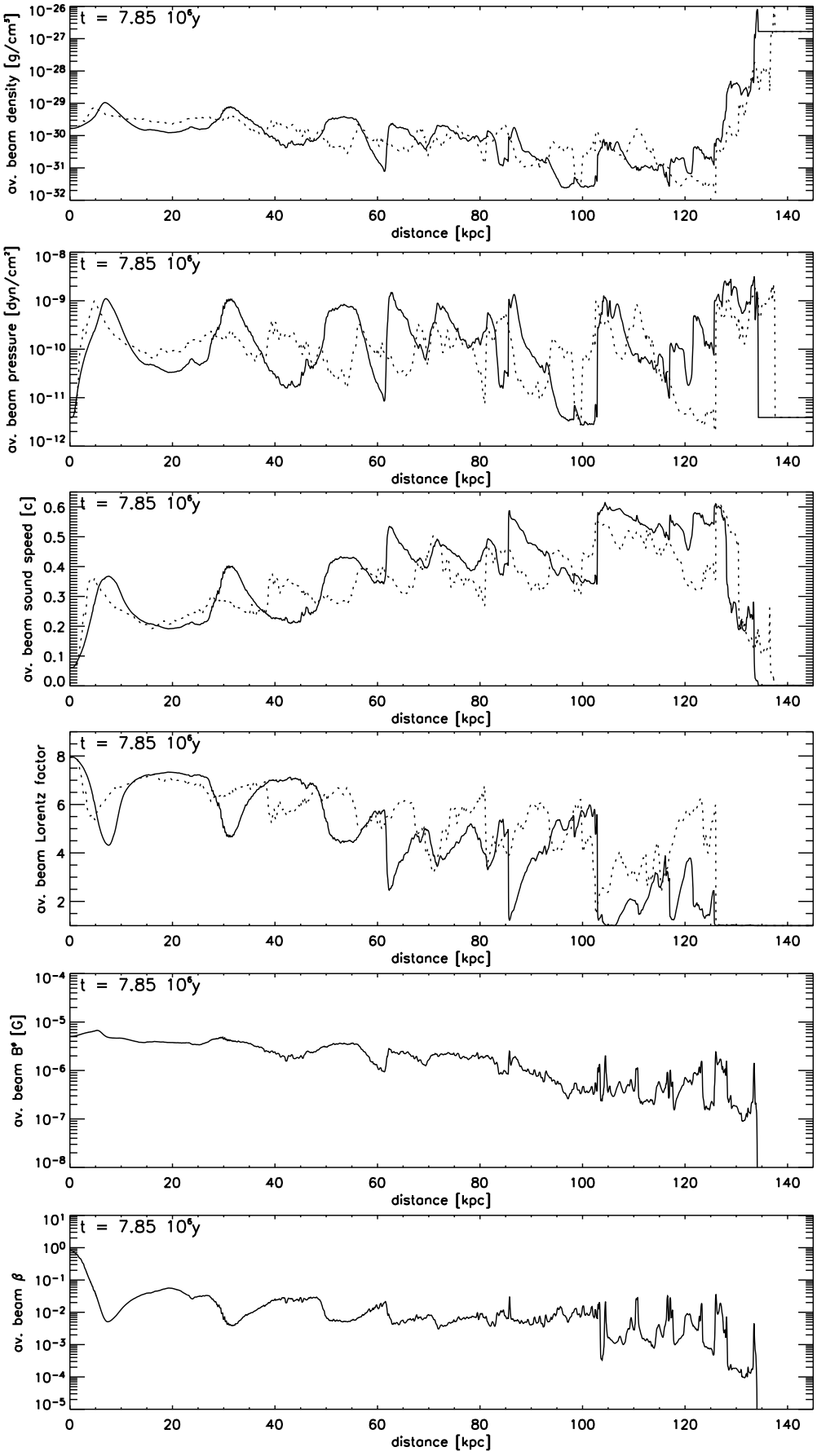

Figure 4.2: Various quantities averaged over the innermost 10 radial zones and plotted along the axis. The solid lines correspond to model LA1, and the dashed lines to model LA0.

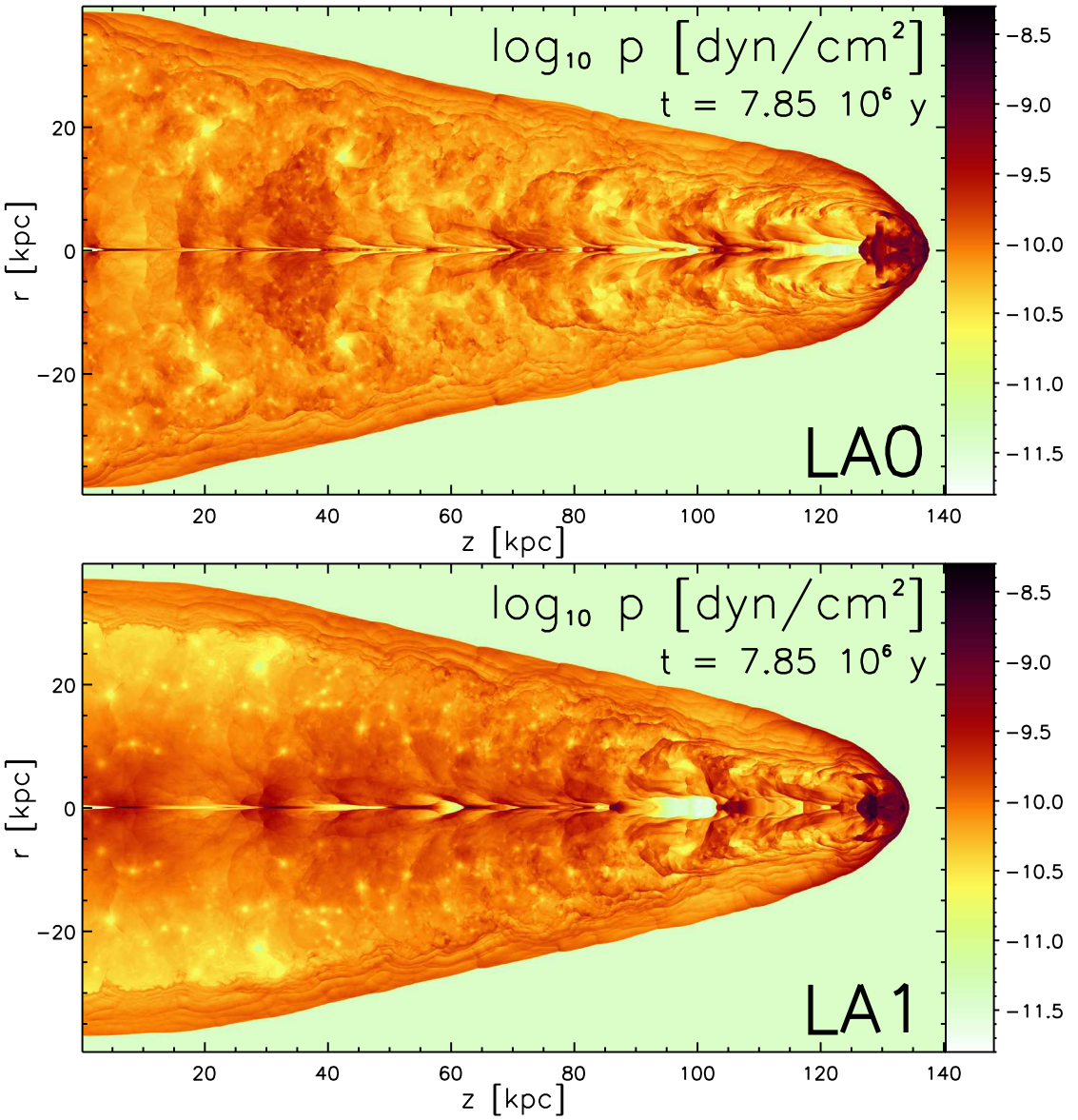

Figure 4.3: Thermal pressure snapshots of the longterm simulation models.

density distribution. The pressure image of LA0 shows a chain of cross shocks and rarefaction waves in the beam and an extended high pressure region in the hot spot. The cavity is turbulent streaked by many waves and eddies everywhere between beam and bow shock. The cavity pressure varies locally by one or two orders of magnitude, but on average it is the same everywhere outside the beam. The pressure distribution of LA1 is much different. Up to $z = 90$ kpc (i.e. the beginning of the cocoon, see above) the thermal pressure decreases with growing radial distance from the beam. Near the beam, roughly in a triangle spanned by the axis and the line connecting $(r, z) = (20, 0)$ and $(r, z) = (0, 90)$, the pressure is much higher than in the remainder of the cavity. In between that region and the shell of shocked ambient gas there is another distinct extended region (between $20 < r < 30$ kpc and $0 < z < 40$ kpc) of much lower pressure than anywhere else in the cavity. Both the high pressure and the low pressure region are much more homogeneous than the

turbulent cavity of model LA0 in the same regions. However, the pressure structure in the cocoon (between $z = 90$ kpc and the hot spot, see above) and in the shell is qualitatively the same as in the hydrodynamic model LA0.

In the beam, the pressure differences between shock and rarefaction waves are also much larger in model LA1 than in LA0, i.e. the cross shocks in the beam are much stronger in the magnetised model. One especially extended rarefaction wave marks the beginning of the cocoon. It is followed downstream by an extended region of high pressure starting with a planar shock ($z \approx 103$ kpc). The strength of the cross shocks on the axis is illustrated by the beam averaged pressure, displayed in the second panel of Fig. 4.2. The solid line, belonging to model LA1 has higher peaks and lower minima by nearly one order of magnitude compared to the dashed line (LA0).

Beam averaged values for the sound speed of both models are displayed in the third panel of Fig. 4.2. The stronger cross shocks in the beam of model LA1 make the plasma hotter, i.e. the sound speed is on average larger in the magnetised model. Especially in the region between 60 and 100 kpc we can see much higher peaks in the sound speed of model LA1 than in that of model LA0. From $z \approx 103$ kpc to the terminal Mach disk at $z \approx 125$ kpc the sound speed of model LA1 remains on a very high level, near to the possible maximum value of $0.648c$[1], i.e. the beam is very hot in that region. The behaviour is similar in LA0, but not as extreme.

Lorentz factor and velocity divergence

The two upper panels of Fig. 4.4 show snapshots of the Lorentz factor of both models. Superposed are velocity vectors. The differences between the two models are obvious. While the beam of model LA0 has bulk Lorentz factors larger than 5 up to the end of the beam, LA1 already decelerates to only mildly relativistic speeds 20 kpc closer to the nozzle. As described previously, the beam of model LA1 is disturbed much more than that of model LA0 already in the first cross shock, and consequently maintains the high initial Lorentz factor for a much shorter distance from the nozzle compared to model LA0.

The hydrodynamic model also shows a stronger and more extended back flow. While any significant back flow is confined to $z > 90$ kpc in model LA1, it reaches back to $z \approx 60$ kpc in the case of LA0. Furthermore, some areas of the back flow near the head of the jet reach relativistic speeds with Lorentz factors of $W \approx 2$ in model LA0. In LA1 this is not the case ($W \approx 1.3$).

The beam averaged Lorentz factor of both models is displayed in the fourth panel of Fig. 4.2. The plot shows once more, that the beam of the magnetised model (solid line) is influenced more strongly by cross shocks than that of the hydrodynamic model (dashed line). In particular near the head of the jet, the beam flow in model LA1 is nearly stopped ($z \approx 86$ kpc) or even completely stopped ($103 < z < 107$ kpc), while the flow of LA0's beam remains at least mildly relativistic until its termination

[1] In an ideal EOS, the sound speed (2.22) converges to maximum in the limit of infinite internal energy, i.e. $c_s \xrightarrow{\varepsilon \to \infty} \sqrt{\gamma - 1}c$. In our models $\gamma = 1.42$, therefore $c_s \to 0.648c$.

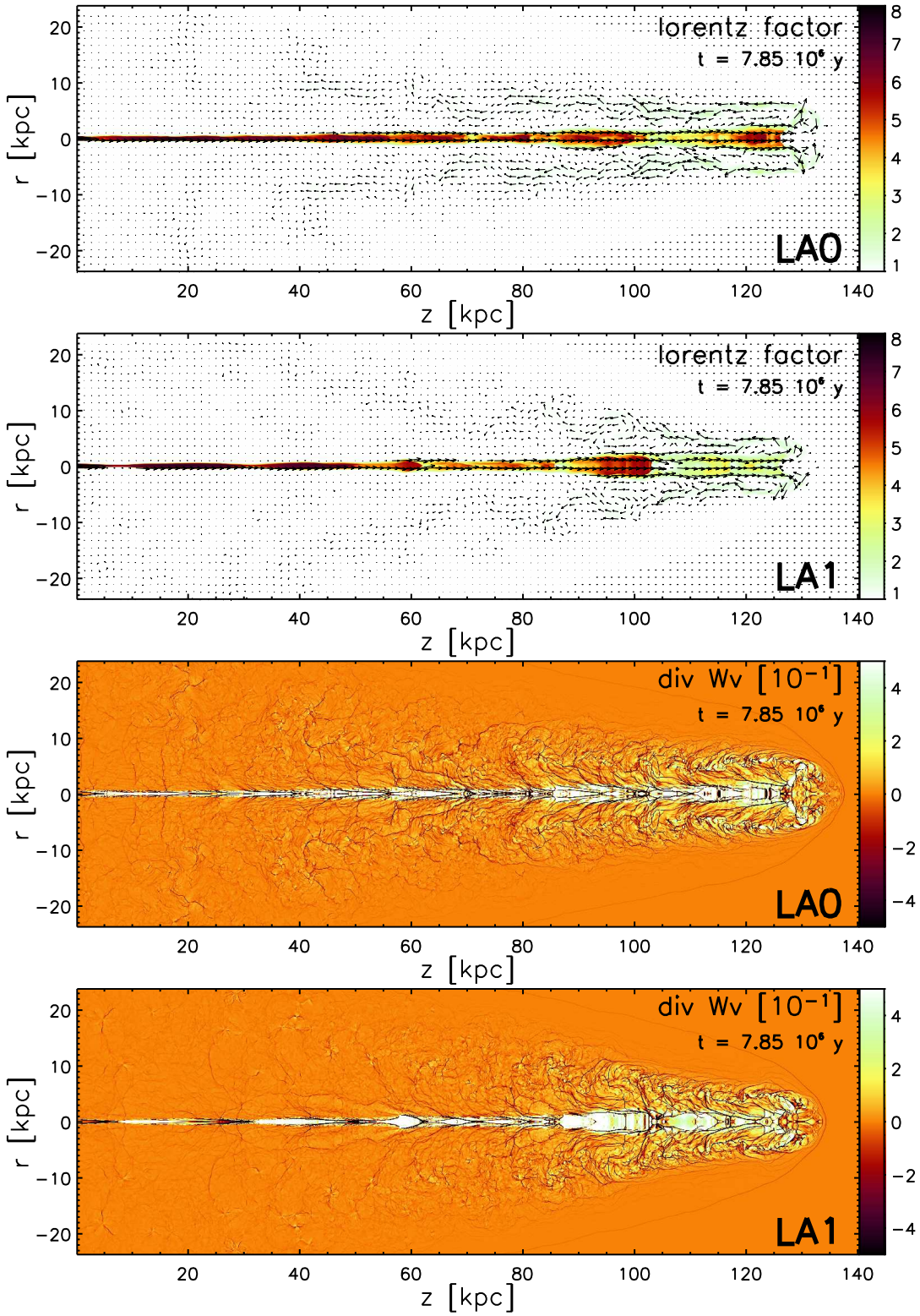

Figure 4.4: Snapshots of the Lorentz factor and of div($W\mathbf{v}$) of the long term simulation models.

point.

The two lower panels of Fig. 4.4 show snapshots of the relativistic velocity divergence, div($W\mathbf{v}$), of both models. In the snapshots, shock waves appear in dark as there the velocity divergence is negative, while rarefaction waves have a positive velocity divergence and appear in bright colours. Again we would like to point out that high p and ρ regions associated with the post-shock states and low p and ρ regions associated with the rarefaction waves in the beam are much more extended in the magnetised model than in the hydrodynamic one (cf. Figs. 4.1 and 4.3). At $z =$ 90 kpc the beam of LA1 is accelerated in a rarefaction region of 10 kpc length and 2 kpc radius. There it becomes more than five times wider and 27 times longer than the initial beam radius. The fact that the cavity of model LA1 is less turbulent than that of model LA0 is also reflected in the velocity divergence. Whereas model LA1 does not show many shocks for $z < 60$ kpc outside of the beam, model LA0 is streaked by shock waves everywhere in its cavity.

The magnetic field in model LA1

Snapshots of the toroidal magnetic field component (upper panel) and of the β parameter (lower panel) of model LA1 are displayed in Fig. 4.5. The magnetic field is especially high inside the beam, where it reaches values of slightly larger than the averaged injected $B^\phi \approx 4 \times 10^{-6}$ G in the two first cross shocks. The beam magnetic field, plotted in the fifth panel of Fig. 4.2, decreases slowly with distance from the nozzle but remains above 10^{-6} G up to $z \approx 90$, where it decreases by one order of magnitude remaining uniform on average until the end of the beam. Near the head of the jet, in the hotspot, B^ϕ increases again to values similar to the highest beam values (Fig. 4.5). From there it is transported backwards with the beam material and reaches a nearly constant value around 10^{-6} G in most parts of the cavity. In particular for $z < 60$ kpc, the magnetic field distribution is even more homogeneous than the thermal pressure distribution described above. A thin layer surrounding the beam only contains a very weak magnetic field.

Since the distribution of the magnetic field strength is so homogeneous in the greater part of the cavity, the image of β (Fig. 4.5, bottom panel) mostly reflects the distribution of the thermal pressure, which, as we have described above, varies radially in the cavity. β is very low for $r < 5$ kpc. It then increases with radius, and reaches values ≈ 1 only where the magnetic field accumulates at the reflecting $z = 0$ boundary, and where the pressure is low. The β distribution also demonstrates why LA1 does not develop a nose cone. In the short term simulations of equal initial magnetisation β grows to values larger than 1 near the terminal Mach disk (Cha. 3), and in particular in the plasma that flows away radially from the beam's termination point, which gives rise to the nose cone. In model LA1 this is not the case, β only reaches values of 0.3 or less near the terminal shock ($z \approx 125$ kpc). This might be explained by the lower Poynting flux of model LA1 (σ is at least five times lower in model LA1 than in all equipartition short term models).

The beam averaged β value plotted along the axis (bottom panel of Fig. 4.2) reveals that the initially high magnetisation of the beam decreases by more than two orders

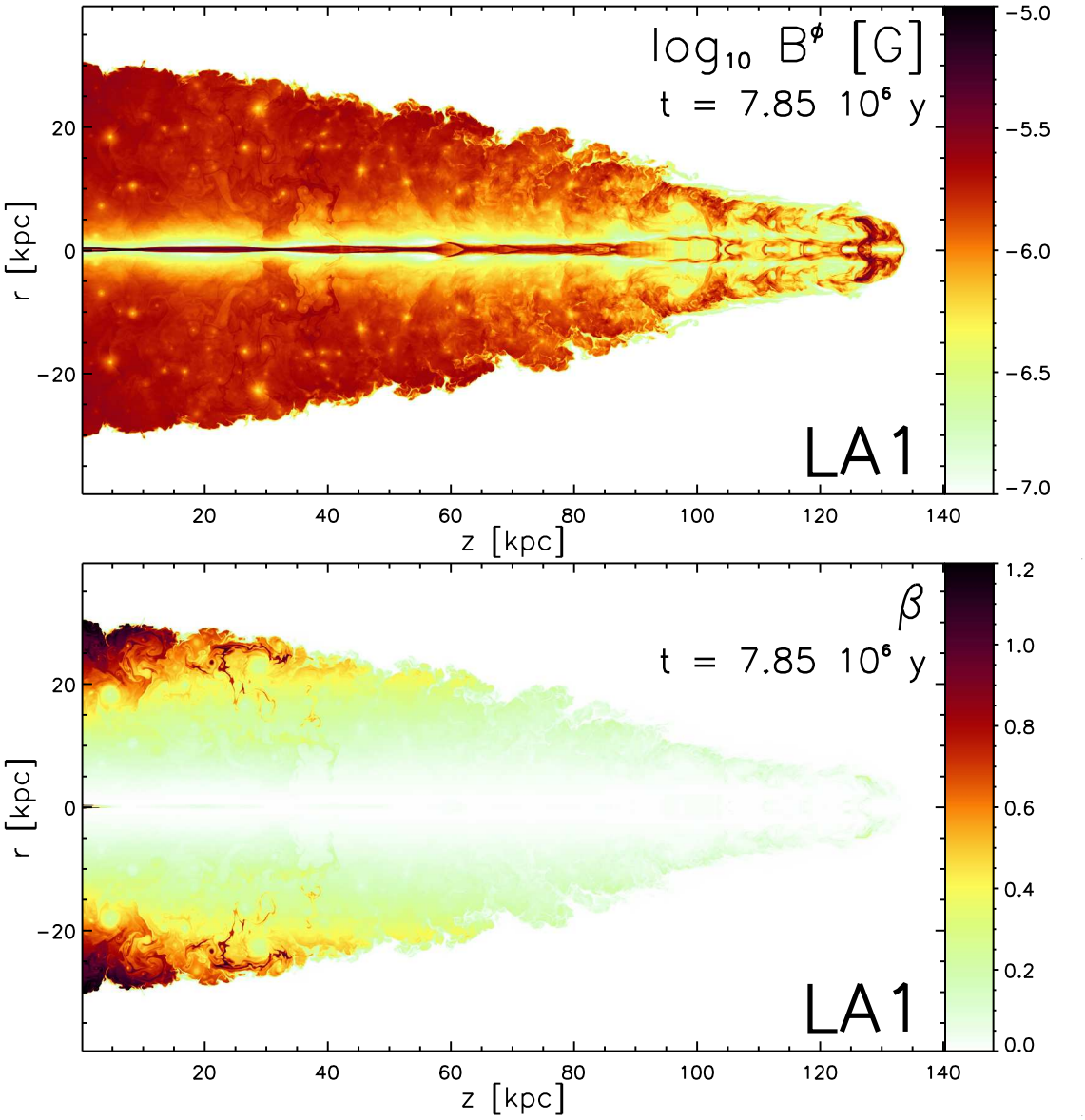

Figure 4.5: Snapshots of the logarithm of B^ϕ (upper panel) and of β (lower panel) of model LA1.

of magnitude in the first recollimation shock at $z = 7$ kpc, and afterwards remains at an average value of 10^{-2}, which is modulated by the beam's cross shocks. In these shocks the magnetisation can grow by more than a factor of 5. Close to the head of the jet β starts oscillating wildly, reaching a peak value of $\approx 5 \times 10^{-2}$ near the hotspot.

4.2.2 Temporal evolution

For studying the dynamics of the two long term models, we examine the evolution of various global quantities defined in Sec. 3.1.

Time evolution plots of the head position, l_c are shown in Fig. 4.6 (top panel). The

1D phase of the evolution lasts until $t \approx 5 \times 10^5$y, when the heads of both models reach $z \approx 20$ kpc. After that LA1 decelerates slightly more than LA0 until the distance between the head positions of the two models reaches a quasi constant state at $t \approx 3.5 \times 10^6$y. At later times the deceleration is minimal, and the propagation speed is nearly constant at $v \approx 0.04\ c$.

The differences in the evolution of the cylindrical aspect ratio, A_c, (middle panel of Fig. 4.6) are correlated with the differences in the propagation speed. The evolution can be divided into the same three phases (1) a rapid increase of the aspect ratio in the 1D phase until $t \approx 5 \times 10^5$y; (2) a slow increase of the aspect ratio until $t \approx 3.5 \times 10^6$y; and (3) a nearly self similar phase to the final times of the simulations with only a slight total increase. The aspect ratio of model LA1 remains lower than that of LA0 throughout the last two phases and reaches a maximum of 5, while model LA0 reaches $A_c \approx 5.3$.

The bottom panel of Fig. 4.6 shows the time evolution of the average thermal pressure in the cavity. For both models it follows an almost perfect power law distribution. Apart from the interval $3 \times 10^5 < t < 5 \times 10^5$y, the magnetised jet has slightly higher average pressure at any time of the simulation. Since initially both models begin with the same p, there is some transfer of toroidal field energy to the thermal energy, as in the short term simulation.

The hot spot thermal pressure of both models is displayed in the top panel of Fig. 4.7. No systematic trend dividing the two models can be observed. The evolution is such that the pressure in the hotspot remains approximately constant in the 1D phase of the simulations, and then decreases following, on average, some kind of power law until the final time is reached. The definition of the hotspot position via the beam mass fraction, f, leads to the oscillations seen in Fig. 4.7. However, a smoothing of the data does not yield any further insight.

Fig. 4.7 also includes plots of the average cavity magnetisation, β_c (middle panel), and the average cocoon magnetisation, β_{cc} (bottom panel), of model LA1. Note that the cavity includes the cocoon (Sec. 3.1 on page 57). Both curves show opposite trends. The magnetisation of the whole cavity increases from an initial value of $\beta_c \approx 0.04$ to $\beta_c \approx 0.095$ at $t \approx 10^6$ y, and then remains on that level for the last two million years. However, β_{cc} decreases rapidly from a value around 0.07 to 0.04 in the first two million years, then decreases slowly for another two million years, until it reaches a constant level of $\beta_{cc} \approx 0.03$ for the remaining four million years. This is interesting, because neither of the two quantities seems to follow the evolutionary phases exhibited by all other quantities. In addition, the magnetisation of the whole cavity is an order of magnitude larger than that of the beam at the final time of the simulation (cf. Fig. 4.2, bottom panel).

4.3 Discussion

The results of models LA1 and LA0 are remarkably similar. This is unexpected as the short term simulations of equipartition toroidal field and corresponding hydrodynamic models have shown considerable differences in morphology and dynamics

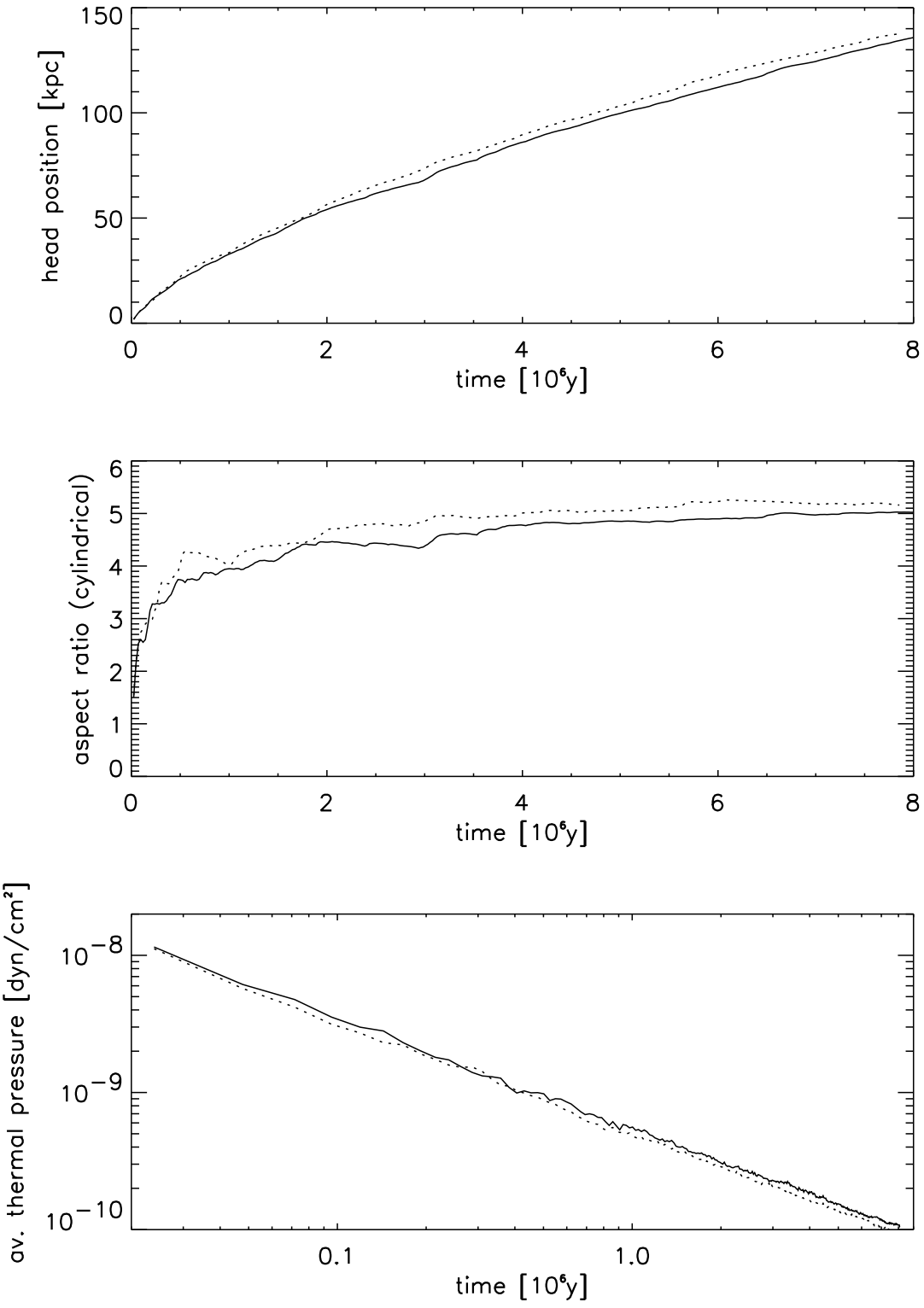

Figure 4.6: Head position, aspect ratio and average cavity pressure plotted against time. The solid lines correspond to model LA1, and the dashed lines to model LA0.

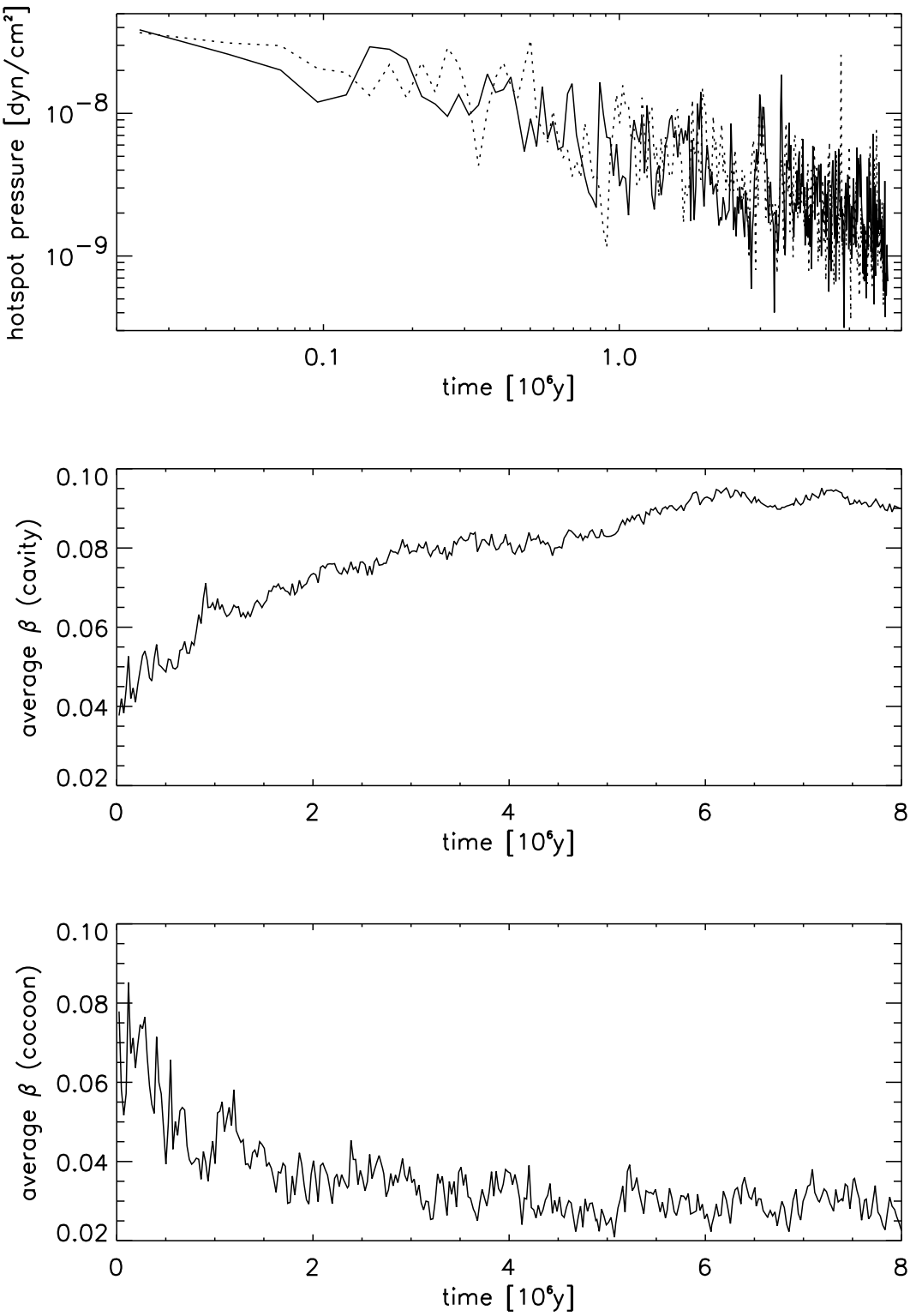

Figure 4.7: Hot spot pressure, average cavity β and average cocoon β plotted against time. The solid lines correspond to model LA1 and the dashed line to model LA0.

(Sec. 3.6). The relatively small differences between both models are due to the small value of the Poynting flux in contrast to the mass flux ($\sigma \sim 5 \times 10^{-3}$). That is the reason why fixing the kinetic power and speed of the jet determines the overall evolution, whereas the physical differences in the beam do not have a large influence. This behaviour has also been observed by Scheck et al. (2002) who simulated three jet models with varying plasma compositions. However, we find that the models differ substantially in the internal morphology of the cavity and of the beam.

4.3.1 Comparison with previous simulations

Since our long term evolution simulations use nearly the same parameters as those of Scheck et al. (2002), we compare our results with their baryonic cold (BC) model. Their simulations were performed with a grid resolution of 6 zones/r_b using the code of Martí et al. (1997), i.e. they used a similar method, but only half of our grid resolution. The main difference is that Scheck et al. (2002) use an equation of state with varying adiabatic index including protons, electrons and positrons (Synge, 1957, see also the appendix of Komissarov & Falle, 1998) whereas we use an ideal equation of state. The overall morphology of both our models and their BC model is very similar. However, some quantities show a different behaviour. The 1D evolution phase ends at $t \approx 5 \times 10^5$y in our models compared to $t \approx 10^5$y in their BC model. Their model has an aspect ratio of ≈ 4 at their final simulation time of 6×10^6y, whereas our models reach a maximum of 5.3. In addition, our models propagate slightly faster, reaching a length of 120 kpc (LA1) or 125 kpc (LA0) at $t \approx 6.3 \times\ 10^6$y when their BC model has a length of 110 kpc.

A simple theory for the evolution of the jet cavity was introduced by Begelman & Cioffi (1989). Scheck et al. (2002) have found that the evolution of their models follows an extended version of this theory, the extended Begelman-Cioffi (eBC) model. In this model the evolution of the head position, l_c, the average cavity pressure, P_c, and the aspect ratio, A_c, ban be described by the power laws

$$l_c \propto t^{1+\alpha}, \quad P_c \propto t^{-1-\frac{\alpha}{2}}, \text{and} \quad A_c \propto t^{\frac{1}{2}+\frac{5\alpha}{4}}\ , \tag{4.1}$$

respectively. Since the magnetisation of the matter in model LA1 is at least one order of magnitude below equipartition almost everywhere in the cavity (see Fig. 4.5), we can neglect the effects of the magnetic field pressure, and apply the same theory to both our jets. In exactly the same way as Scheck et al. (2002) did, we have extracted the index α by fitting the head position, l_c, as a function of time with a power law, separately in the 1D and the 2D epochs. We have also fitted P_c and A_c with power laws to compare the exponents with the ones predicted by the eBC model, P_c^{eBC} and A_c^{eBC}, using the value of α from the fit to l_c. The results are listed in Table 4.1. In the 1D phase the values are considerably different from those of Scheck et al. (2002), possibly because it lasts longer in our case. The exponents themselves are within 20% of those predicted by the eBC model in the 1D phase, and within 10% in the 2D phase. A self-similar growth of the cavity requires that the aspect ratio does not change with time. According to (4.1) this implies $\alpha = -0.4$. The fitted values of α are $\sim 30\%$ smaller, i.e. our models are not self-similar yet. However, the trend is that $\alpha \to -0.4$ at larger evolutionary times, e.g. extracting α from the fit of the

cavity pressure in the second part of the 2D phase yields a value of -0.405 for model LA0. Comparing with the numbers in Scheck et al. (2002) we see that our models are less self-similar than their BC model because our values of α are smaller.

4.3.2 Influence of the magnetic field on the long term evolution

The toroidal magnetic field of initially equipartition strength in model LA1 does not greatly influence the evolution of the jet. It only leads to slightly lower propagation speeds and aspect ratios (Fig. 4.6), the differences being less than 10%. Given that the LA1 beam has a total pressure, p^*, which is twice as large as that of LA0, this is unexpected. In fact, we expected a much larger difference owing to the results of the short term simulations. However, the differences in the internal structure of the cavity and the beam are substantial.

Similar to the short term models, the toroidal magnetic field in model LA1 leads to a different density and pressure distribution in the beam and in the cavity compared to model LA0. This can be explained by the Lorentz force which is directed radially inwards in side the beam, leading to larger pressure differences between the cross shocks and the rarefaction waves. The more violent shock pattern in the beam of LA1 leads to a deceleration of the flow, explaining the lower beam Lorentz factors (Fig. 4.4). In turn, this leads to a less violent back flow of beam material. Consequently, the cocoon is smaller in model LA1 than in LA0. The cavity, however, is not smaller in LA1, since the Lorentz force acting on the back flowing beam plasma is directed radially outwards, and hence adds to the sidewards expansion of the cavity. The magnetic field assumes values of 10μG in the cross shocks on the axis and in the hot spot. The jet remains super-Alfvénic everywhere with a maximum Alfvén speed of $c_A = 0.35c$ in the hot spot.

The second major effect of the magnetic field is that it suppresses eddies and shock waves in the part of the cavity up to $z < 60$ kpc. There the magnetic field is very homogeneous, assuming values near 1μG. The Alfvén speed in that part of the cavity is uniform ($c_A \approx 0.1c$) as is the sound speed ($c_s \approx 0.03c$). The matter is also sub-Alfvénic in that part of the cavity, which helps to suppress instabilities there. Moreover, the Lorentz force either enlarges or contracts eddies, depending on the direction of rotation of the eddies. This explains why there are only very large or

Table 4.1: Exponents of the eBC model. The values of α are extracted from fits to l_c according to Eq. (4.1). Columns P_c and A_c contain the exponents of fits to $P_c \propto t^\beta$ and $P_c \propto t^\gamma$, respectively. The values in columns P_c^{eBC} and A_c^{eBC} are the same exponents calculated using α and Eq. (4.1).

Phase	Model	α	P_c	P_c^{eBC}	A_c	A_c^{eBC}
1D	LA0	-0.215	-0.821	-0.893	0.274	0.231
	LA1	-0.189	-0.825	-0.906	0.303	0.264
2D	LA0	-0.323	-0.799	-0.839	0.107	0.096
	LA1	-0.315	-0.785	-0.843	0.120	0.106

very small eddies in LA1 compared to those in LA0 (Fig. 4.1). Once the eddies get too large, they are destroyed. When they are too small, they are dissolved my numerical viscosity. Given the large evolutionary age of the cavity (the width of the cavity at the base of the jet is 3 times the sound crossing distance and 10 times the Alfvén wave crossing distance at the end of the simulation), many eddies are dissolved already. Owing to that reasoning the cavity of model LA0 shows much more turbulence than that of LA1.

LA1 does not develop a nose cone at any time during its evolution. The jet models in the short term simulations (Cha 3), which have the same magnetisation all develop nose cones, because the magnetisation parameter, β, is larger than unity around their terminal Mach disks. Consequently, the Lorentz force is larger than the thermal pressure force and, thus, the geometrical source term of the radial momentum (2.31) becomes negative. Matter is forced into the nose cone instead of flowing backwards into the cocoon. The reason for β being so small in the head of LA1 is the small value of σ at injection.

4.3.3 Comparison with observations

The results of model LA1 at the final time of the simulation can be compared with observations of FR II radio galaxies. Observers usually assume equipartition between magnetic and thermal energy density in the hotspots of powerful radio galaxies. Therefore, absolute numbers are given in equipartition values. We find that the magnetic field is far from equipartition in the hotspot, the cocoon and most part of the cavity. Values of 10μG ($\beta \approx 0.01 - 0.05$) are found in the beam and the hotspot, and values from 0.1μG to 1μG in the cavity, where β ranges from 0.001 to 1. These fields are much smaller than the equipartition values of 1000μG (hotspot and jet) and 10μG (lobe) obtained for young powerful radio galaxies (Ferrari, 1998). Compared to Cyg A, our values agree reasonably well (Carilli et al., 1996). More recent observations using the Chandra X-ray observatory constrain the β value in the hot spots of 3C 280 and 3C 254 to 0.2-0.3 (Donahue et al., 2003) and to 0.04-0.1 in 3C 351 (Hardcastle et al., 2002). The values found in our simulation are smaller ($\beta \approx 0.03$), but agree within one order of magnitude.

In our simulation the magnetisation in the hotspot is much smaller than assumed in many observations (e.g. Hardcastle et al., 1998, assume equipartition values). Most probably, in order to obtain equipartition magnetic fields in the hot spots, the initial magnetisation of the beam must be much larger than in our models. Even in the short term models with $\overline{\beta} = 10/3$ the magnetisation in the beam decreases by two orders of magnitude in the first recollimation shock. In addition, a combination of poloidal and toroidal fields might help to conserve the initial beam magnetisation, since axial fields would remain in the beam (e.g. model B1-pol-1, Cha. 3) confined by the toroidal field.

The hot spot pressure of $\approx 2 \times 10^9$ dyn/cm^2 found in our models is within a factor of 1.5 of that deduced for Cyg A, while the average jet pressure of 2.4×10^{-10} dyn/cm^2 agrees even better with the Cyg A value of 3×10^{-10} dyn/cm^2 (Carilli et al., 1996). The propagation velocity of ≈ 0.05c in the 2D phase is in good agreement with the

estimates by Daly (1995).

Hydrodynamic properties of jets can only indirectly be inferred from observations. Yet, we can compare our simulated jets with observations by computing the non-thermal synchrotron emission for model LA1. Previous, hydrodynamic long term simulations (Scheck et al., 2002; Komissarov & Falle, 1998) had to make assumptions about the magnetic field strength and structure, because the magnetic field was not included in these simulations. However, our simulations do not include the evolution of the non-thermal matter content of extragalactic jets. We assume that this non-thermal population of particles is coupled to the thermal plasma (the one we simulate) through the magnetic field. In a first approach, we have computed radio maps according to the method used by Scheck et al. (2002). This approach assumes an electron energy distribution by taking the energy density of the non-thermal particles to be proportional to the beam mass fraction. The energy of these particles is distributed according to a power law. To calculate the emission of the complete galaxy including both jet and counter jet, we have exploited the symmetry properties of our models. However, the results are unrealistic, as the large magnetic field in the cavity (compared to that of the cocoon) leads to images without radio lobes at all viewing angles (surface brightness, S, given in arbitrary units for three viewing angles in Fig. 4.8). Instead, these images look more like X-ray images of radio galaxies. This failure led us to consider a second model for the distribution of non-thermal particles, both inside the beam and inside the cavity.

In this second approach, we assume two non-thermal electron distributions: (1) a diffuse part, whose energy distribution, normalised with the square of the beam mass fraction, is distributed among the emitting non-thermal particles according to a power law $N(E) \propto E^{-\sigma}$ with cutoffs at the maximum and minimum energies for the non-thermal population (similar to model type-E in Mimica et al., 2004), and (2) a second population of electrons which takes into account acceleration by local shocks by scaling the cutoff energy densities with the velocity divergence and the pressure (similar to model type-N in Mimica et al., 2004). The resulting surface brightness images are displayed in Fig. 4.9 (S_2, in arbitrary units) for viewing angles of 10, 45 and 80 degrees. The resolution of the images is much larger than that of actual observations, because in that case the data is convolved with the instrumental beam resolution. This explains why we see such narrow and well defined profiles in the synthetic radio images. The two main features known from observations of powerful radio galaxies are present in all three images: radio lobes with hotspots and bright, knotty jets. Focussing on the image of 45 degrees viewing angle we can see a one–sided jet and two hotspots and radio lobes much like those seen in the image Cyg A in Fig. 4.10. Moreover, the brightness ratios of hotspot to lobe of the approaching jet of S_2(45 degrees) and Cyg A are of the same order of magnitude. However, the ratio of the beam's width to the lobe width is too large compared with that of a prototypical FR II source. This might be the case, because our model has not yet reached the final evolutionary time of $10^7 - 10^8$y of a typical FR II source, or, because of the assumed axisymmetry of our simulation. In our results the cocoon emission from the counter jets is slightly brighter than that of the approaching jet. This follows from the relatively high speed of the back flow material, which enhances the emission from the counter jet lobe through Doppler boosting, while dimming

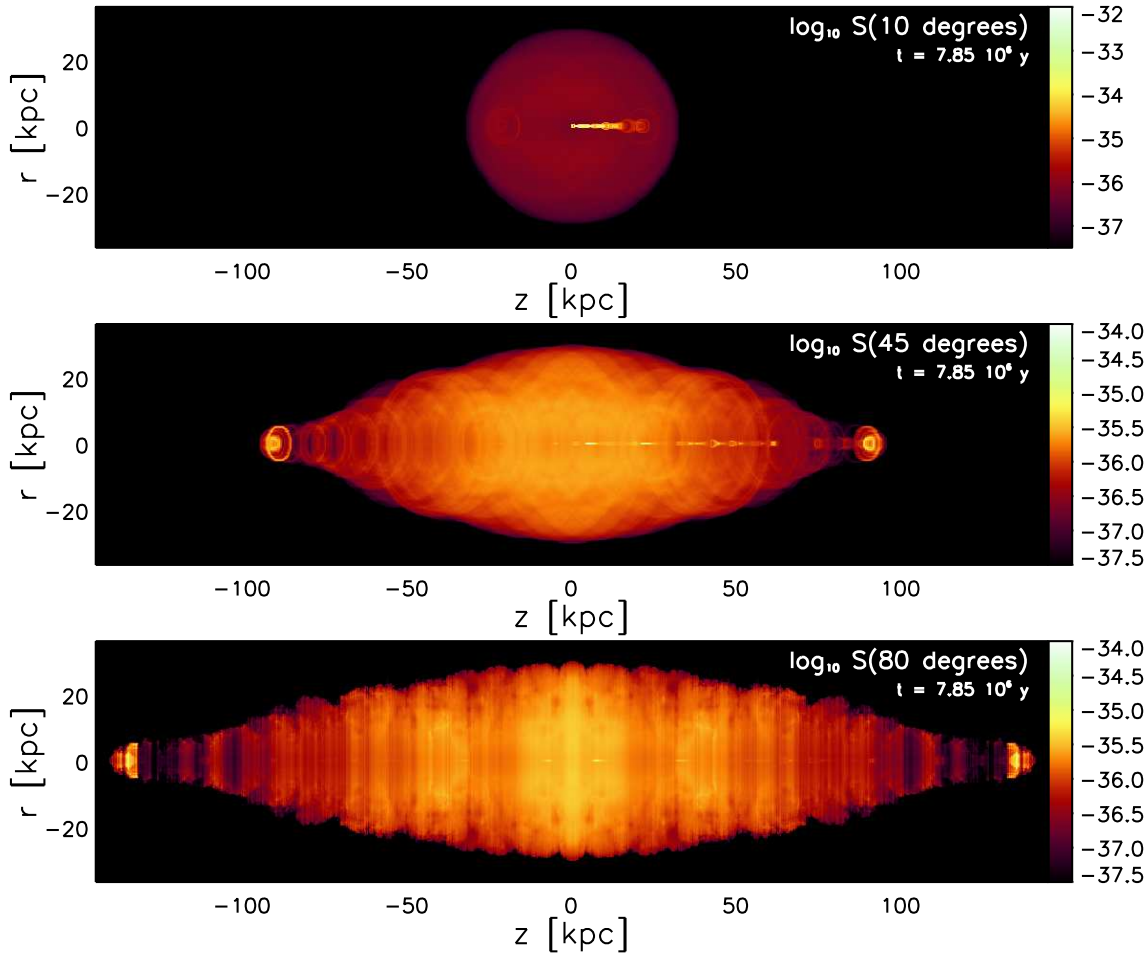

Figure 4.8: Simulated radio maps for model LA1 using one electron population. The surface brightness is given in arbitrary units, with viewing angles of 10, 45 and 80 degrees, respectively (from top to bottom).

the lobe emission of the approaching jet. In real sources this is not observed, i.e. back flow with relativistic speeds is not supported by observations. However, the large back flow velocities may be caused only by the axisymmetry imposed on our model. 3D relativistic simulations predict much more moderate values of the back flow velocity (Aloy et al., 2000).

4.3.4 Limitations

Our simulations are restricted to 2D axisymmetric flows, i.e. we force the jet to propagate along the symmetry axis. This is a considerable drawback, because the head of the jet cannot wobble around, which would change the effective head area, and thus the morphology of the cocoon and the hotspot. Specifically, the aspect ratio of axisymmetric jets is larger than that of 2D Cartesian simulations without imposed symmetry (Komissarov & Falle, 2003). In three dimensions, the wobbling of the jet's head may lead to different scenarios: (a) the effective area grows, leading to a faster deceleration (*dentist drill effect*, Cox et al., 1991), or (b) the wobbling

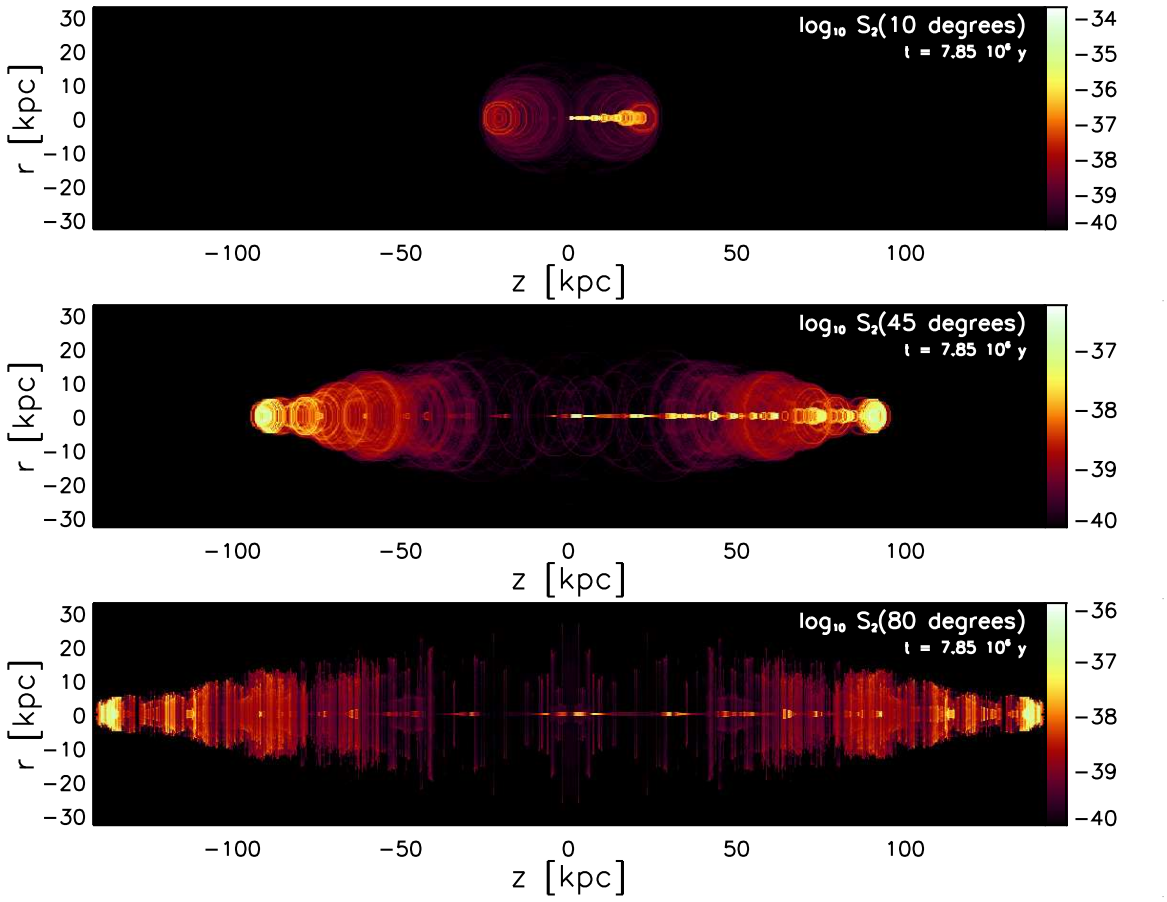

Figure 4.9: Simulated radio maps for model LA1 using two electron populations. The surface brightness is given in arbitrary units, with viewing angles of 10, 45 and 80 degrees, respectively (from top to bottom).

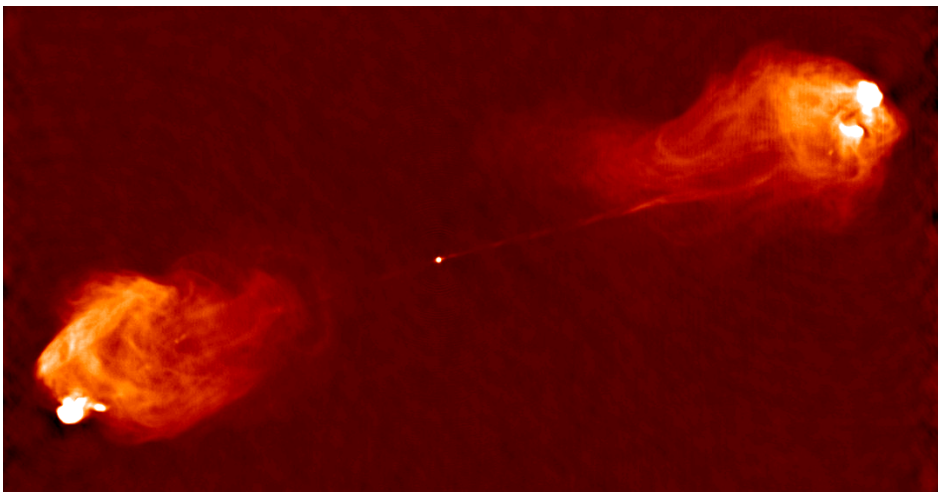

Figure 4.10: Radio image of the FR II radio galaxy Cygnus A (taken from the web page of the *National Radio Astronomy Observatory*, `http://www.nrao.edu`).

Mach disk reduces the cross sectional area of the jet, leading to acceleration (Aloy et al., 2000). Thus, three dimensional simulations are required to clarify this issue.

The grid resolution of twelve zones per beam radius at the injection nozzle is too small to account properly for mass entrainment and mixing. However, it is twice as large as in Scheck et al., 2002, leading to a more accurate description of the gross morphology and dynamics of the cocoon. On the other hand, the beam cross section grows with distance from the nozzle. Thus, the effective resolution is $\sim 20/r_b$ for $z > 50$ kpc. Comparison with the short term simulations (see Cha. 3) shows that a larger resolution does not necessarily lead to different morphologies. Furthermore, the required computational time is proportional to $(\text{zones}/r_b)^3$, i.e. doubling the resolution to $(24/r_b)$ would require 4600 instead of 600 hours of computing time to reach $t_{\text{end}} = 8 \times 10^6$y on the same IBM p690 Regatta computer node with 32 processors. Translated into turnaround time, this means that a simulation would require 24 months, which is far beyond the scope of a PhD project. This also means that long term simulations of RMHD jets in 3D with a similar resolution will either require much faster computers or multi-node parallel codes.

The ambient medium was uniform and non-magnetised. This is not entirely realistic, because extragalactic jets on kiloparsec scales will propagate into a stratified intra-cluster medium. Both pressure and density will decrease with distance from the galactic nucleus. A declining density atmosphere will cause a widening of the jet and might lead to considerable deceleration (Hooda et al., 1994). The galactic nucleus might also be moving with respect to the atmosphere, causing further deformation of the jet (Loken et al., 1995). Moreover, the intra-cluster medium will contain a diffuse magnetic field. This might lead to additional deceleration and bending of the jet (Koide, 1997). The number of parameters involved in modelling such an atmosphere is very large, i.e. many runs have to be performed (a parameter study is required).

In 2D axisymmetry the toroidal field cannot reverse its direction, i.e. it remains positive everywhere on the grid, if it is so initially. A reversal is only possible in 3D in combination with poloidal field components. In addition, poloidal fields may influence the magnetisation of the beam plasma and of the hot spot (see above). However, a full interplay between poloidal and toroidal field components would again require three dimensional simulations. In 2D the toroidal field will merely act as an additional pressure term on the poloidal fields.

5 Summary and Conclusions

In the past decade, time dependent numerical simulations have been used extensively to study the hydrodynamic properties of relativistic extragalactic jets. Simulations have proved to be very successful tools for understanding their morphology and dynamics, when compared to observations. Already in two dimensional, axisymmetric simulations most of the key features of large scale jets can be found. However, magnetic fields are considered to play a crucial role in the creation, collimation and propagation of jets. While our current understanding is that the formation of jets depends on magnetic fields, their large scale collimation over several hundred kiloparsecs probably requires magnetic confinement. The synchrotron radiation observed in these galaxies relies on the presence of magnetic fields in the emitting plasma, too, even where it is dynamically negligible. Therefore, relativistic magnetohydrodynamic (RMHD) simulations are required for an adequate treatment of large scale extragalactic jets.

It was the aim of this work to examine the properties of extragalactic radio jets by means of RMHD simulations in two spatial dimensions. To this end, we have developed a simulation code that solves the equations of ideal RMHD in conservation form. It is based upon an existing high-resolution, shock-capturing relativistic hydrodynamics code. Numerical fluxes are computed with an approximate Riemann solver which does not require a full spectral decomposition of the RMHD system of equations. Instead, we use an analytic estimate as upper (lower) bound for the largest (smallest) eigenvalue of the system. We developed this method to avoid the numerical instabilities, which arise from the degeneracies of the RMHD eigensystem. The magnetic field components are updated in time following a second order accurate constraint transport method which keeps the code divergence free. We have demonstrated that the code properly solves a full suite of one and two dimensional test problems and is at least competitive when compared to other RMHD codes published in the past years.

Summary of the results

Using this new tool, we performed a parameter study based on 14 two dimensional axisymmetric jet models, varying the strength and configuration of the magnetic field, the beam Lorentz factor and adiabatic index of the gas. We have found that the effects of toroidal magnetic fields on the morphology and dynamics of the jets are multifarious. With growing toroidal field strength jets develop strongly magnetised nose cones which have high density and pressure. They are created when magnetised beam plasma deflected at the terminal Mach disk of the beam is

driven in forward direction by the Lorentz force instead of flowing backwards into the cocoon. During that process, the beam plasma is mixed with higher density material from the ambient medium. Upstream of the nose cone, the beam material gathers in a bubble like structure, which is confined by a shell of large magnetisation. If the nose cone has grown to a size of $\sim 40\%$ of the total jet length, the jet becomes ballistic and propagates much faster than those with a smaller or without any nose cone. Apart from that, we have not found a simple trend connecting the strength or configuration of the magnetic field with propagation speed. Toroidal field jets also suffer from deceleration of their beam through strong oblique shocks enhanced by the inwards directed Lorentz force. Thus, the bulk Lorentz factor in the beams of toroidal field jet models is much smaller than that of non-magnetised or poloidal field jets. The opposite is observed in poloidal field jets. The oblique shocks are weaker than in the purely hydrodynamic jets, and the beam retains high bulk Lorentz factors up to its termination point. Even a toroidal field of a strength 20 times below equipartition can already have a large effect on the properties of a jet. In one of the jet models, the small magnetic field suppresses turbulent structures in the cavity, thus keeping the beam undisturbed from external influences and increasing the propagation efficiency of the jet. In all toroidal field jets we have found that the magnetisation in the beam becomes negligible (two orders of magnitude below equipartition) after the beam has passed through the first oblique shock. This has consequences for observations where it is usually assumed that the magnetic field energy density is in equipartition with the thermal energy density of the plasma in the hot spot and other bright emission features of the jet. Poloidal fields are almost completely expelled from the cavity of the jet, and the magnetic field accumulates in the high pressure region near the bow shock. In side the beam and in the hot spot the poloidal field retains its initial values, but the magnetisation decreases similarly to the toroidal field cases in two out of our three poloidal field jet models.

To study the influence of the magnetic field on the morphology and dynamics of a powerful radio jet, we have performed the first long term evolution simulation of a RMHD jet with toroidal field together with a reference simulation of a purely hydrodynamic jet of the same length. The simulations extend up to an evolutionary age of 8×10^6y, which is only a few times smaller than the typical age of a powerful radio source. The differences between both models in overall morphology and dynamics are surprisingly small. After an initial fast propagation epoch, both jets inflate their cavities in an almost self-similar manner, which is in good agreement with a simple theoretical model for the cocoon inflation (Scheck et al., 2002). The aspect ratios of both jets are practically constant during the last four million years of their evolution, but the average cavity pressure decreases according to a simple power law. The propagation velocities are almost equal, the reference model being approximately 2.5% faster than the magnetised one. Although the magnetised jet does not develop a nose cone, the toroidal field has a large impact on the internal structures of its beam and its cavity. The bulk Lorentz factor of the beam plasma is considerably smaller than in the hydrodynamic reference model. This is caused by stronger oblique shocks present inside the beam, which are induced by the inwards directed Lorentz force. The same force is also responsible for the less turbulent cavity of the magnetised jet. The Lorentz force either contracts or expands turbulent eddies, thus

dissolving most of them with time. In addition to being less turbulent, pressure and density decrease with radial distance from the axis. At large radii they are much larger in the magnetised jet than in the reference model. The magnetic field itself is almost completely uniform inside the cavity. The field strength is about 1μG, which is only a few times less than the initial value injected with the beam. The hot spot pressure, the propagation speed and the magnetic fields found in our simulation agree very well with those observed in powerful radio jets. Yet, the magnetisation of the plasma in the hot spot and inside the beam of our model is one to two orders of magnitude smaller than that reported by observers. For a further comparison with observations we have computed synthetic radio maps from our model. The maps exhibit two of the most prominent features found in observations of powerful radio galaxies: (1) bright, knotty jets and (2) hot spots surrounded by extended lobes of diffuse emission. Depending on the viewing angle and the model of the synchrotron emitting plasma, the synthetic images are in good agreement with observed images of the powerful radio galaxy Cygnus A. The differences between our radio maps and the observations are probably caused by assuming axisymmetry in our simulations. The ratio of the width of the beam and the radio lobes is too large, as is the amount of emission from the lobe of the counter jet.

Outlook

Our results demonstrate that the step from purely hydrodynamic to RMHD simulations leads to a large number of effects, not all of which we can fully understand by the simulations presented here. The most prominent effect of toroidal magnetic fields on the large scale structure of jets is the generation of nose cones. We have found that the ratio of Poynting and mass flux could be the decisive parameter determining whether models develop nose cones. Although nose cones where also found in Newtonian MHD simulations, this issue has never been clarified. For further examination, a series of simulations with jet densities lower than those in our parameter study is required. We would also like to deepen our understanding of how the magnetic field affects the stability of the beam. Particularly interesting in that respect would be to find out exactly which combination of jet parameters leads to the suppression of turbulence in the cavity. Starting point for such an examination should be model series B1, where a weak toroidal field has a larger effect on the cavity than a strong one. The low magnetisation of beams and hot spots is another interesting result of our simulations. Since observers usually infer larger magnetic field strengths in those regions, further simulations with larger initial fields are required to clarify this issue. The combination of poloidal and toroidal fields could also have the desired effect. However, the study of many features related with the combination of poloidal and toroidal magnetic fields require three dimensional simulations (in order to allow for helical field structures or field reversals).

Considering long term simulations of large scale jets, several further steps are quite obvious (apart from continuing our existing model up to the full life time of a powerful radio jet). First of all, we would like to include poloidal fields in the simulations, ideally in combination with a larger toroidal field component. This could help to increase the magnetisation of the plasma inside the beam and in the hot spots.

Moreover, this would allow us to compute realistic polarisation maps from our simulation data. In a second step we would include a model for the galactic atmosphere in the initial setup of the external medium. A density and pressure declining with distance from the nucleus could lead to a much larger sideways expansion of the jet's cavity, and thus to smaller aspect ratios, which are closer to those observed. Additionally, intra cluster magnetic fields on the micro Gauss level should be included in the model. As a third step we suggest to perform the computation of the emission of the jets during the simulation itself. This would allow us to use more advanced models for the emitting electrons. However, such a procedure requires a considerably larger amount of computing resources, which will only become available in a few years time. Finally, as mentioned above, three dimensional simulations are required to capture all the effects of the magnetic field.

List of Figures

1.1 Montage of different images of the radio galaxy M87 10
1.2 Fanaroff–Riley class II radio galaxy superposed onto an optical image 12
1.3 Illustration of superluminal motion. 15
1.4 Sketch of the morphology of a light jet. 18

2.1 Schematic explanation of a hydrodynamic Riemann problem. 32
2.2 The quartic equation (2.44) for a Lorentz factor of 20. 34
2.3 Analytic versus numerically computed eigenvalues. 35
2.4 Illustration of the staggered grid magnetic fields. 40
2.5 Flow diagram of the code. 41
2.6 First 1D test problem. 44
2.7 Second 1D test problem. 46
2.8 Third 1D test problem. 47
2.9 Fourth 1D test problem. 48
2.10 Fifth 1D test problem. 49
2.11 Cylindrical explosion test with PLM reconstruction. 51
2.12 Cylindrical explosion test with PPM reconstruction. 51
2.13 Cylindrical explosion test: comparison at different resolutions. 52
2.14 Jet model A from Komissarov (1999*b*) at time 110. 53
2.15 Convergence test results. 54

3.1 Diagram of a 2D cylindrical grid. 56
3.2 C2: snapshots of the logarithm of the rest mass density of different models. 61
3.3 C2: snapshots of the logarithm of the thermal pressure of different models. 62
3.4 C2: snapshots of the Lorentz factor of different models. 63

3.5 Snapshots of β and B^ϕ of the two strongly magnetised models of the C2 series. . . . 64

3.6 Snapshots of the poloidal field model C2-pol-1: rest mass density, thermal pressure and Lorentz factor. . . . 66

3.7 Snapshots of the poloidal field model C2-pol-1: magnetic field with field lines and β parameter. . . . 67

3.8 C2: time evolution of various quantities. . . . 68

3.9 B1: snapshots of the logarithm of the rest mass density of different models. . . . 71

3.10 B1: snapshots of the logarithm of the thermal pressure of different models. . . . 72

3.11 B1: snapshots of the Lorentz factor of different models 73

3.12 Snapshots of β and B^ϕ for the two strongly magnetised models of the B1 series. . . . 74

3.13 Snapshots of the poloidal field model B1-pol-1: rest mass density, thermal pressure and Lorentz factor. . . . 76

3.14 Snapshots of the poloidal field model B1-pol-1: magnetic field with field lines and β parameter. . . . 77

3.15 B1: time evolution of various quantities. . . . 78

3.16 C1: snapshots of the logarithm of the rest mass density of different models. . . . 81

3.17 C1: snapshots of the logarithm of the thermal pressure of different models. . . . 82

3.18 C1: snapshots of the Lorentz factor of different models. . . . 83

3.19 Snapshots of β and B^ϕ of the two strongly magnetised models of the C1 series. . . . 84

3.20 Snapshots of the poloidal field model C1-pol-1: magnetic field with field lines and β parameter. . . . 85

3.21 C1: time evolution of various quantities. . . . 86

4.1 Rest mass density snapshots of the long term simulation models. . . . 93

4.2 Beam averaged quantities plotted along the axis of model LA1 and LA0. . . . 94

4.3 Thermal pressure snapshots of the long term simulation models. . . . 95

4.4 Snapshots of the Lorentz factor and of div($W\mathbf{v}$) of the long term simulation models. . . . 97

4.5 Snapshots of the logarithm of B^ϕ (upper panel) and of β (lower panel) of model LA1. . . . 99

4.6 Long term models: time evolution plots of head position, aspect ratio and cavity pressure. 101

4.7 Long term models: time evolution plots of hot spot pressure, cavity β and cocoon β. 102

4.8 Simulated radio maps for model LA1 using one electron population. . 107

4.9 Simulated radio maps for model LA1 using two electron populations. 108

4.10 Image of Cyg A 108

Bibliography

Aloy M., Martí J., Gómez J., Agudo I., Müller E., Ibáñez J. (2003). "Three-dimensional Simulations of Relativistic Precessing Jets Probing the Structure of Superluminal Sources". *Astrophysical Journal*, **585**:L109–L112. 18

Aloy M.A., Gómez J.L., Ibáñez J.M., Martí J.M., Müller E. (2000). "Radio emission from three-dimensional relativistic hydrodynamic jets: observational evidence of jet stratification". *Astrophysical Journal*, **528**:L85–L88. 14, 18, 107, 109

Aloy M.A., Ibáñez J.M., Miralles J.A., Urpin V. (2002). "Stability analysis of relativistic jets from collapsars and its implications on the short-term variability of gamma-ray bursts". *Astronomy and Astrophysics*, **396**:693–703. 18

Aloy M.A., Ibáñez J.M., Martí J.M., Gómez J.L., Müller E. (1999*a*). "High-resolution three-dimensional simulations of relativistic jets". *Astrophysical Journal*, **523**:L125–L128. 18

Aloy M.A., Ibáñez J.M., Martí J.M., Müller E. (1999*b*). "Genesis: A High-Resolution Code for Three-Dimensional Relativistic Hydrodynamics". *Astrophysical Journal Supplement Series*, **122**:151–166. 18, 41

Aloy M.A., Martí J.M. (2002). "3D Relativistic Hydrodynamics". In *LNP Vol. 589: Relativistic Flows in Astrophysics*, pages 197–+. 18

Aloy M.A., Müller E., Ibáñez J.M., Martí J.M., MacFadyen A. (2000). "Relativistic Jets from Collapsars". *Astrophysical Journal Letters*, **531**:L119–L122. 18

Aloy M.A., Pons J..A., Ibáñez J.M. (1999*c*). "An efficient implementation of flux formulae in multidimensional relativistic hydrodynamical codes". *Computer Physics Communications*, **120**:115–121. 35

Anile A.M. (1989). *Relativistic fluids and magneto–fluids* (Cambridge University Press). 21, 24, 27, 28

Appl S., Camenzind M. (1988). "Shock conditions for relativistic MHD jets". *Astronomy and Astrophysics*, **206**:258–268. 23

Appl S., Camenzind M. (1992). "The stability of current-carrying jets". *Astronomy and Astrophysics*, **256**:354–370. 17

Baade W. (1956). "Polarization in the Jet of Messier 87". *Astrophysical Journal*, **123**:550–551. 7

Baade W., Minkowski R. (1954). "On the Identification of Radio Sources". *Astrophysical Journal*, **119**:215–231. 7

Balsara D.S. (2001). "Total Variation Diminishing Scheme For Relativistic Magnetohydrodynamics". *Astrophysical Journal Supplement Series*, **132**:83–101. 28, 42, 43, 45

Balsara D.S., Norman M.L. (1992). "Three-dimensional hydrodynamic simulations of narrow-angle-tail radio sources. I - The Begelmann, Rees, and Blandford model". *Astrophysical Journal*, **393**:631–647. 17

Balsara D.S., Spicer D.S. (1999). "A Staggered Mesh Algorithm Using High Order Godunov Fluxes to Ensure Solenoidal Magnetic Fields in Magnetohydrodynamic Simulations". *Journal of Computational Physics*, **149**:270–292. 39

Begelman M.C., Cioffi D.F. (1989). "Overpressured cocoons in extragalactic radio sources". *Astrophysical Journal Letters*, **345**:L21–L24. 103

Begelman M.C., Rees M.J., Blandford R.D. (1979). "A twin-jet model for radio trails". *Nature*, **279**:770–773. 12

Begelman M.C., Rees M.J., Sikora M. (1994). "Energetic and radiative constraints on highly relativistic jets". *Astrophysical Journal Letters*, **429**:L57–L60. 14

Begelmann M.C., Blandford R.D., Rees M.J. (1984). "Theory of extragalactic radio sources". *Reviews of Modern Physics*, **56**(No. 2, Part I):255–351. 13, 14, 21

Benson J.M., Walker R.C., Unwin S.C., Muxlow T.W.B., Wilkinson P.N., Booth R.S., Pilbratt G., Simon R.S. (1988). "VLBI and MERLIN observations of 3C 120 at 1.7 GHz - Superluminal motions beyond 0.05 arcsec". *Astrophysical Journal*, **334**:560–572. 12

Bicknell G.V. (1996). "Decelerating relativistic jets and the Fanaroff-Riley classification". In Hardee et al. (1996), pages 253+. 14

Blandford R. (2002). "Blood Out Of Stone". *Science*, **295**:1653+. 16, 19

Blandford R., Payne D. (1982). "Hydromagnetic flows from accretion discs and the production of radio jets". *Monthly Notices the Royal Astronomical Society*, **199**:883–903. 16

Blandford R.D., Königl A. (1979). "Relativistic jets as compact radio sources". *APJ*, **232**:34–48. 15

Blandford R.D., Rees M.J. (1974). "A 'Twin–Exhaust' Model for Double Radio Sources". *Monthly Notices the Royal Astronomical Society*, **169**:395–415. 7, 14, 16

Blandford R.D., Znajek R.L. (1977). "Electromagnetic extraction of energy from Kerr black holes". *Monthly Notices the Royal Astronomical Society*, **179**:433–456. 16

Bodo G., Rossi P., Massaglia S., Ferrari A., Malagoli A., Rosner R. (1998). "Three-dimensional simulations of jets". *Astronomy and Astrophysics*, **333**:1117–1129. 17

Brackbill J.U., Barnes D.C. (1980). "Note: The effect of nonzero $\nabla \cdot \mathbf{B}$ on the numerical solution of the magnetohydrodynamic equations". *Journal of Computational Physics*, **35**:426. 39

Bridle A.H. (1984). "Sidedness, field configuration, and collimation of extragalactic radio jets". *Astronomical Journal*, **89**:979–986. 13

Bridle A.H. (2003). Personal web page at the *National Radio Astronomy Observatory*, `http://www.cv.nrao.edu/~abridle/`. 12

Bridle A.H., Hough D.H., Lonsdale C.J., Burns J.O., Laing R.A. (1994). "Deep VLA imaging of twelve extended 3CR quasars". *Astronomical Journal*, **108**:766–820. 9

Bridle A.H., Perley R.A. (1984). "Extragalactic Radio Jets". *Annu. Rev. Astron. Astrophys.*, **22**:319–358. 13

Brio M., Wu C.C. (1988). *Journal of Computational Physics*, **75**:400. 42, 44

Burns J.O., Norman M.L., Clarke D.A. (1991). "Numerical models of extragalactic radio sources". *Science*, **253**:522–530. 17

Carilli C., Perley R., Bartel N., Dreher J. (1996). "The jets in Cygnus A: from pc- to kpc-scales". In Carilli & Harris (1996), pages 76–+. 105

Carilli C.L., Harris D.E. (eds.) (1996). *Cygnus A – Study of a Radio Galaxy*. 123

Clarke D.A., Burns J.O., Norman M.L. (1989). "Numerical observations of a simulated jet with a passive helical magnetic field". *Astrophysical Journal*, **342**:700–717. 17

Clarke D.A., Norman M.L., Burns J.O. (1986). "Numerical simulations of a magnetically confined jet". *Astrophysical Journal Letters*, **311**:L63–L67. 17, 59, 87

Cohen M.H., Cannon W., Purcell G.H., Shaffer D.B., Broderick J.J., Kellermann K.I., Jauncey D.L. (1971). "The Small-Scale Structure of Radio Galaxies and Quasi-Stellar Sources at 3.8 Centimeters". *Astrophysical Journal*, **170**:207–+. 13

Colella P., Woodward P.R. (1984). "The piecewise–parabolic method (PPM) for gasdynamic simulations". *Journal of Computational Physics*, **54**:174. 36

Cox C.I., Gull S.F., Scheuer P.A.G. (1991). "Three-dimensional simulations of the jets of extragalactic radio sources". *Monthly Notices the Royal Astronomical Society*, **252**:558–585. 107

Curtis H.D. (1918). *Publications of the Lick Observatory*, **13**:9. 7

Dai W., Woodward P.R. (1998). "On the divergence-free condition and conservation laws in numerical simulations for supersonic magnetohydrodynamic flows". *Astrophysical Journal*, **494**:317. 39

Daly R.A. (1995). "Powerful Extended Radio Sources as Tools to Estimate Ambient Gas Densities, Jet Luminosities, and Other Key Physical Parameters". *Astrophysical Journal*, **454**:580–+. 106

Dedner A., Kemm F., Kröner D., Munz C.D., Schitzer T., Wesenberg M. (2002). "Hyperbolic Divergence Cleaning for the MHD Equations". *Journal of Computational Physics*, **175**:645–673. 39

Del Zanna L., Bucciantini N., Londrillo P. (2003). "An efficient shock-capturing central-type scheme for multidimensional relativistic flows. II. Magnetohydrodynamics". *Astronomy and Astrophysics*, **400**:397–413. 34, 42, 43, 45, 50, 54

Donahue M., Daly R.A., Horner D.J. (2003). "Constraints on the Cluster Environments and Hot Spot Magnetic Field Strengths of the Radio Sources 3C 280 and 3C 254". *Astrophysical Journal*, **584**:643–656. 13, 105

Donat R., Marquina A. (1996). "Capturing shock reflections: an improved flux formula". *Journal of Computational Physics*, **125**:42. 35, 45

Dubal M. (1991). *Computer Physics Communications*, **64**:221. 50

Duncan C.G., Hughes P.A. (1994). "Simulations of relativistic extragalactic jets". *Astrophysical Journal*, **436**:L119. 17

Einfeldt B. (1988). "On Godunov-Type Methods for Gas Dynamics". *SIAM Journal on Numerical Analysis*, **25**:294–318. 33

Evans C.R., Hawley J.F. (1988). "Simulation of magnetohydrodynamic flows: A constrained transport method". *Astrophysical Journal*, **332**:659. 39

Fanaroff B.L., Riley J.M. (1974). "The Morphology of Extragalactic Radio Sources of High and Low Luminosity". *Monthly Notices the Royal Astronomical Society*, **167**:31P–35P. 11

Ferrari A. (1998). "Modeling Extragalactic Jets". *Annu. Rev. Astron. Astrophys.*, **36**:539–598. 13, 14, 105

Gambill J.K., Sambruna R.M., Chartas G., Cheung C.C., Maraschi L., Tavecchio F., Urry C.M., Pesce J.E. (2003). "Chandra observations of nuclear X-ray emission from a sample of radio sources". *Astronomy and Astrophysics*, **401**:505–517. 8

Ghisellini G., Padovani P., Celotti A., Maraschi L. (1993). "Relativistic bulk motion in active galactic nuclei". *Astrophysical Journal*, **407**:65–82. 14

Ghisellini G., Padovani P., Celotti A., Maraschi L. (1993). "Relativistic bulk motion in active galactic nuclei". *Astrophysical Journal*, **407**:65–82. 15

Gómez J., Marscher A.P., Alberdi A. (1999). "86, 43, and 22 GHZ VLBI Observations of 3C 120". *Astrophysical Journal Letters*, **521**:L29–L32. 12

Gómez J., Marsher A., Alberdi A., Martí J.M., Ibáñez J. (1998). "Subparsec Polarimetric Radio Observations of 3C 120: A Close-up Look at Superluminal Motion". *Astrophysical Journal*, **499**:221. 12

Hardcastle M.J., Birkinshaw M., Cameron R.A., Harris D.E., Looney L.W., Worrall D.M. (2002). "Magnetic Field Strengths in the Hot Spots and Lobes of Three Powerful Fanaroff-Riley Type II Radio Sources". *Astrophysical Journal*, **581**:948–973. 13, 105

Hardcastle M.J., Birkinshaw M., Worrall D.M. (1998). "Magnetic field strengths in the hotspots of 3C 33 and 111". *Monthly Notices the Royal Astronomical Society*, **294**:615–+. 13, 105

Hardee P.E., Bridle A.H., Zensus J.A. (eds.) (1996). *Energy Transport in Radio Galaxies and Quasars*, volume 100 of *ASP Conference Series*. 122, 127, 129

Hardee P.E., Clarke D.A., Howell D.A. (1995). "The Stability and Collimation of Three-Dimensional Jets". *Astrophysical Journal*, **441**:644–664. 17

Hardee P.E., Cooper M.A., Norman M.L., Stone J.M. (1992). "Spatial stability of the magnetized slab jet". *Astrophysical Journal*, **399**:478–494. 17

Hardee P.E., Norman M.L. (1988). "Spatial stability of the slab jet. I. Linear instability analysis". *Astrophysical Journal*, **334**:70–79. 17

Harris D.E., Carilli C.L., Perley R.A. (1994). "X-Ray Emission from the Radio Hotspots of Cygnus-A". *Nature*, **367**:713–+. 13

Harten A., Lax P.D., van Leer B. (1983). "On Upstream Differencing and Godunov-Type Schemes for Hyperbolic Conservation Laws". *SIAM Review*, **25**:35–61. 33

Heinz S., Begelman M.C. (1997). "Analysis of the Synchrotron Emission from the M87 Jet". *Astrophysical Journal*, **490**:653–+. 13

Hooda J.S., Mangalam A.V., Wiita P.J. (1994). "Long-term hydrodynamical simulations of extragalactic radio jets". *Astrophysical Journal*, **423**:116–130. 109

Hough D.H., Vermeulen R.C., Readhead A.C.S., Cross L.L., Barth E.L., Yu L.H., Beyer P.J., Phifer E.M. (2002). "Parsec-Scale Radio Structure and Broad Optical Emission Lines in a Complete Sample of 3CR Lobe-dominated Quasars". *Astronomical Journal*, **123**:1258–1287. 15

Hughes P.A. (ed.) (1991). *Beams and Jets in Astrophysics*. Cambridge Astrophysics Series (Cambridge University Press). 125, 127, 129

Hughes P.A., Miller L. (1991). "Introduction: Synchrotron and Inverse-Compton Radiation". In Hughes (1991), chapter 1. 8

Jackson J. (1975). *Classical Electrodynamics*. 2nd edition (John Wiley & Sons Inc., New York). 21, 24

Jennison R.C., Das Gupta M.K. (1953). *Nature*, **172**:996. 7

Koide S. (1997). "A Two-dimensional Simulation of a Relativistic Jet Bent by an Oblique Magnetic Field". *Astrophysical Journal*, **478**:66–+. 18, 109

Koide S. (2003). "Magnetic extraction of black hole rotational energy: Method and results of general relativistic magnetohydrodynamic simulations in Kerr spacetime". *Phys. Rev. D.*, **67**:104010–+. 19

Koide S., Meier D.L., Shibata K., Kudoh T. (2000). "General Relativistic Simulations of Early Jet Formation in a Rapidly Rotating Black Hole Magnetosphere". *Astrophysical Journal*, **536**:668–674. 19

Koide S., Nishikawa K., Mutel R.L. (1996). "A Two-dimensional Simulation of Relativistic Magnetized Jet". *Astrophysical Journal Letters*, **463**:L71+. 18

Koide S., Shibata K., Kudoh T. (1998). "General Relativistic Magnetohydrodynamic Simulations of Jets from Black Hole Accretions Disks: Two-Component Jets Driven by Nonsteady Accretion of Magnetized Disks". *Astrophysical Journal*, **495**:L63. 19

Koide S., Shibata K., Kudoh T. (1999). "Relativistic Jet Formation from Black Hole Magnetized Accretion Disks: Method, Tests, and Applications of a General Relativistic Magnetohydrodynamic Numerical Code". *Astrophysical Journal*, **522**:727–752. 19

Koide S., Shibata K., Kudoh T., Meier D.L. (2002). "Extraction of Black Hole Rotational Energy by a Magnetic Field and the Formation of Relativistic Jets". *Science*, **295**:1688–1691. 19

Komissarov S.S. (1999*a*). "A Godunov-type scheme for relativistic magnetohydrodynamics". *Monthly Notices the Royal Astronomical Society*, **303**:343–366. 19, 28, 42, 50

Komissarov S.S. (1999*b*). "Numerical simulations of relativistic magnetized jets". *Monthly Notices the Royal Astronomical Society*, **308**:1069–1076. 19, 23, 50, 53, 87, 88, 117

Komissarov S.S., Falle S.A.E.G. (1997). "Simulations of Superluminal Radio Sources". *Monthly Notices the Royal Astronomical Society*, **288**:833–848. 18

Komissarov S.S., Falle S.A.E.G. (1998). "The large-scale structure of FR-II radio sources". *Monthly Notices the Royal Astronomical Society*, **297**:1087–1108. 18, 103, 106

Komissarov S.S., Falle S.A.E.G. (2003). "The evolution of slab jets and self-similar models of extragalactic radio sources". *Monthly Notices the Royal Astronomical Society*, **343**:1045–1053. 107

Komissarov S.S., Lyubarsky Y.E. (2003). "The origin of peculiar jet-torus structure in the Crab nebula". *Monthly Notices the Royal Astronomical Society*, **344**:L93–L96. 19

Königl A. (1980). "Relativistic gasdynamics in two dimensions". *Physics of Fluids*, **23**:1083–1090. 56

Kössl D., Müller E., Hillebrandt W. (1990). "Numerical simulations of axially symmetric magnetized jets. I - The influence of equipartition magnetic fields. II - Apparent field structure and theoretical radio maps. III - Collimation of underexpanded jets by magnetic fields". *Astronomy and Astrophysics*, **229**:378–415. 17, 87

Krasnopolsky R., Li Z.Y., Blandford R. (2003). "Magnetocentrifugal Launching of Jets from Accretion Disks. II. Inner Disk-Driven Winds". *Astrophysical Journal*, **595**:631–642. 16

Krolik J.H. (1999). *Active galactic nuclei : from the central black hole to the galactic environment* (Active galactic nuclei : from the central black hole to the galactic environment /Julian H. Krolik. Princeton, N. J. : Princeton University Press, c1999.). 9, 11

Laing R. (1993). In D. Burgarella, M. Livio, C. O'Dea (eds.), *Astrophysical Jets*, page 95 (Cambridge University Press, Cambridge). 13

Laing R.A. (1996*a*). "Brightness and polarization structure of decelerating relativistic jets". In Hardee et al. (1996), page 241. 14

Laing R.A. (1996*b*). "Large Scale Structure: Jets on kiloparsec Scales (Review)". In *IAU Symposia*, volume 175, page 147. 14

Laing R.A., Bridle A.H. (2002). "Relativistic models and the jet velocity field in the radio galaxy 3C 31". *Monthly Notices the Royal Astronomical Society*, **336**:328–352. 13

Laing R.A., Canvin J.R., Bridle A.H. (2003). "The physics of jets in FR I radio galaxies". *New Astronomy Review*, **47**:577–579. 13

Landau L.D., Lifschitz E.M. (1966). *Hydrodynamik*, volume VI of *Lehrbuch der Theoretischen Physik* (Akademie Verlag, Berlin). 24, 31

Leahy J.P. (1991). "Interpretation of Large Scale Extragalactic Jets". In Hughes (1991), chapter 3. 9

LeVeque R.J. (1991). *Numerical Methods for Conservation Laws* (Birhkhäuser, Basel). 29, 30, 36

LeVeque R.J. (1998). "Nonlinear Conservation Laws and Finite Volume Methods for Astrophysical Fluid Flow". In O. Steiner, A. Gautschy (eds.), *Computational Methods for Astrophysical Fluid Flow*, 27th Saas-Fee Advanced Course / Lecture Notes 1997 (Springer-Verlag, Berlin). 30, 33

Lind K.R., Payne D.G., Meier D.L., Blandford R.D. (1989). "Numerical simulations of magnetized jets". *Astrophysical Journal*, **344**:89–103. 17, 59, 87

Loken C., Roettiger K., Burns J.O., Norman M. (1995). "Radio jet propagation and wide-angle tailed radio sources in merging galaxy cluster environments". *Astrophysical Journal*, **445**:80–97. 17, 109

Marscher A.P., Gear W.K. (1985). "Models for high-frequency radio outbursts in extragalactic sources, with application to the early 1983 millimeter-to-infrared flare of 3C 273". *Astrophysical Journal*, **298**:114–127. 14

Martí J.M., Ibáñez J.M., Miralles J. (1991). *Phys. Rev. D*, **43**:3794. 17

Martí J.M., Müller E., Ibañez J.M. (1998). "The Long Term Evolution of Powerful Relativistic Jets". In *Astrophysical Jets: Open Problems*, pages 149–+. 18

Martí J.M., Müller E. (1994). "The analytical solution of the Riemann problem in relativistic hydrodynamics". *JFL*, **258**:317+. 31

Martí J.M., Müller E. (1996). "Extension of the Piecewise Parabolic Method to One–Dimensional Relativistic Hydrodynamics". *Journal of Computational Physics*, **123**:1–14. 17, 36, 37

Martí J.M., Müller E. (1999). "Numerical Hydrodynamics in Special Relativity". *Living Reviews in Relativity*, **2**(1999-3). URL `http://www.livingreviews.org`. 30, 32

Martí J.M., Müller E., Font J.A., Ibáñez J.M. (1995). "Morphology and dynamics of highly supersonic relativistic jets". *Astrophysical Journal*, **448**:L105–L109. 17

Martí J.M., Müller E., Font J.A., Ibáñez J.M., Marquina A. (1997). "Morphology and dynamics of relativistic jets". *Astrophysical Journal*, **479**:151–163. 17, 58, 103

Martí J.M., Müller E., Ibáñez J.M. (1994). "Hydrodynamical simulations of relativistic jets". *Astronomy and Astrophysics*, **281**:L9–L12. 17

Meier D., Kiode S., Uchida Y. (2001). "Magnetohydrodynamic Production of Relativistic Jets". *Science*, **291**:84–92. 16

Mimica P., Aloy M.A., Müller E., Brinkmann W. (2004). "Synthetic X-ray light curves of BL Lacs from relativistic hydrodynamic simulations". *Astronomy and Astrophysics*. In press. 106

Müller E. (1998). "Astrophysical fluid flow". In O. Steiner, A. Gautschy (eds.), *Computational Methods for Astrophysical Fluid Flow*, 27th Saas-Fee Advanced Course/ Lecture Notes 1997 (Springer-Verlag, Berlin). 17, 18

Munz C.D., Omnes P., Schneider R., Sonnendrücker E., Voß U. (2000). "Divergence Correction Techniques for Maxwell Solvers Based on a Hyperbolic Model". *Journal of Computational Physics*, **161**:484–511. 39

Muxlow T.W.B., Garrington S.T. (1991). "Observation of Large Scale Extragalactic Jets". In Hughes (1991), chapter 2. 9, 11

Nishikawa K., Koide S., Sakai J., Christodoulou D.M., Sol H., Mutel R.L. (1997). "Three-Dimensional Magnetohydrodynamic Simulations of Relativistic Jets Injected along a Magnetic Field". *Astrophysical Journal Letters*, **483**:L45+. 18

Nishikawa K., Koide S., Sakai J., Christodoulou D.M., Sol H., Mutel R.L. (1998). "Three-dimensional Magnetohydrodynamic Simulations of Relativistic Jets Injected into an Oblique Magnetic Field". *Astrophysical Journal*, **498**:166–+. 18

Norman M.L. (1996). "Progress in numerical simulations of extragalactic radio sources". In Hardee et al. (1996), pages 405+. 18

Norman M.L., Burns J.O., Sulkanen M.E. (1988). "Disruption of galactic radio jets by shocks in the ambient medium". *Nature*, **335**:146–149. 17

Norman M.L., Hardee P.E. (1988). "Spatial stability of the slab jet. II. Numerical simulations". *Astrophysical Journal*, **334**:80–94. 17

Norman M.L., Winkler K.H.A., Smarr L., Smith M.D. (1982). "Structure and dynamics of supersonic jets". *Astronomy and Astrophysics*, **113**:285–302. 16

Okamoto I. (2003). "Global Asymptotic Solutions for Magnetohydrodynamic Jets and Winds". *Astrophysical Journal*, **589**:671–676. 16

Owen F.N., Rudnick L. (1976). "Radio Sources with Wide-Angle Tails in Abell Clusters of Galaxies". *Astrophysical Journal Letters*, **205**:L1–L4. 12

Powell K.G. (1994). "An Approximate Riemann Solver For Magnetohydrodynamics (That Works In More Than One Dimension)". ICASE Report 94-24, NASA Langley Research Center, Hampton, VA. 39

Press W.H., Teukolsky S.A., Vetterling W.T. (1992). *Numerical Recipes in* FORTRAN. 2nd edition (Cambridge University Press). 33, 38

Rees M. (1984). "Black Hole Models for Active Galactic Nuclei". *Annu. Rev. Astron. Astrophys.*, **22**:471–506. 16

Roe P. (1981). *Journal of Computational Physics*, **43**:357. 35

Rosen A., Hardee P.E., Clarke D.A., Johnson A. (1999). "Effects of Magnetic Fields on Mass Entrainment of Supermagnetosonic Jets". *Astrophysical Journal*, **510**:136–154. 17

Ryu D., Miniati F., Jones T.W., Frank A. (1998). "A divergence-free upwind code for multidimensional magnetohydrodynamic flows". *Astrophysical Journal*, **509**:244–255. 39

Sambruna R.M., Maraschi L., Tavecchio F., Urry C.M., Cheung C.C., Chartas G., Scarpa R., Gambill J.K. (2002). "A Survey of Extended Radio Jets in Active Galactic Nuclei with Chandra and the Hubble Space Telescope: First Results". *Astrophysical Journal*, **571**:206–217. 8, 9

Scheck L., Aloy M.A., Martí J.M., Gómez J.L., Müller E. (2002). "Does the plasma composition affect the long-term evolution of relativistic jets?" *Monthly Notices the Royal Astronomical Society*, **331**:615–634. 18, 57, 58, 91, 92, 103, 104, 106, 109, 112

Scheuer P.A.G. (1974). "Models of extragalactic radio sources with a continuous energy supply from a central object". *Monthly Notices the Royal Astronomical Society*, **166**:513–528. 7

Seielstad G.A., Cohen M.H., Linfield R.P., Moffet A.T., Romney J.D., Schilizzi R.T., Shaffer D.B. (1979). "Further monitoring of the structure of superluminal radio sources". *Astrophysical Journal*, **229**:53–72. 12

Shklovskii I.S. (1953). *Astronomicheskii Zhurnal*, **30**:15. 7

Shklovskii I.S. (1963). *Soviet Astronomy - AJ*, **6**:465. 7

Shone D.L., Porcas R.W., Zensus J.A. (1985). "Combined MERLIN/VLA observations of the superluminal quasar 3C179". *Nature*, **314**:603–+. 12

Shu C.W., Osher S.J. (1988). "Efficient Implementation of Essentially Non–oscillatory Shock–Capturing Schemes". *Journal of Computational Physics*, **77**:439–471. 37

Sol H., Pelletier G., Asseo E. (1989). "Two-flow model for extragalactic radio jets". *Monthly Notices the Royal Astronomical Society*, **237**:411–429. 14

Stawarz Ł., Ostrowski M. (2002). "Radiation from the Relativistic Jet: A Role of the Shear Boundary Layer". *Astrophysical Journal*, **578**:763–774. 14

Swain M.R., Bridle A.H., Baum S.A. (1998). "Internal structure of the jets in 3C 353". *Astrophysical Journal*, **507**:L29–L33. 14

Synge J. (1957). *The Relativistic Gas* (North-Holland Publ., Amsterdam). 103

Tominmatsu A., Takahashi M. (2003). "Relativistic Acceleration of Magnetically Driven Jets". *Astrophysical Journal*, **592**:321–331. 16

Toro E. (1997). *Riemann Solvers and Numerical Methods for Fluid Dynamics* (Springer-Verlag, Berlin, Heidelberg). 36

Tóth G. (2000). "The $\nabla \cdot \mathbf{B} = 0$ Constraint in Shock–Capturing Magnohydrodynamic Codes". *Journal of Computational Physics*, **161**:605–652. 38, 39

Urry C.M., Padovani P. (1995). "Unified Schemes for Radio-Loud Active Galactic Nuclei". *Publications of the Astronomical Society of the Pacific*, **107**:803–845. 14

van Putten M.H.P.M. (1993). "A two-dimensional relativistic (Gamma = 3.25) jet simulation". *Astrophysical Journal Letters*, **408**:L21–L23. 18, 43

van Putten M.H.P.M. (1995). *SIAM Journal on Numerical Analysis*, **32**:1504. 50

van Putten M.H.P.M. (1996). "Knots in Simulations of Magnetized Relativistic Jets". *Astrophysical Journal Letters*, **467**:L57+. 18

Vlahakis N., Tsinganos K. (1999). "A class of exect MHD models for astrophysical jets". *Monthly Notices the Royal Astronomical Society*, **307**:279–292. 16

Walker R.C. (1997). "Kiloparsec-Scale Motions in 3C 120—Revisited". *Astrophysical Journal*, **488**:675–+. 12

Walker R.C., Benson J.M., Unwin S.C. (1987). "The radio morphology of 3C 120 on scales from 0.5 parsecs to 400 kiloparsecs". *Astrophysical Journal*, **316**:546–572. 12

Wardle J. (1998). "Magnetic Fields in AGN". In Zensus et al. (1998). 13, 14

Whitney A.R., Shapiro I.I., Rogers A.E.E., Robertson D.S., Knight C.A., Clark T.A., Goldstein R.M., Marandino G.E., Vandenberg N.R. (1971). "Quasars Revisited: Rapid Time Variations Observed Via Very-Long-Baseline Interferometry". *Science*, **173**(3993):225–230. 13

Wilms J., Reynolds C.S., Begelman M.C., Reeves J., Molendi S., Staubert R., Kendziorra E. (2001). "XMM-EPIC observation of MCG-6-30-15: direct evidence for the extraction of energy from a spinning black hole?" *Monthly Notices the Royal Astronomical Society*, **328**:L27–L31. 16

Wilson A.S., Young A.J., Shopbell P.L. (2000). "Chandra Observations of Cygnus A: Magnetic Field Strengths in the Hot Spots of a Radio Galaxy". *Astrophysical Journal Letters*, **544**:L27–L30. 13

Worrall D.M., Birkinshaw M., Hardcastle M.J. (2001). "Chandra finds that X-ray jets are common in low-power radio galaxies". *Monthly Notices the Royal Astronomical Society*, **326**:L7–L12. 8

Zensus J., Taylor G., Wrobel J. (eds.) (1998). *IAU Colloquium 164: Radio Emission from Galactic and Extragalactic Compact sources*, volume 144 of *ASP Conference Series*. 131

Danksagung

Einen großen Anteil am Erfolg dieser Arbeit hatte Miguel-Angel Aloy. Er verbrachte während der vergangenen drei Jahre einen großen Teil seiner Arbeitszeit damit, zusammen mit mir über den RMHD Gleichungen zu brüten, das Programm zu optimieren und Probleme zu diskutieren (manchmal stundenlang). Seine Kreativität, sein Enthusiasmus und sein Einsatz für das Projekt waren eine große Hilfe und sehr motivierend. Dafür danke ich ihm von ganzem Herzen. Außerdem danke ich ihm für die beispielhafte Gastfreundschaft, die er mir bei meinen Besuchen in Valencia entgegen brachte.
Meinem Betreuer, Ewald Müller, danke ich für viele anregende und motivierende Diskussionen und die angenehme Arbeitsatmosphäre, die er in unser relativistischen Hydro Gruppe geschaffen hat. Zudem danke ich Ewald für das kritische Durchsehen des Manuskripts dieser Arbeit.
Luis Antón von der Universität Valencia hatte großen Anteil an der Entwicklung der numerischen Methoden, die in dieser Arbeit beschrieben werden. Seinem Betreuer, Chema Martí, und José Maria Ibañez und den restlichen Mitgliedern der Gruppe in Valencia danke ich für die außerordentlich freundliche Aufnahme in ihre Gruppe und ihre Gastfreundschaft während meiner zwei Besuche dort.
Ich danke Petar Mimica, der das Programm entwickelt hat, um die Radiokarten von meinen Simulationen zu berechnen.
Leonhard Scheck teilte mit mir das Büro am MPA seit dem Beginn unsere Diplomarbeit vor 4,5 Jahren. Seine Freundschaft hat maßgeblich dazu beigetragen, dass ich die Frustphasen dieser Arbeit unbeschadet überstand. Ich danke ihm auch für die Unterstützung bei kniffligen Programmierproblemen und bei der Entwicklung der IDL Programme, die ich für die Datenanalyse und die Bilder in dieser Arbeit benutzt habe. Desweiteren danke ich ihm dafür, dass ich über Jahre hinweg sein Kopilot und Navigator sein durfte. Möge sein Corolla in Frieden ruhen.
Die angenehme Arbeitsatmosphäre am MPA ist auch der Verdienst der folgenden Personen, denen ich herzlichst dafür danke: Daniel Sauer, Martin Jubelgas, Christian Haydn, Felix Stoehr, Fritz Röpke, Harry Dimmelmeier, und der Fußballmannschaft des MPA.

Schließlich möchte ich folgenden Menschen für Freundschaft und Unterstützung danken: den Mitgliedern meiner Band, Sina, Marc, Till und Roland, außerdem Norman, Jörg, David, meinen Eltern und Sonja.